

Daniel Kjønsvik Bang  
Erlend Ekern

# Aerodynamic Stability of a Suspension Bridge with an Aluminum Girder

Wind Tunnel Testing and Numerical Predictions

Master's thesis in ICT, Civil and Environmental Engineering

Supervisor: Ole Øiseth

June 2020



Daniel Kjønsvik Bang  
Erlend Ekern

# **Aerodynamic Stability of a Suspension Bridge with an Aluminum Girder**

Wind Tunnel Testing and Numerical Predictions

Master's thesis in ICT, Civil and Environmental Engineering  
Supervisor: Ole Øiseth  
June 2020

Norwegian University of Science and Technology  
Faculty of Engineering  
Department of Structural Engineering







# Sammendrag

Verdens første hengebru med brukasse i aluminum vurderes konstruert for fjordkryssingen av Langenuen. Ved å bruke aluminum istedenfor stål, oppstår det utfordringer blant annet med tanke på aerodynamisk stabilitet. Denne oppgaven tar for seg å finne en brukasseform som gir bruene tilfredstillende stabilitet.

For å undersøke mulige tverrsnittformer til en brukasse, ble en parametrisk modell etablert. Ved å ta utgangspunkt i et brukasse-konsept utarbeidet av Dr. techn. Olav Olsen, ble torsjonsstivheten i den parametriske modellen fastholdt til å være konstant. Videre ble seks ulike tverrsnittformer valgt ut. Disse har en varierende tverrsnittshøyde fra 5.5 m til 7.0 m, samt varierende vinkel på undersiden av kassen. For hver av de seks brukassene ble stivheter og massetreggheter estimert, og implementert i en parametrisert global elementmodell av hengebruene. Deretter ble modalanalyse brukt for å hente modale parametere. For å bestemme de aerodynamiske deriverte for hver av brukassene ble det utført vind-tunneltester på samtlige. Disse ble videre anvendt i estimeringen av kritisk vindhastighet for hver av brukassene.

De seks utvalgte brukassene er generelt høyere og mindre strømlinjeformet enn mange av stål-brukassene brukt i verdens lengste hengebruer. Dette er allikevel nødvendig for en brukasse i aluminium for å oppnå tilstrekkelig stivhet. Ved å fastholde konstant torsjonsstivhet forandres verken omkrets eller tverrsnittareal betydelig. Derfor vil materialbruken for de seks brukassene være lik, noe som er avgjørende for kostnaden av brukassene. Videre viser beregningene at stivheter og massetreggheter forblir reeltvis like for de seks brukassene. Dette resulterer i rimelig like modale egenskaper, og på grunn av dette er det de aerodynamiske egenskapene til brukassene som blir avgjørende for de estimerte kritiske vindhastighetene.

Resultatene viser at de fire brukassene med høyder 5.5, 5.8, 6.1 og 6.4 m alle oppfyller designkriteriet på 76 m/s, med estimerte kritiske vindhastigheter på henholdsvis 84.0, 86.8, 87.0 og 85.9 m/s. Brukassene med høyder 6.7 m og 7.0 m har kritiske vindhastigheter på 48.6, og 40.6 m/s, og oppfyller dermed ikke designkriteriet. For de fire laveste brukassene ble det avgjørende instabilitetsfenomenet "flutter", mens "galloping" ble avgjørende for de to høyeste brukassene. Det er videre noe høyere usikkerhet i estimatene for de tre høyeste brukassene, da de fikk påvist Reynoldstall-avhengighet i vindtunneltestingen. Betydelige virvelavløsningsinduserte vibrasjoner ble observert i testene av de to laveste brukassene. Dermed er muligens brukassen med høyde 6.1 m den mest optimale brukassen. Ettersom resultatene viser at de estimerte kritiske vindhastighetene for fire av brukassene er godt innenfor designkriteriet, burde det være mulig å realisere en brukasse med enda mindre materiale.

# Abstract

The world's first suspension bridge with an aluminium girder is being considered for the fjord crossing of Langenuen. The use of aluminium instead of steel gives rise to some challenges regarding the aerodynamic stability of the bridge. The goal of this thesis is to find a girder shape that has satisfactory aerodynamic stability.

To investigate the girder shape, a parametric model was established. By basing the model on a panel girder concept developed by Dr. techn. Olav Olsen in 2019, the torsional stiffness in the parametric model was constrained to be constant. Further, six unique girder shapes were selected. The cross-sectional properties of these girders were estimated and implemented in a global element model. Further, modal analysis was performed to attain the modal parameters. Forced vibration wind tunnel tests were conducted on section models of the six girders in order to obtain aerodynamic derivatives. These were implemented in the calculations of critical wind speed for each of the six girders.

The selected girder shapes are in general quite high and less streamlined than most of the steel girders in long-span suspension bridges today. However, it is acknowledged that an unconventional girder shape may be necessary when using aluminium in the girder instead of steel. An advantage of selecting girder shapes on the basis of constant torsional stiffness is that the resulting cross sectional area and perimeter of the girders also remain roughly unchanged. Therefore, the amount of material in the girders is also about the same, which is important for the cost of the girders. In addition, the cross-sectional property calculations show little variation in the stiffness and inertia forces of the girders. This results in the modal properties remaining relatively unchanged, and therefore the effect of the aerodynamic properties of the girders is in large part be isolated in the stability calculations.

The results show that the four girders of height 5.5, 5.8, 6.1 and 5.4 m all pass the design criteria of 76 m/s, with critical wind speed estimates of 84.0, 86.8, 87.0 and 85.9 m/s, respectively. The two girders of height 6.7 and 7.0 m did however not have sufficient stability, with 48.6 and 40.6 m/s. The instability phenomenon occurring for the four former girders is flutter, while galloping occurs for the two latter. Furthermore, there is slightly more uncertainty for estimates of the three highest girders, due to Reynolds number dependency observed in the processed data from the wind tunnel tests. Vortex shedding induced oscillations were also prevalent during the testing of the two lowest girders. Therefore, the 6.1 m girder may be the overall preferable option. Furthermore, since the results showed that the critical wind speeds of four girders are within the design criteria by a relatively large margin, a girder with less material may also be feasible.

# Preface

This report is the result of 20 weeks of work during the spring of 2020, and concludes our five year master's degree at Department of Structural Engineering, NTNU. Working on this thesis has been a very interesting and educational process for the both of us.

Due to the situation surrounding the COVID-19 pandemic, student access to campus and laboratories was denied from March 12th. Therefore, the wind tunnel testing was delayed and performed by the supervisor instead of the authors. Other than this, the work has been conducted from our home offices.

We would like to thank our supervisor Professor Ole Øiseth for his guidance throughout the semester, and Postdoc Øyvind Wiig Petersen for his help with the Abaqus modelling. It is motivating to collaborate with such devoted and interested supervisors.

The research group of Leirvik AS, Hydro, Dr. techn. Olav Olsen and the Norwegian Public Roads Administration has included us in their project, and shared their expertise. A special thanks goes to Dr. techn. Olav Olsen for consultation and interesting discussions. Their work was decisive for the direction taken in our thesis.

*Erlend Ekern and Daniel Kjønsvik Bang*  
Trondheim 10.06.2020

# Contents

<b>Sammendrag</b>	<b>i</b>
<b>Abstract</b>	<b>ii</b>
<b>Preface</b>	<b>iii</b>
<b>List of Figures</b>	<b>vii</b>
<b>List of Tables</b>	<b>viii</b>
<b>Abbreviations</b>	<b>ix</b>
<b>1 Introduction</b>	<b>1</b>
1.1 Problem Description: . . . . .	1
1.2 Structure of the Thesis . . . . .	2
<b>2 Theory</b>	<b>3</b>
2.1 Suspension Bridge Fundamentals . . . . .	3
2.2 Wind and Motion Induced Loads . . . . .	4
2.3 Modal Theory . . . . .	6
2.4 Aerodynamic Derivatives . . . . .	7
2.5 Motion Induced Instabilities . . . . .	9
2.6 Wind Tunnel Testing . . . . .	14
2.7 Identification of Static Coefficients . . . . .	15
2.8 Identification of Aerodynamic Derivatives . . . . .	16
2.9 Computation of Critical Wind Speed . . . . .	18
<b>3 Review of Current Long-Span Bridges</b>	<b>19</b>
3.1 A Brief History of Suspension Bridges . . . . .	19
3.2 Presentation of Box Girder Shapes . . . . .	25
<b>4 The Fjord Crossing of Langenuen</b>	<b>30</b>
4.1 Langenuen Suspension Bridge . . . . .	30
4.2 Aluminium Girder . . . . .	32
<b>5 Parametric Girder Shape</b>	<b>35</b>
5.1 Parametrization . . . . .	35
5.2 Torsional Stiffness Estimation . . . . .	36
5.3 Selecting Girder Shapes . . . . .	39

<b>6</b>	<b>Cross Sectional Parameters</b>	<b>42</b>
6.1	St. Venant Torsion . . . . .	42
6.2	Finite Element Analysis . . . . .	43
6.3	Thin-Wall Analysis . . . . .	45
6.4	Results . . . . .	50
<b>7</b>	<b>Global Element Model</b>	<b>55</b>
7.1	Global Design . . . . .	55
7.2	Modelling . . . . .	56
7.3	Girder Inertia . . . . .	57
7.4	Modal Properties . . . . .	60
<b>8</b>	<b>Wind Tunnel Tests</b>	<b>63</b>
8.1	Section Models . . . . .	63
8.2	Experimental Setup . . . . .	65
8.3	Test Description . . . . .	66
8.4	Test Observations . . . . .	67
<b>9</b>	<b>Experimental Results and Predicted Stability Limits</b>	<b>68</b>
9.1	Static Coefficients . . . . .	68
9.2	Aerodynamic Derivatives . . . . .	70
9.3	Predicted Stability Limits . . . . .	79
9.4	Discussion of Results . . . . .	90
<b>10</b>	<b>Conclusion</b>	<b>91</b>
10.1	Further work . . . . .	92
	<b>Appendices</b>	<b>96</b>
<b>A</b>	<b>List of Electronic Attachments</b>	<b>97</b>
<b>B</b>	<b>Girder Shape Drawings</b>	<b>98</b>
<b>C</b>	<b>Girder Inertia Properties</b>	<b>101</b>
<b>D</b>	<b>Modal Properties</b>	<b>102</b>
<b>E</b>	<b>Aerodynamic Derivatives</b>	<b>106</b>

# List of Figures

2.1	Main components of a suspension bridge. . . . .	3
2.2	Drag, lift and moment force components . . . . .	5
2.3	NTNU forced vibration rig. The section model is mounted between the two actuators. . . . .	14
3.1	Menai Suspension Bridge. Built in 1826. [31] . . . . .	20
3.2	Brooklyn Bridge. Built in 1883. [28] . . . . .	20
3.3	Williamsburg Bridge. Built in 1903. [42] . . . . .	21
3.4	The collapse of Tacoma Narrows Bridge. [12] . . . . .	22
3.5	The second Tacoma Narrows Bridge. [39] . . . . .	22
3.6	Akashi Kaikyo. The world's longest span. Built in 1998. [15] . . . . .	23
3.7	Great Belt Bridge. Built in 1998. [29] . . . . .	24
3.8	Hardanger Bridge. Built in 2013. [22] . . . . .	24
4.1	The Langenuen Suspension Brigde as presented by Norconsult in 2015 [6] .	30
4.2	Map of the Hordfast project with the Langenuen crossing marked in red [4]	31
4.3	The steel box girder as presented by Norconsult in 2015 [6] . . . . .	31
4.4	Dr.techn. Olav Olsen's proposed cross section in black line and a Julsundet cross section in red dashed line. The cross sections is scaled to equal width.	33
4.5	Panel girder cross section, as presented in Olav Olsen's report . . . . .	33
4.6	Close up of the panel geoemetry . . . . .	34
4.7	Panel girder section in 3D . . . . .	34
5.1	The 7 points defining the shape of the box girder cross section . . . . .	35
5.2	The remaining 2 points defining the shape . . . . .	35
5.3	Parametric girder . . . . .	36
5.4	Parametric girder Dynamo script . . . . .	36
5.5	Surface plot of the torsional stiffness constant $I_T$ as a function of H and $\theta$ , by Brechts 2. formula. Red stars indicate points at a value of $I_T = 31 \text{ m}^4$ . .	37
5.6	Constant torsional stiffness curve, $I_T = 31 \text{ m}^4$ . . . . .	38
5.7	Dynamo script implementing the function $\theta(H)$ . . . . .	38
5.8	Six selected girder shapes . . . . .	39
6.1	Part of the imported CAD-geometry . . . . .	44
6.2	FE Mesh of the 7.0 m girder . . . . .	44
6.3	Midlines of outer and inner panel plates. Outer midlines are marked in blue.	46
6.4	Node points. Outer points line 6 are marked in blue. . . . .	46
6.5	Python script . . . . .	47
6.6	Web segments . . . . .	47
6.7	The Dynamo script saves the .txt-file of the sketch . . . . .	48
6.8	Close up of the deck panel as seen in CrossX. . . . .	48
6.9	Close up of a node in a the exact CrossX model . . . . .	48
6.10	Simplified model of the girder of height 5.5 m . . . . .	49

6.11	Solid material cross sectional area . . . . .	50
6.12	Vertical and horizontal 2nd moment of area . . . . .	51
6.13	Torsional stiffness constant of three different calculation procedures . . . . .	52
6.14	Torsional stiffness constant of from estimation with Bredts 2. formula . . . . .	53
7.1	Abaqus Model of Langenuen Suspension Bridge . . . . .	55
7.2	Global dimensions of FE-models . . . . .	56
7.3	Connection elements between the hangers and the girder . . . . .	57
7.4	Boundary conditions of the FE-models . . . . .	57
7.5	Python code for adding beam girder inertia, for girder 5.5 m . . . . .	58
7.6	The torsional, horizontal and vertical mass of the six girders . . . . .	59
7.7	The rotational inertia $I_{22}$ of the bulkheads of the six girders . . . . .	59
7.8	First vertical mode shape . . . . .	60
7.9	Comparison of the natural frequencies between the six element models . . . . .	62
8.1	Milling of the 7.0 m model section at NTNU . . . . .	64
8.2	The fences mounted on the bridge deck . . . . .	64
8.3	CAD-model of the fences . . . . .	65
8.4	A section model mounted inside the wind tunnel . . . . .	65
8.5	The section model connected to the load cells and actuators . . . . .	66
9.1	Static coefficients . . . . .	69
9.2	The legend used for the AD-fits . . . . .	70
9.3	ADs for the 5.5 m girder . . . . .	71
9.4	ADs for the 5.8 m girder . . . . .	72
9.5	ADs for the 6.1 m girder . . . . .	73
9.6	ADs for the 6.4 m girder . . . . .	74
9.7	ADs for the 6.7 m girder . . . . .	75
9.8	ADs for the 7.0 m girder . . . . .	76
9.9	The legend used for the AD-plots . . . . .	77
9.10	Comparison of polynomial fit . . . . .	78
9.11	Critical wind speed estimates . . . . .	84
9.12	Argand diagrams of the instability modes for all six girders . . . . .	85
9.13	Comparison of the instability modes . . . . .	86
9.14	In-wind frequency and damping for the instability modes . . . . .	87
B.1	Girder shape of height 5.5 m . . . . .	99
B.2	Girder shape of height 5.8 m . . . . .	99
B.3	Girder shape of height 6.1 m . . . . .	99
B.4	Girder shape of height 6.4 m . . . . .	100
B.5	Girder shape of height 6.7 m . . . . .	100
B.6	Girder shape of height 7.0 m . . . . .	100
E.1	The legend used for the AD-plots . . . . .	106
E.2	ADs for 5.5 m . . . . .	107
E.3	ADs for 5.8 m . . . . .	108
E.4	ADs for 6.1 m . . . . .	109
E.5	ADs for 6.4 m . . . . .	110
E.6	ADs for 6.7 m . . . . .	111
E.7	ADs for 7.0 m . . . . .	112

# List of Tables

2.1	ADs effect on flutter . . . . .	8
3.1	The world's longest bridge spans, per June 2020 [44] . . . . .	25
4.1	Material properties of aluminum and steel . . . . .	32
5.1	Selected girder shapes . . . . .	41
6.1	Calculated parameters of selected girders . . . . .	54
7.1	Section properties . . . . .	56
7.2	Input for beam girder inertia . . . . .	58
7.3	Modal properties 5.5 m . . . . .	61
8.1	Considered test values in the forced vibration test . . . . .	67
9.1	Stability calculations 5.5 m . . . . .	80
9.2	Flutter combinations for 5.8 m . . . . .	80
9.3	Flutter combinations for 6.1 m . . . . .	81
9.4	Flutter combinations for 6.4 m . . . . .	81
9.5	Flutter combinations for 6.7 m . . . . .	82
9.6	Flutter combinations for 7.0 m . . . . .	82
9.7	Critical frequency and reduced velocity for the presented critical velocities .	83
9.8	Brief sensitivity analysis . . . . .	88
9.9	Critical wind speeds estimates for the six selected girders . . . . .	89
C.1	Girder inertia properties that vary between the six girders . . . . .	101
D.1	Modal properties 5.5 m . . . . .	103
D.2	Modal properties 5.8 m . . . . .	103
D.3	Modal properties 6.1 m . . . . .	104
D.4	Modal properties 6.4 m . . . . .	104
D.5	Modal properties 6.7 m . . . . .	105
D.6	Modal properties 7.0 m . . . . .	105



# Abbreviations

## Acronyms

DOF	Degree of Freedom
ADs	Aerodynamic Derivatives
NPRA	Norwegian Public Roads Administration
FE	Finite Element
FEM	Finite Element Method
NTNU	Norwegian University of Science and Technology
TNB	Tacoma Narrows Bridge

## Nomenclature

$\tilde{\mathbf{M}}_0, \tilde{\mathbf{C}}_0, \tilde{\mathbf{K}}_0$	Modal Mass, Modal Damping and Modal Stiffness Matrices
$\mathbf{K}_{ae}, \mathbf{C}_{ae}$	Aerodynamic stiffness and damping matrices
$\hat{\mathbf{K}}_{ae}, \hat{\mathbf{C}}_{ae}$	Normalized aerodynamic stiffness and damping matrices
$\tilde{\mathbf{Q}}, \tilde{\mathbf{Q}}_{ae}$	Modal Wind Load Matrices
$\mathbf{q}, \mathbf{q}_{Se}$	Load vectors
$q_y, q_z, q_\theta$	Drag, lift and moment load per unit length
$\Phi$	Matrix of mode vectors
$\varphi$	Mode Vector
$\phi_i$	Mode Vector Element
$\omega_i$	Eigenfrequency
$\zeta_i$	Damping ratio
$F_D, F_L, M$	Static Aerodynamic forces for Drag, Lift and Moment
$C_D, C_L, C_M$	Static coefficients for Drag, Lift and Moment
$P_i^*, H_i^*, A_i^*$	Aerodynamic derivatives related to drag, lift and moment
$K_i$	Reduced frequency
$\hat{\mathbf{H}}$	Response function
$\hat{\mathbf{E}}$	Impedance function
$\kappa, \zeta$	Matrix containing modal stiffness and damping contributions
$V_{cr}$	Critical wind speed

# Chapter 1

## Introduction

The Norwegian government has a long-term goal of developing a continuous coastal highway route between Kristiansand and Trondheim. This project involves several fjord crossings along the west coast of the country, one of which is the crossing of Langenuen. A suspension bridge concept has been developed for this crossing, and it has further been proposed to implement a bridge girder made out of aluminium instead of steel, in order to reduce the cost of the bridge. This would make Langenuen the first suspension bridge in the world with an aluminium girder. For this to be realized, extensive research must be conducted to develop new production methods and to rethink the application of known technology. This thesis addresses one of the problems to be solved: achieving sufficient aerodynamic stability.

There has been identified several advantages of using an aluminum girder. The western part of Norway has a prominent aluminum industry, which allows the girder to be produced locally. For an industry that has experienced a fall of demand [24][30], such a project would create job activities. As Norwegian aluminum works are powered by hydro power and the transportation distance to the building site would be low, it is a good reason to believe that the overall carbon footprint would be lower than for the steel alternative. Another environmental aspect is that recycling aluminum only demands 5% of the energy required to produce primary aluminum [21].

### 1.1 Problem Description:

As aluminium has both less weight and stiffness than steel, some challenges arise regarding the aerodynamic stability of the bridge. The lowest wind speed at which instability occurs is referred to as the critical wind speed,  $V_{cr}$ , or the aerodynamic stability limit. This limit is dependent upon two main factors: the modal properties of the bridge, and the aerodynamic properties of the girder. In order to be able to accurately estimate the critical wind speed, wind tunnel tests must first be performed on a section model of the girder shape.

By producing section models of several different girder shapes, and testing them in a wind tunnel at NTNU, this thesis provides results regarding the aerodynamic stability that directly supply the ongoing research project of the crossing of Langenuen. In addition, the thesis presents a design method for the girder shape which is shown to successfully isolate the effect of the aerodynamic properties in the aerodynamic stability calculations.

## 1.2 Structure of the Thesis

The thesis starts out by presenting the necessary basic theory for the problem handled in the thesis. Chapter 3 presents a study of the various girder shapes used in the world's longest suspension bridges today, and provides a brief history of the evolution of suspension bridges. This study is conducted to get a perspective of the existing solutions, which is further utilized when selecting girder shapes to be investigated in the thesis. The next chapter presents the work that has already conducted for the fjord crossing, which provides the groundwork for the thesis. In chapter 5, the method developed to select the girder shapes to be investigated in the thesis is presented. The calculation of cross sectional parameters for each of the selected girders is presented in chapter 6, and the results are compared between the girders. These parameters are further implemented in global element models in chapter 7, which are used to attain the modal properties. In chapter 8, the experimental setup for the forced vibration wind tunnel tests conducted at NTNU is presented. The resulting processed data is presented in chapter 9, along with the critical wind speed estimates. The results are discussed and compared between the girders. Finally, a conclusion to the research is given in chapter 10, as well as proposals for further work.

# Chapter 2

## Theory

### 2.1 Suspension Bridge Fundamentals

Among the various types of bridges in the world, it is the suspension bridge that covers the longest spans. This can be attributed to an effective and simple structural design. The structural system of the suspension bridge consists of a stiffening girder, the main cables, the hangers, the pylons and the anchor blocks. These components are shown in figure 2.1. The road is placed on top of the girder, which is connected to the main cables through vertical hangers. The main cables go over the pylons on each side of the span, and are further anchored into the ground in each end. The cables and hangers are loaded in tension, while the towers are in compression.

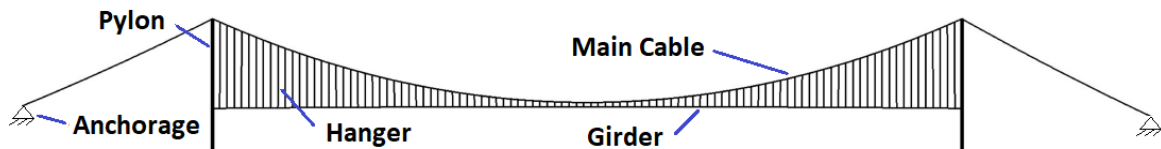


Figure 2.1: Main components of a suspension bridge.

Further, a suspension bridge has three suspended spans in total; the main span and two side spans. When the girder is not attached to the main cables at the side spans, as is the case in figure 2.1, the bridge is referred to as a single-span suspension bridge. These types of suspension bridges are often practical for fjord crossings, where the pylons are placed on land.

A suspension bridge is subjected to three main loads: self weight, traffic and wind. For long-span bridges, the self-weight of the girder becomes the dominating gravitational load [11]. The necessary dimensions in the cables and hangers are therefore in large part determined by the girder weight.

Long-span suspension bridges are also particularly vulnerable to dynamic excitation from wind loading. Harmless moderate oscillations are not uncommon. However, historical observations have shown that suspension bridges can oscillate to the point of becoming unstable, which may ultimately result in structural collapse. A physical explanation of this phenomenon is that the wind introduces more kinetic energy into the structural system than the system is able to dissipate [17]. The smallest wind speed of which instability may occur is called the critical wind speed, or the aerodynamic stability limit.

The aerodynamic stability is dependent upon the modal properties of the bridge, i.e. it's

mass, damping and stiffness, and the aerodynamic properties of the girder. Some mathematical models exist to describe the instability, but it still remains challenging to describe the aerodynamic behaviour of bridge girders analytically. Therefore, wind tunnel testing is a necessary tool to accurately evaluate the aerodynamic stability in suspension bridges.

As noted, the girder stiffness is an important factor for the aerodynamic performance of a suspension bridge. The torsional stiffness of the girder is of special importance. This is the torsional mode shapes play significant roles in the instability phenomena. The height of the girder is typically indicative of its stiffness. Therefore, the measurement known as "slenderness", which is the ratio between the height of the girder and the main span length of the bridge [19], can be interesting to consider. Another ratio that can be of interest is the height of the girder divided by the width of the girder. This number is indicative of the stiffness of the girder in relation to the aerodynamic drag force on the girder.

There are two main types of stiffening girders used in long-span suspension bridges, namely truss and closed box girders. The closed box girder is the more modern design, and it is generally preferable due to more efficient manufacturing, less demand for maintenance and overall less weight. However, the truss girder is still often preferred for carrying traffic in two storeys. The closed box girder has a closed thin-wall cross section, which provides superior torsional stiffness to an open thin-wall cross section. It has also a streamlined shape, in order to minimize aerodynamic forces on the girder. Still, there are many different cross-sectional shapes used for closed box girders in the world. In chapter 3, drawings of the cross-sectional outer shapes of the girders from some of the world's longest suspension bridges are presented, in addition to a brief history of the evolution of suspension bridges.

## 2.2 Wind and Motion Induced Loads

When the wind flows around a non-static line-like structure, such as a bridge girder, a complex wind field occurs. The total pressure, relative pressure differences and interaction between the wind field and the moving girder, all induce forces on the girder. These forces can be divided into four parts [40]:

- Static forces due to the mean wind
- Fluctuating forces due to the phenomenon of vortex shedding
- Buffeting forces due to the turbulent wind
- Motion induced forces due to the interaction between the movement of the structure and the wind field

Since long-span suspension bridges have high flexibility, the motion induced forces play a significant role in the structural response of the bridge deck for higher wind velocities [14]. It is primarily this force contribution that is related to the phenomenon of aerodynamic instability.

### 2.2.1 Static Aerodynamic Forces

The static wind induced forces consist of the drag, lift and moment force components, which can be expressed as [40]:

$$F_D = \frac{1}{2}\rho(D \cdot L)V^2 \cdot C_D(\alpha) \quad (2.1a)$$

$$F_L = \frac{1}{2}\rho(B \cdot L)V^2 \cdot C_L(\alpha) \quad (2.1b)$$

$$M = \frac{1}{2}\rho(B \cdot L)V^2 \cdot C_M(\alpha) \quad (2.1c)$$

where D and B is the characteristic height and width of the cross section, respectively, while the pressure component  $\frac{1}{2}\rho V(t)^2$  results from Bernoulli's equation.  $C_D$ ,  $C_L$  and  $C_M$  are the static coefficients for drag, lift and moment, respectively. These are dependent of the rotation of the cross section,  $\alpha$ . The force components are visualized in figure 2.2.

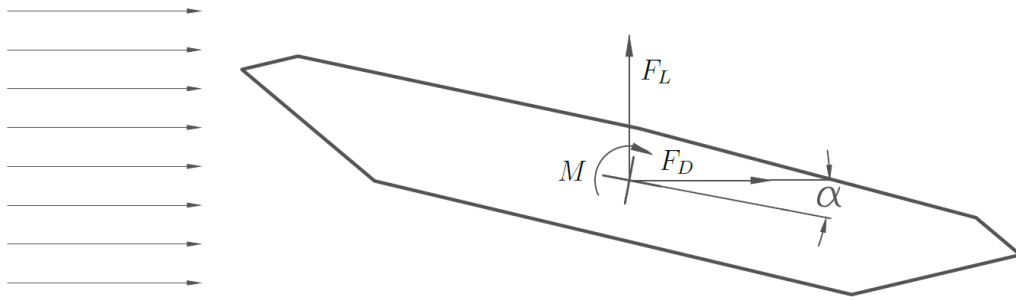


Figure 2.2: Drag, lift and moment force components

### 2.2.2 Vortex Shedding

The wind flow can lead to large alternating eddies forming behind the bridge girder, which is known as vortex shedding. These result in an alternating pressure gradient, which produces a fluctuation in the lift force of the girder. When the frequency of the alternating force coincides with the natural frequency of a vertical mode shape, a vertical oscillation of that mode shape can occur due to resonance. Vortex induced oscillations are usually not of a catastrophic nature, but can become problematic regarding the serviceability of the bridge, as well as related to fatigue [19].

### 2.2.3 Buffeting

Buffeting is the mechanism by which the the fluctuations in the oncoming wind cause the bridge to vibrate [19]. As with vortex shedding, these vibrations are usually not of catastrophic nature, but can cause serviceability and fatigue related issues. Buffeting would be included in a dynamic response analysis. However, this is not considered in this thesis, but is certainly relevant and is recommended as future work.

### 2.2.4 Self-Excited Forces

The self-excited forces occur as a result of the interaction between the wind flow and the motion of the girder. This effect is primarily associated with higher wind velocities. They are difficult to derive analytically as they depend on the structure shape, and are normally identified experimentally through wind tunnel testing. They can be described by the aerodynamic derivatives.

## 2.3 Modal Theory

As the girder is a line-like structure, its displacements  $\mathbf{r}$ , can be described as a function of the longitudinal coordinate,  $x$ , with a modal approach. The basic assumption behind a modal approach is that the structural displacements  $\mathbf{r}(x, t)$  can be represented by the sum of the products between the natural eigen-modes

$$\boldsymbol{\varphi}_i(x) = [\phi_y \quad \phi_z \quad \phi_\theta]_i^T \quad (2.2)$$

and the unknown exclusively time dependent functions,  $\eta_i(t)$ , i.e.

$$\mathbf{r}(x, t) = \Phi(x) \cdot \boldsymbol{\eta}(t) \quad (2.3)$$

where

$$\mathbf{r}(x, t) = [r_y \quad r_z \quad r_\theta]^T \quad (2.4)$$

$$\Phi(x) = [\boldsymbol{\varphi}_1 \dots \boldsymbol{\varphi}_i \dots \boldsymbol{\varphi}_{N_{mod}}] \quad (2.5)$$

$$\boldsymbol{\eta}(t) = [\eta_1 \dots \eta_i \dots \eta_{N_{mod}}] \quad (2.6)$$

The equation of motion can be expressed in the modal frequency domain as [40]:

$$\tilde{\mathbf{M}}_0 \ddot{\boldsymbol{\eta}}(t) + \tilde{\mathbf{C}}_0 \dot{\boldsymbol{\eta}}(t) + \tilde{\mathbf{K}}_0 \boldsymbol{\eta}(t) = \tilde{\mathbf{Q}}(t) + \tilde{\mathbf{Q}}_{ae}(t, \boldsymbol{\eta}, \dot{\boldsymbol{\eta}}, \ddot{\boldsymbol{\eta}}) \quad (2.7)$$

Here,  $\tilde{\mathbf{M}}_0$ ,  $\tilde{\mathbf{C}}_0$  and  $\tilde{\mathbf{K}}_0$  are the modal mass, modal damping and modal stiffness, respectively. These are defined as

$$\begin{aligned} \tilde{\mathbf{M}}_0 &= \text{diag}[\tilde{M}_i] & \tilde{M}_i &= \int_L \boldsymbol{\varphi}_i^T \cdot \mathbf{M}_0 \cdot \boldsymbol{\varphi}_i dx \\ \tilde{\mathbf{C}}_0 &= \text{diag}[\tilde{C}_i] & \tilde{C}_i &= 2\tilde{M}_i \omega_i \zeta_i \\ \tilde{\mathbf{K}}_0 &= \text{diag}[\tilde{K}_i] & \tilde{K}_i &= \omega_i^2 \tilde{M}_i \end{aligned} \quad (2.8)$$

where

$$\mathbf{M}_0 = \text{diag}[m_y(x) \quad m_z(x) \quad m_\theta(x)] \quad (2.9)$$

Here,  $\omega_i$  and  $\zeta_i$  are the natural frequency and the damping ratio associated with the eigenmode  $\boldsymbol{\varphi}_i$ .  $\mathbf{M}_0$  contains the cross sectional mass properties associated with the y, z and  $\theta$  degrees of freedom. In 2.7,  $\tilde{\mathbf{Q}}$  is the total modal wind load except the self-excited forces, while  $\tilde{\mathbf{Q}}_{ae}$  is the modal self-excited forces in a  $1 \times N_{mod}$  vector shapes, where each element is defined as

$$\tilde{\mathbf{Q}}_i = \int_{L_{exp}} \boldsymbol{\varphi}_i^T \cdot \mathbf{q} \quad dx \quad \tilde{\mathbf{Q}}_{aei} = \int_{L_{exp}} \boldsymbol{\varphi}_i^T \cdot \mathbf{q}_{Se} \quad dx \quad (2.10)$$

and the load vectors contain the total drag, lift and moment load per unit length

$$\mathbf{q}(x, t) = [q_y \quad q_z \quad q_\theta]^T \quad \mathbf{q}_{Se}(x, t) = [q_y \quad q_z \quad q_\theta]_{Se}^T \quad (2.11)$$

## 2.4 Aerodynamic Derivatives

The aerodynamic derivatives (ADs) are non-dimensional functions, dependent on the mean wind velocity and the frequency of motion of the bridge girder, that describe the self-excited forces. They depend on the external shape of the girder, and are usually determined through wind tunnel testing.

Theodorsen [41] was the first to develop theoretical formulations for the ADs, for thin aerofoils in 1935. This included 8 ADs, as presented later in equation 2.17. This was later expanded by R. Scanlan and J. Tomko in 1971, as they applied the ADs from a flat plate within bridge aerodynamics. The result was 18 ADs, that account for the interactions between the horizontal, vertical and torsional movement of the bridge girder. The 18 ADs,  $P_i^*, H_i^*$  and  $A_i^*$  ( $i=1-6$ ), are all seen in relation to the self-excited forces in degree of freedom (DOF)  $i$ ,  $q_i^{Se}$ , through equation 2.12 [26]:

$$q_x^{Se} = \frac{1}{2}\rho V^2 B \left( KP_1^* \frac{\dot{r}_y}{V} + KP_2^* \frac{B\dot{r}_\theta}{V} + K^2 P_3^* r_\theta + K^2 P_4^* \frac{r_y}{B} + KP_5^* \frac{\dot{r}_z}{V} + K^2 P_6^* \frac{r_z}{B} \right) \quad (2.12a)$$

$$q_z^{Se} = \frac{1}{2}\rho V^2 B \left( KH_1^* \frac{\dot{r}_z}{V} + KH_2^* \frac{B\dot{r}_\theta}{V} + K^2 H_3^* r_\theta + K^2 H_4^* \frac{r_z}{B} + KH_5^* \frac{\dot{r}_y}{V} + K^2 H_6^* \frac{r_y}{B} \right) \quad (2.12b)$$

$$q_\theta^{Se} = \frac{1}{2}\rho V^2 B \left( KA_1^* \frac{\dot{r}_z}{V} + KA_2^* \frac{B\dot{r}_\theta}{V} + K^2 A_3^* r_\theta + K^2 A_4^* \frac{r_z}{B} + KA_5^* \frac{\dot{r}_y}{V} + K^2 A_6^* \frac{r_y}{B} \right) \quad (2.12c)$$

where  $\omega$ ,  $B$  and  $V$  is the frequency of motion, the reference section width and the mean wind velocity.  $K$  is the reduced frequency, defined as

$$K = \frac{B\omega}{V} \quad (2.13a)$$

The ADs are further related to the structural stiffness and damping, respectively. Equation 2.12 can be expressed on the compact form

$$\mathbf{q}_{Se} = \mathbf{C}_{ae}\dot{\mathbf{r}} + \mathbf{K}_{ae}\mathbf{r} \quad (2.14)$$

where

$$\mathbf{K}_{ae} = \frac{\rho B^2}{2} \omega^2 \begin{bmatrix} P_4^* & P_6^* & BP_3^* \\ H_6^* & H_4^* & BH_3^* \\ BA_6^* & BA_4^* & B^2 A_3^* \end{bmatrix} \quad (2.15)$$

$$\mathbf{C}_{ae} = \frac{\rho B^2}{2} \omega \begin{bmatrix} P_1^* & P_5^* & BP_2^* \\ H_5^* & H_1^* & BH_2^* \\ BA_5^* & BA_1^* & B^2 A_2^* \end{bmatrix} \quad (2.16)$$

where  $\mathbf{K}_{ae}$  and  $\mathbf{C}_{ae}$  are the aerodynamic stiffness and damping matrices.

The expressions for the self-excited forces given by equation 2.12 are only valid for a single harmonic motion in one DOF, but an arbitrary motion can be obtained under the assumption that the principle of superposition holds [7].

There has been made efforts to determine how the aerodynamic derivatives influence the



critical wind speed in terms of the flutter phenomena. There is a general agreement that the critical ADs for this are  $H_1^*$ ,  $H_3^*$ ,  $A_1^*$ ,  $A_2^*$  and  $A_3^*$ . Table 2.1 summarizes their effect on coupled flutter [43]:

Table 2.1: ADs effect on flutter

AD	Stabilizing	Destabilizing
$A_1^*$	Low absolute values	High absolute values
$A_2^*$	Negative values	Positive values
$A_3^*$	Low absolute values	High absolute values
$H_1^*$	Negative values	Positive values
$H_3^*$	Low absolute values	High absolute values

### 2.4.1 Theodorsen's Aerodynamic Derivatives

This thesis adopts the ADs derived by Theodorsen as a reference to the presented ADs resulting from the conducted wind tunnel tests. In the derivations of these, Theodorsen made several assumptions. For one, non-stationary potential flow theory is applied when deriving the wind forces acting on the section. Further, at least two DOFs are assumed sufficient to obtain instability, and only small oscillatory motions around the state of equilibrium are considered. Theodorsen focused on describing the mechanism of flutter, and therefore, secondary effects as varying section shape was not considered.

Theodorsen's theoretical aerodynamic derivatives for an ideal flat plate are given by [40]:

$$\begin{bmatrix} H_1^* & A_1^* \\ H_2^* & A_2^* \\ H_3^* & A_3^* \\ H_4^* & A_4^* \end{bmatrix} = \begin{bmatrix} -2\pi F V_{red} & -\frac{\pi}{2} F V_{red} \\ \frac{\pi}{2}(1 + F + 4G V_{red}) V_{red} & -\frac{\pi}{8}(1 - F - 4G V_{red}) V_{red} \\ 2\pi(F V_{red} - \frac{G}{4}) V_{red} & \frac{\pi}{2}(F V_{red} - \frac{G}{4}) V_{red} \\ \frac{\pi}{2}(1 + 4G V_{red}) & \frac{\pi}{2} G V_{red} \end{bmatrix} \quad (2.17)$$

where

$$F\left(\frac{\hat{\omega}_i}{2}\right) = \frac{J_1 \cdot (J_1 + Y_0) + Y_1 \cdot (Y_1 - J_0)}{(J_1 + Y_0)^2 + (Y_1 - J_0)^2} \quad (2.18a)$$

$$G\left(\frac{\hat{\omega}_i}{2}\right) = \frac{J_1 \cdot J_0 + Y_1 - Y_0}{(J_1 + Y_0)^2 + (Y_1 - J_0)^2} \quad (2.18b)$$

are Theodorsen's circulatory functions, where  $J_n$  and  $Y_n$  are the first and second kinds of Bessel functions with order  $n$ .  $\hat{\omega}_i$  is the non-dimensional resonance frequency.

## 2.5 Motion Induced Instabilities

The majority of the theory presented in this section is based on Chapter 8 in *Theory of Bridge Aerodynamics*, by E. Strømmen [40].

There are four different types of aerodynamic instability phenomena that can occur for suspension bridges. These are:

- Static Divergence
- Galloping
- Dynamic Stability in Torsion
- Flutter

The lowest wind speed at which one of these instabilities occur is referred to as the critical wind speed,  $V_{cr}$ , or the aerodynamic stability limit. As previously mentioned, these instabilities are directly related to the self-excited forces of the bridge girder, which are described by the aerodynamic derivatives. Equation 2.7 can be rewritten to enlighten the effect of the aerodynamic damping and stiffness  $\mathbf{C}_{ae}$ ,  $\mathbf{K}_{ae}$ , in the equation of motion:

$$\tilde{\mathbf{M}}_0 \ddot{\eta}(t) + (\tilde{\mathbf{C}}_0 - \tilde{\mathbf{C}}_{ae}(V, \omega)) \dot{\eta}(t) + (\tilde{\mathbf{K}}_0 - \tilde{\mathbf{K}}_{ae}(V, \omega)) \eta(t) = 0 \quad (2.19)$$

This structural system is velocity- and frequency-dependent. The characteristic eigenvalue problem from equation 2.19 have several formulations, and this thesis presents the formulation from by Einar Strømmen. Here, the response of a modal dynamic system is described by the response function

$$\hat{\mathbf{H}}_{\eta}(\omega, V) = \left( \mathbf{I} - \boldsymbol{\kappa}_{ae} - \left( \omega \cdot \text{diag} \left[ \frac{1}{\omega_i} \right] \right)^2 + 2i\omega \cdot \text{diag} \left[ \frac{1}{\omega_i} \right] \cdot (\boldsymbol{\zeta} - \boldsymbol{\zeta}_{ae}) \right)^{-1} \quad (2.20)$$

where  $\mathbf{I}$  is the identity matrix,  $\boldsymbol{\zeta}$  is a diagonal matrix of  $\zeta_i$  containing the damping ratio for the respective mode,  $\boldsymbol{\varphi}_i$ , and  $\omega_i$  is the in-wind resonance frequency for the respective mode,  $\boldsymbol{\varphi}_i$ . The members of the matrices  $\boldsymbol{\kappa}_{ae}$  and  $\boldsymbol{\zeta}_{ae}$  are defined as

$$\kappa_{aeij} = \frac{\tilde{K}_{aeij}}{\omega_i^2 \tilde{M}_i} = \frac{\rho B^2}{2\tilde{m}_i} \cdot \left[ \frac{\omega}{\omega_i} \right]^2 \cdot \frac{\int_{L_{exp}} (\boldsymbol{\varphi}_i^T \cdot \hat{\mathbf{K}}_{ae} \cdot \boldsymbol{\varphi}_j) dx}{\int_L (\boldsymbol{\varphi}_i^T \cdot \boldsymbol{\varphi}_i) dx} \quad (2.21)$$

$$\zeta_{aeij} = \frac{\omega_i}{2} \cdot \frac{\tilde{C}_{aeij}}{\omega_i^2 \tilde{M}_i} = \frac{\rho B^2}{4\tilde{m}_i} \cdot \frac{\omega}{\omega_i} \cdot \frac{\int_{L_{exp}} (\boldsymbol{\varphi}_i^T \cdot \hat{\mathbf{C}}_{ae} \cdot \boldsymbol{\varphi}_j) dx}{\int_L (\boldsymbol{\varphi}_i^T \cdot \boldsymbol{\varphi}_i) dx} \quad (2.22)$$

The stability limit of such a system is expressed by the critical wind speed,  $V_{cr}$  and a corresponding critical frequency  $\omega_{cr}$ , where the response of the system becomes unstable. This occurs as the determinant of the impedance function,  $\hat{\mathbf{E}}_{\eta}(\omega, V)$ , goes to zero. Therefore, the stability limit can be found by evaluating the impedance function.

$$\hat{\mathbf{E}}_{\eta}(\omega, V) = \hat{\mathbf{H}}_{\eta}(\omega, V)^{-1} = \left( \mathbf{I} - \boldsymbol{\kappa}_{ae} - \left( \omega \cdot \text{diag} \left[ \frac{1}{\omega_i} \right] \right)^2 + 2i\omega \cdot \text{diag} \left[ \frac{1}{\omega_i} \right] (\boldsymbol{\zeta} - \boldsymbol{\zeta}_{ae}) \right) \quad (2.23)$$

By evaluating the impedance function, one can observe that  $\boldsymbol{\kappa}_{ae}$  and  $\boldsymbol{\zeta}_{ae}$  are the components able to cause instability. The dimensions of all the matrices in 2.23 are given by the

number of modes of the system,  $N_{mod} \times N_{mod}$ . The solution of the eigenvalue problem will result in  $N_{mod}$  stability limits for the respective mode shapes,  $\varphi_i$ . As  $\hat{\mathbf{E}}$  contains complex quantities, 2.24 implies the simultaneous conditions of 2.25 and 2.26.

$$\left| \det \left( \hat{\mathbf{E}}_\eta(\omega, V) \right) \right| = 0 \quad (2.24)$$

$$\operatorname{Re} \left( \det \left( \hat{\mathbf{E}} \right) \right) = 0 \quad (2.25) \quad \operatorname{Im} \left( \det \left( \hat{\mathbf{E}} \right) \right) = 0 \quad (2.26)$$

Observing the eigenvalues resulting from solving 2.24, they consist of pairs of  $\omega$  and values of  $V$ . For a static limit where  $\omega = 0$ , it is simply defined by a critical wind speed,  $V_{cr}$ . Considering the dynamic stability, the response is assumed narrow-banded around either the in-wind preference frequency or the resonance frequency for a certain mode or mode combination. Out of all of the eigenvalues resulting from solving 2.24, the lowest value of  $V_{cr}$  with the associated  $\omega_r$  will determine the overall critical wind speed.

The four instability phenomena are described in the following subsections. In common for them all is that it is either the vertical motion  $r_z$ , or the torsional motion  $r_\theta$ , or both, that are the dominating response quantities in  $\mathbf{r}(x, t) = [r_y \ r_z \ r_\theta]^T$ . Further, a decent estimate for the stability limit can be provided with only two modes. However, the thesis has included several modes, in order to investigate the stability limit in a greater detail. It is still useful to express analytical solutions only considering the first two modes  $\varphi_1$  and  $\varphi_2$  and their associated eigen-frequencies  $\omega_1$  and  $\omega_2$ . One of these modes containing a dominant component of  $\phi_z$  and the other containing a dominant component of  $\phi_\theta$ . Simplifying the calculations, the modes can be described as

$$\varphi_1(x) \approx [0 \ \phi_z \ 0]^T \quad (2.27)$$

$$\varphi_2(x) \approx [0 \ 0 \ \phi_\theta]^T \quad (2.28)$$

By implementing this in the impedance matrix, it can be reduced to

$$\hat{\mathbf{E}}_\eta(\omega_r, V_{cr}) = \begin{bmatrix} 1 & 0 \\ 0 & 1 \end{bmatrix} - \begin{bmatrix} \kappa_{ae_{zz}} & \kappa_{ae_{z\theta}} \\ \kappa_{ae_{\theta z}} & \kappa_{ae_{\theta\theta}} \end{bmatrix} - \begin{bmatrix} (\omega_r/\omega_z)^2 & 0 \\ 0 & (\omega_r/\omega_\theta)^2 \end{bmatrix} \quad (2.29)$$

$$+ 2i \begin{bmatrix} \omega_r/\omega_z & 0 \\ 0 & \omega_r/\omega_\theta \end{bmatrix} \cdot \begin{bmatrix} \zeta_z - \zeta_{ae_{zz}} & -\zeta_{ae_{z\theta}} \\ -\zeta_{ae_{\theta z}} & \zeta_\theta - \zeta_{ae_{\theta\theta}} \end{bmatrix} \quad (2.30)$$

where

$$\kappa_{ae_{zz}} = \frac{\rho B^2}{2\tilde{m}_z} \left[ \frac{\omega_r}{\omega_z} \right]^2 H_4^* \frac{\int_{L_{exp}} \phi_z^2 dx}{\int_L \phi_z^2 dx} \quad (2.31)$$

$$\kappa_{ae_{z\theta}} = \frac{\rho B^3}{2\tilde{m}_z} \left[ \frac{\omega_r}{\omega_z} \right]^2 H_3^* \frac{\int_{L_{exp}} \phi_z \phi_\theta dx}{\int_L \phi_z^2 dx} \quad (2.32)$$

$$\kappa_{ae_{\theta\theta}} = \frac{\rho B^4}{2\tilde{m}_\theta} \left[ \frac{\omega_r}{\omega_\theta} \right]^2 A_3^* \frac{\int_{L_{exp}} \phi_\theta^2 dx}{\int_L \phi_\theta^2 dx} \quad (2.33)$$

$$\kappa_{ae_{\theta z}} = \frac{\rho B^3}{2\tilde{m}_\theta} \left[ \frac{\omega_r}{\omega_\theta} \right]^2 A_4^* \frac{\int_{L_{exp}} \phi_\theta \phi_z dx}{\int_L \phi_\theta^2 dx} \quad (2.34)$$

$$\zeta_{ae_{zz}} = \frac{\rho B^2}{4\tilde{m}_z} \frac{\omega_r}{\omega_z} H_1^* \frac{\int_{L_{exp}} \phi_z^2 dx}{\int_L \phi_z^2 dx} \quad (2.35)$$

$$\zeta_{ae_{z\theta}} = \frac{\rho B^3}{4\tilde{m}_z} \frac{\omega_r}{\omega_z} H_2^* \frac{\int_{L_{exp}} \phi_z \phi_\theta dx}{\int_L \phi_z^2 dx} \quad (2.36)$$

$$\zeta_{ae_{\theta\theta}} = \frac{\rho B^4}{4\tilde{m}_\theta} \frac{\omega_r}{\omega_\theta} A_2^* \frac{\int_{L_{exp}} \phi_\theta^2 dx}{\int_L \phi_\theta^2 dx} \quad (2.37)$$

$$\zeta_{ae_{\theta z}} = \frac{\rho B^3}{4\tilde{m}_\theta} \frac{\omega_r}{\omega_\theta} A_1^* \frac{\int_{L_{exp}} \phi_\theta \phi_z dx}{\int_L \phi_\theta^2 dx} \quad (2.38)$$

where  $\omega_r$  are the resonance frequency. Establishing this reduced impedance function is useful when reviewing the four different types of structural behaviour close to the instability limit.

### 2.5.1 Static Divergence

The mode shape of static divergence in torsion can be simplified as

$$\varphi_2(x) \approx [0 \quad 0 \quad \phi_\theta]^T \quad (2.39)$$

when considering the static instability limit,  $\omega_r = 0$ . Implementing this into 2.30 yields

$$\hat{E}_\eta(\omega_r = 0, V_{cr}) = 1 - \kappa_{ae\theta\theta} \quad (2.40)$$

This is not a dynamic problem, so the quasi-static value of  $A_3^*$  can be applied. As 2.40 goes to zero when  $\kappa_{ae\theta\theta} = 1$ , the critical wind speed for static divergence can be derived from 2.33, as:

$$V_{cr} = B \cdot \omega_\theta \cdot \sqrt{\frac{2\tilde{m}_\theta}{\rho B^4 C'_M} \cdot \frac{\int_L \phi_\theta^2 dx}{\int_{L_{exp}} \phi_\theta^2 dx}} \quad (2.41)$$

### 2.5.2 Galloping

The mode shape for galloping has the lowest eigen-frequency,  $\omega_1 = \omega_z$ , with a main component of  $\phi_z$ , and can be simplified as

$$\varphi_1(x) \approx [0 \quad \phi_z \quad 0]^T \quad (2.42)$$

As the resonance frequency related to the galloping mode is  $\omega_z(V_{cr})$ , this can be inserted into equation 2.30, to reduce the impedance matrix to

$$\hat{E}_\eta(\omega_r, V_{cr}) = 1 - \kappa_{aezz} - (\omega_r/\omega_z)^2 + 2i(\zeta_z - \zeta_{aezz})\omega_r/\omega_z \quad (2.43)$$

where  $\kappa_{aezz}$  and  $\zeta_{aezz}$  is defined in 2.31 and 2.35, respectively. By setting both the real and imaginary part of 2.43 equal to zero the dynamic stability limit can be identified

$$\omega_r = \omega_z \left( 1 + \frac{\rho B^2}{2\tilde{m}_z} \cdot H_4^* \frac{\int_{L_{exp}} \phi_z^2 dx}{\int_L \phi_z^2 dx} \right)^{-1/2} \quad (2.44)$$

when

$$\zeta_z = \zeta_{aezz} = \frac{\rho B^2}{4\tilde{m}_z} \cdot \frac{\omega_r}{\omega_z} H_1^* \frac{\int_{L_{exp}} \phi_z^2 dx}{\int_L \phi_z^2 dx} \quad (2.45)$$

From this, one can observe that galloping instability will only occur if  $H_1^*$  attains positive values.

### 2.5.3 Dynamic stability limit in torsion

As for the static divergence, the mode shape for this instability can be described as

$$\varphi_2(x) \approx [0 \quad 0 \quad \phi_\theta]^T \quad (2.46)$$

However, in a dynamic instability the respective eigen-frequency is the lowest where  $\phi_\theta$  is the dominating component,  $\omega_2 = \omega_\theta$ . Applying this into 2.30, the impedance function is reduced to

$$\hat{E}_\eta(\omega_r, V_{cr}) = 1 - \kappa_{ae\theta\theta} - (\omega_r/\omega_\theta)^2 + 2i(\zeta_\theta - \zeta_{ae\theta\theta})\omega_r/\omega_\theta \quad (2.47)$$

where  $\kappa_{ae\theta\theta}$  and  $\zeta_{ae\theta\theta}$  is defined in 2.33 and 2.37, respectively. Again, by setting the real and imaginary part of 2.47 equal to zero, the dynamic stability limit can be identified by

$$\omega_r = \omega_\theta \left( 1 + \frac{\rho B^4}{2\tilde{m}_\theta} \cdot A_3^* \frac{\int_{L_{exp}} \phi_\theta^2 dx}{\int_L \phi_\theta^2 dx} \right)^{-1/2} \quad (2.48)$$

when

$$\zeta_\theta = \zeta_{ae\theta\theta} = \frac{\rho B^4}{4\tilde{m}_\theta} \cdot \frac{\omega_r}{\omega_\theta} A_2^* \frac{\int_{L_{exp}} \phi_\theta^2 dx}{\int_L \phi_\theta^2 dx} \quad (2.49)$$

From this, one can observe that instability in pure torsion will only occur if  $A_2^*$  attains positive values.

## 2.5.4 Flutter

Flutter is the dynamic instability phenomenon where  $r_z$  and  $r_\theta$  couples. This coupling occurs via  $\kappa_{ae\theta z}$  and  $\kappa_{aez\theta}$  in the impedance function 2.30, and is therefore most likely to occur between modes  $\varphi_1$  and  $\varphi_2$  with main components of  $\phi_z$  and  $\phi_\theta$ , respectively. Further,  $r_z$  and  $r_\theta$  couples and obtain the same resonant frequency

$$\omega_r = \omega_z = \omega_\theta \quad (2.50)$$

Computing the critical wind speed for this case becomes easier if the impedance function is split into four parts

$$\hat{\mathbf{E}}_\eta(\omega, V) = \hat{\mathbf{E}}_1 + \hat{\mathbf{E}}_2 + 2i(\hat{\mathbf{E}}_3 + \hat{\mathbf{E}}_4) \quad (2.51)$$

where

$$\hat{\mathbf{E}}_1 = \begin{bmatrix} 1 - \kappa_{aezz} - (\omega_r/\omega_z)^2 & 0 \\ -\kappa_{ae\theta z} & 0 \end{bmatrix} \quad (2.52)$$

$$\hat{\mathbf{E}}_2 = \begin{bmatrix} 0 & -\kappa_{aez\theta} \\ 0 & 1 - \kappa_{ae\theta\theta} - (\omega_r/\omega_\theta)^2 \end{bmatrix} \quad (2.53)$$

$$\hat{\mathbf{E}}_3 = \begin{bmatrix} (\zeta_z - \zeta_{aezz}) \cdot \omega_r/\omega_z & 0 \\ -\zeta_{ae\theta z} \cdot \omega_r/\omega_\theta & 0 \end{bmatrix} \quad (2.54)$$

$$\hat{\mathbf{E}}_4 = \begin{bmatrix} 0 & -\zeta_{aez\theta} \cdot \omega_r/\omega_z \\ 0 & (\zeta_\theta - \zeta_{ae\theta\theta}) \cdot \omega_r/\omega_\theta \end{bmatrix} \quad (2.55)$$

With all quantities given in 2.31-2.37. Again, both the real and imaginary part of 2.51 are set to zero to identify the critical wind speed.

$$\operatorname{Re} \left( \det \left( \hat{\mathbf{E}}_{\eta} \right) \right) = \det \left( \hat{\mathbf{E}}_1 + \hat{\mathbf{E}}_2 \right) - 4 \cdot \det \left( \hat{\mathbf{E}}_3 + \hat{\mathbf{E}}_4 \right) \quad (2.56)$$

$$\operatorname{Im} \left( \det \left( \hat{\mathbf{E}}_{\eta} \right) \right) = 2 \cdot \left[ \det \left( \hat{\mathbf{E}}_1 + \hat{\mathbf{E}}_4 \right) + \det \left( \hat{\mathbf{E}}_2 + \hat{\mathbf{E}}_3 \right) \right] \quad (2.57)$$

As the ADs are dependent on  $\omega_r$  and  $V_{cr}$ , solving 2.56 and 2.57 demands iterations until convergence. If the ratio  $\omega_r/\omega_z$  is higher than 1.5, Selberg's formula can be useful to provide a first estimate of the flutter stability [40] [32].

$$V_{cr} = 0.6B\omega_{\theta} \cdot \sqrt{\left[ 1 - \frac{\omega_r^2}{\omega_{\theta}^2} \right] \cdot \frac{\sqrt{\tilde{m}_z \tilde{m}_{\theta}}}{\rho B^3}} \quad (2.58)$$

However, for the estimation of critical wind speed in this thesis, a multi-mode approach is performed.

### 2.5.5 Multi-modal Flutter

While the bi-modal approach does provide reasonable approximations of the critical wind speed, it is widely recognized that a multi-modal approach provides more accurate results. Also, when analysing the instability behaviour, a higher number of DOFs, in this case modes, will improve the accuracy of the prediction.

The multi-modal approach does not make assumptions regarding the mode shapes, so all three components are included:

$$\boldsymbol{\varphi}_i(x) = [\phi_y \quad \phi_z \quad \phi_{\theta}]^T \quad (2.59)$$

As all three components are included, the expressions for  $\kappa_{aeij}$  and  $\zeta_{aeij}$  in equations 2.21 and 2.22 are expanded. This is a tedious exercise and is omitted for the theory presented in this thesis.

By assuming a solution on form  $\eta = \Phi e^{\lambda t}$  one can rewrite equation of motion 2.19 as the following

$$\left( \lambda^2 \tilde{\mathbf{M}}_0 + \lambda (\tilde{\mathbf{C}}_0 - \tilde{\mathbf{C}}_{ae}) + (\tilde{\mathbf{K}}_0 - \tilde{\mathbf{K}}_{ae}) \right) \boldsymbol{\varphi} = \mathbf{0} \quad (2.60)$$

The resulting complex eigenvalues of the corresponding eigenvalue problem is on the form

$$\lambda_n = -\zeta_n \omega_n + -i \omega_n \sqrt{1 - \zeta_n^2} \quad (2.61)$$

where  $\omega_n$   $\zeta_n$  is the still-wind frequency, and damping ratio. As seen, a solution to equation 2.60 appears when the real part of equation 2.61 reaches zero. This is obtained when the in-wind damping ratio is negative.

Iterations are required to solve equation 2.60, as the aerodynamic stiffness and damping,  $\mathbf{K}_{ae}$  and  $\mathbf{C}_{ae}$ , both depend on the mean wind velocity and the frequency. The process of iterations is explained in section 2.9.

## 2.6 Wind Tunnel Testing

Wind tunnel testing is a necessary tool for estimating aerodynamic stability in long-span bridge design. Wind tunnel tests are commonly performed on either full bridge models, or on section models of the girder. Full models have the advantage of a realistic reproduction of the interaction between aerodynamic forces and all parts of the structure, and are often used to evaluate the overall performance of new bridge concepts [7]. The disadvantage of the full models is that they have to be made in a small scale to fit inside the wind tunnel, which requires a high degree of accuracy and may lead to scaling effects becoming an issue. Section models can be of larger scale, and are therefore less prone to aerodynamic scale effects [19, p533]. In addition, they are less demanding to manufacture. Therefore, section models are the most widely used alternative.

There are two major types of wind tunnel testing methods; free vibration and forced vibration. In free vibration tests, the girder section is suspended on springs, and vibrates due to initial conditions and interaction with the wind flow. In forced vibration, the girder section is forced into a prescribed oscillatory motion by rigs on each end, while under wind flow. Both methods can be used to determine AD's of bridge girder cross-sections. While the free vibration tests are more capable of providing realistic in-wind vibrations, the forced vibration tests generally provide higher data reliability and are more suitable for higher wind velocities [7].

NTNU acquired a new enhanced forced vibration wind tunnel test rig in 2017. Historically, forced vibration test rigs have only been capable of generating sinusoidal motions, which cannot reflect real bridge behaviour [7]. However, this enhanced rig is designed to be able to move the section model in any arbitrary motion. This motion can be generated in any of the three degrees of freedom; horizontal, vertical and torsion. The load cells of the rig can measure three forces and three moments at each end of the section model.

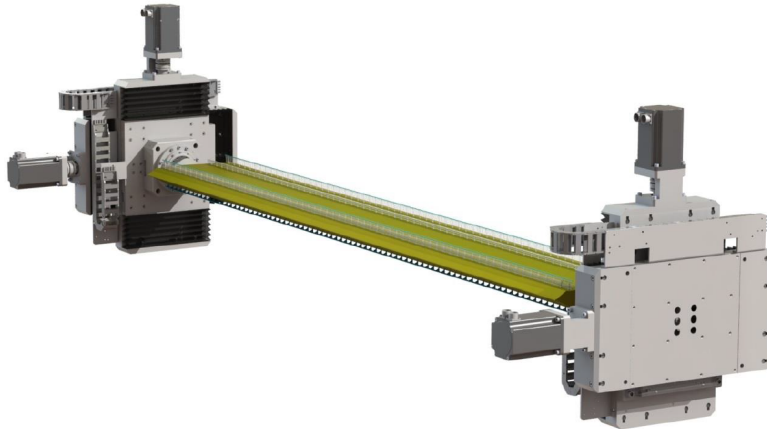


Figure 2.3: NTNU forced vibration rig. The section model is mounted between the two actuators.

The rig and testing system was proven to have an excellent performance when extracting ADs for the Hardanger Bridge cross section [7].

### 2.6.1 Wind Tunnel Effects

This subsection is inspired by the master thesis *Wind Tunnel Testing of Bridge Decks* from 2016 [1], which reported extensively on the wind tunnel at the Fluid Mechanics Lab-

oratory at NTNU. This is an advantage, as experimental set-ups in different wind tunnels do vary.

By placing an object in a closed-section wind tunnel, the flow of the air will be disturbed. This is due to mass conservation, meaning that the wind will accelerate and flow along the object at a higher speed, which is known as the blockage effect. This is a source of uncertainty that must be considered when designing the experimental set up. At NTNU the following correction for measured forces is used:

$$\frac{F_c}{F_m} = 1 - \frac{\sin(|\theta|)}{\cos(|\alpha|)} \cdot k \frac{S}{A} \quad (2.62)$$

where c and m denotes corrected and measured forces,  $\alpha$  is the rotated angle of the section model,  $S$  is the wake area of the model, and  $A$  is the cross sectional area of the wind tunnel.  $k$  is a constant. The ratio  $S/A$  should not be higher than 6% [16].

It is important to maintain a 2-dimensional flow along the section model. This can be ensured with large end plates. As the bridge deck models in this thesis span over the whole width of the tunnel, this should not be a problem. However, this also means that the boundary layer along the walls must be considered. At the wind tunnel at NTNU, the boundary layer cease to exist 200 mm from the panels. As the total width of the tunnel is 2.7 m, the bounadary layers does not affect the overall flow significantly.

The Reynolds Number,  $Re$ , is a dimensionless quantity, which expresses the ratio of the inertial forces and the viscous forces in a fluid:

$$Re = \frac{V \rho D}{\mu} \quad (2.63)$$

$V$ ,  $\rho$ ,  $D$  and  $\mu$  is the fluid velocity, fluid density, the height of the section model and the dynamic viscosity. Studies show that the aerodynamic force coefficients and the general response amplitude are affected by a change of Reynolds number, also for cross sections with sharp edges as the section models. Therefore, it is advised that the Reynolds number should be above  $10^4$  during the wind tunnel test. Testing the sections for several wind speeds will reveal if the section model show Reynolds number dependency, which will add uncertainty to the results.

## 2.7 Identification of Static Coefficients

Quasi-static wind tunnel tests can be performed to determine the static coefficients  $C_D$ ,  $C_L$  and  $C_M$ , at different rotational angles  $\alpha$ . These coefficients determine the static aerodynamic forces on the bridge deck, as given in equation 2.1. Expressing these formulas for the coefficients give:

$$C_D(\alpha) = \frac{F_{D_{ae}}}{\frac{1}{2} \cdot \rho(D \cdot L) \cdot V^2} \quad (2.64a)$$

$$C_L(\alpha) = \frac{F_{L_{ae}}}{\frac{1}{2} \cdot \rho(B \cdot L) \cdot V^2} \quad (2.64b)$$

$$C_M(\alpha) = \frac{M_{ae}}{\frac{1}{2} \cdot \rho B(B \cdot L) \cdot V^2} \quad (2.64c)$$



The total forces on a section model during the wind tunnel test can be expressed as:

$$F_D = F_{D_{inertia}} + F_{D_{ae}} \quad (2.65a)$$

$$F_L = G + F_{L_{inertia}} + F_{L_{ae}} \quad (2.65b)$$

$$M = G \cdot e_H + F_D \cdot e_V + F_L \cdot M_{inertia} + M_{ae} \quad (2.65c)$$

where  $F_D$ ,  $F_L$  and  $M$  are the measured drag force, lift and pitching moment, and  $F_{D_{ae}}$ ,  $F_{L_{ae}}$  and  $M_{ae}$  are the static aerodynamic forces.  $F_{D_{inertia}}$ ,  $F_{L_{inertia}}$  and  $M_{inertia}$  are the inertia forces. These inertia force contributions should be small in a quasi-static test, but should either way be considered. Further,  $G$  is the gravitational force, and  $e_H$  and  $e_V$  are eccentricities to the shear center in horizontal and vertical directions, and  $\cdot$ . The static aerodynamic forces are thus extracted as:

$$F_{D_{ae}} = F_D - F_{D_{inertia}} \quad (2.66a)$$

$$\implies F_{L_{ae}} = F_L - G - F_{L_{inertia}} \quad (2.66b)$$

$$M_{ae} = M - G \cdot e_H - F_D \cdot e_V - F_L \cdot M_{inertia} \quad (2.66c)$$

By rotating the sections in a quasi static (slow) rotation speed, one can thus identify static coefficients for wind flow at different angles to the girder.

## 2.8 Identification of Aerodynamic Derivatives

There are several known methods to identify ADs by wind tunnel tests. One common way is to study the phase angle between the self-excited forces and the motion of the section. Another method is to consider the complex Fourier amplitudes of the self-excited forces and how these are related to the ADs [7]. However, these methods can have significant errors, due to inaccurate phase angle estimates or spectral leakage [7]. Another approach is the time domain method where the equations for the self-excited forces given in 2.12 are fitted to the time series of the measured self excited forces by least squares [7]. In order to do this, the self-excited forces must be identified from the wind tunnel test data. This is the method applied in this thesis, with forced vibration wind tunnel tests.

The total forces acting on a section model can be expressed by [7]:

$$\mathbf{Q}_{tot}(\mathbf{r}, \dot{\mathbf{r}}, \ddot{\mathbf{r}}, V, u, w) = \mathbf{Q}_G + \mathbf{Q}_I(\dot{\mathbf{r}}) + \mathbf{Q}_B(V, u, w) + \mathbf{Q}_{Se}(V, \dot{\mathbf{r}}, \ddot{\mathbf{r}}) + \mathbf{Q}_S(V) \quad (2.67)$$

Where  $\mathbf{Q}_G$  is the static gravitational load of self weight,  $\mathbf{Q}_I$  is the inertia forces from the forced motion,  $\mathbf{Q}_B$  is the buffeting forces,  $\mathbf{Q}_{Se}$  is the self-excited forces and  $\mathbf{Q}_S$  is the static wind load. Each of these quantities have three components, namely the force in each DOF.

To extract the self-excited forces, the other load contributions must be subtracted from the measured total load, similar to in 2.66. The static loads  $\mathbf{Q}_G$  and  $\mathbf{Q}_S$  are subtracted by simply removing the mean values in the measured load time series. The buffeting forces can be neglected for the tests in this thesis, because the wind tunnel testing is conducted with a laminar flow. Further, the inertia forces are measured through still-wind tests with the same motion-series as used in the in-wind tests. By subtracting all these contributions from the total measured load  $\mathbf{Q}_{tot}$ , the self-excited forces are obtained.

The testing in this thesis is divided into single harmonic motion in the three DOFs, respectively. Each of these tests are capable of identifying the 6 ADs corresponding to this motion, which summarizes to the total 18 ADs. Further, the single DOF harmonic motion

tests can be conducted with different values for wind speed  $V$  and oscillation frequency  $f$ , in order to obtain a ADs for a range of  $V_{red}$ . Further, a data fitting procedure can be executed on these AD data points to find 18 functions for the 18 ADs.

By rewriting equation 2.12, the self-excited forces can be expressed in terms of the AD's as follows:

$$\mathbf{q}_{Se}(t, K, V) = \mathbf{X}_y \mathbf{E}_y + \mathbf{X}_z \mathbf{E}_z + \mathbf{X}_\theta \mathbf{E}_\theta = [q_y^{Se}, q_z^{Se}, q_\theta^{Se}] \quad (2.68)$$

where:

$$\mathbf{E}_y = \frac{1}{2} \rho V^2 B \begin{bmatrix} KP_1^*/V & KH_5^*/V & BKA_5^*/V \\ K^2P_4^*/V & K^2H_6/B & K^2A_6^* \end{bmatrix} \quad (2.69a)$$

$$\mathbf{E}_z = \frac{1}{2} \rho V^2 B \begin{bmatrix} KP_5^*/V & KH_1^*/V & BKA_1^*/V \\ K^2P_6/B & K^2H_4^*/B & K^2A_4^* \end{bmatrix} \quad (2.69b)$$

$$\mathbf{E}_\theta = \frac{1}{2} \rho V^2 B \begin{bmatrix} BKP_2^*/V & BKH_2^*/V & B^2KA_2^*/V \\ K^2P_3^* & K^2H_3^* & BK^2A_3^* \end{bmatrix} \quad (2.69c)$$

$$\mathbf{X}_y, \mathbf{X}_z, \mathbf{X}_\theta = \begin{bmatrix} \dot{r}_{y,1} & r_{y,1} \\ \dot{r}_{y,2} & r_{y,2} \\ \vdots & \vdots \\ \dot{r}_{y,n} & r_{y,n} \end{bmatrix} \begin{bmatrix} \dot{r}_{z,1} & r_{z,1} \\ \dot{r}_{z,2} & r_{z,2} \\ \vdots & \vdots \\ \dot{r}_{z,n} & r_{z,n} \end{bmatrix}, \begin{bmatrix} \dot{r}_{\theta,1} & r_{\theta,1} \\ \dot{r}_{\theta,2} & r_{\theta,2} \\ \vdots & \vdots \\ \dot{r}_{\theta,n} & r_{\theta,n} \end{bmatrix} \quad (2.70)$$

$$\mathbf{q}_{Se,i} = \begin{bmatrix} q_{Se,y,1} & q_{Se,z,1} & q_{Se,\theta,1} \\ q_{Se,y,2} & q_{Se,z,2} & q_{Se,\theta,2} \\ \vdots & \vdots & \vdots \\ q_{Se,y,n} & q_{Se,z,n} & q_{Se,\theta,n} \end{bmatrix}, i \quad (2.71)$$

Here,  $\mathbf{E}_i$  are the coefficient matrices containing the ADs corresponding to motion in DOF  $i$ ,  $\mathbf{X}_i$  are the matrices containing the motion history of DOF  $i$ , and  $\mathbf{q}_{Se,i}$  is the measured self-excited forces for the tested oscillation in DOF  $i$ . Also, "n" denotes sample number in the time series.

Further, the ADs are obtained by minimizing the respective sum of squares:

$$\mathbf{E}_y = (\mathbf{X}_y^T \mathbf{X}_y)^{-1} \mathbf{X}_y^T \mathbf{q}_{Se,y} \quad (2.72a)$$

$$\mathbf{E}_z = (\mathbf{X}_z^T \mathbf{X}_z)^{-1} \mathbf{X}_z^T \mathbf{q}_{Se,z} \quad (2.72b)$$

$$\mathbf{E}_\theta = (\mathbf{X}_\theta^T \mathbf{X}_\theta)^{-1} \mathbf{X}_\theta^T \mathbf{q}_{Se,\theta} \quad (2.72c)$$

This data fitting procedure is executed for the particular value of the reduced wind velocity,  $V_{red}$ .

## 2.9 Computation of Critical Wind Speed

This section describes the computational program applied in this thesis to estimate the critical wind speed  $V_{cr}$ . As mentioned in section 2.5, an iterative solution procedure is required to estimate the critical wind speed related to flutter. The program used is a multi-mode approach, and the entire program described by the algorithm presented in the following.

The algorithm takes the modal properties  $\Phi$ ,  $\tilde{\mathbf{M}}_0$ ,  $\omega_n$  as input, and sets a start wind velocity  $V_0$ . It further iterates through increasing values for  $V$ , until the stability limit is found. On each iteration, the complex eigenvalue problem is solved, iteratively, until the in-wind frequencies  $\omega_i$  and damping ratios  $\zeta_i$  are found for every mode shape included in the analysis. If there exists one damping ratio  $\zeta_i$  that equals zero, within a margin, the stability limit has been identified, and the given iterate for the wind velocity  $V_j$  corresponds to the critical velocity  $V_{cr}$ .

**Input:**

- Modal properties:  $\Phi$ ,  $\tilde{\mathbf{M}}_0$ ,  $\omega_n$
- AD-functions

Initiate wind velocity:  $V_j = V_0$

```

while  $V_j < V_{cr}$  do
  for all modes  $\varphi_i$  in  $\Phi$  do
    - Select frequency of mode i:  $\omega_i$ 
    - Assemble the aerodynamic stiffness and damping matrices for the given
      wind velocity and frequency:  $\tilde{\mathbf{K}}_{ae}$ ,  $\tilde{\mathbf{C}}_{ae}$ 
    while  $\omega_i \neq$  in-wind frequency do
      | - Solve quadratic eigenvalue problem
      | - Update frequency  $\omega_i$ 
    end
    - In wind frequency  $\omega_i$  and corresponding eigenvalues are attained
  end
  - All eigenvalues are attained. The real parts are further evaluated.
  if All  $\zeta_i \leq 0$  then
    |  $V_{cr} = V_j + \Delta V$ 
  else if One  $\zeta_i > 0$  then
    |  $V_{j+1} = V_j - 0.5\Delta V$ 
  else if One  $\zeta_i > 0$  then
    |  $V_j = V_{cr}$ 
  end
end

```

When the instability limit is found, the corresponding instability mode shape is extracted from the eigenvalue solution of the identified critical wind speed and frequency. Also, the program plots the real and imaginary parts of the eigenvalues as functions of the wind speed  $V$ . From these plots, it is possible to identify which instability phenomenon that occur. Further, estimated critical wind speed result should be validated by checking that it is within the range of the values of  $V_{red}$  for the AD data points used in the calculation.

## Chapter 3

# Review of Current Long-Span Bridges

The first modern suspension bridges appeared in the early 1800s. Since then, the design of suspension bridges has evolved greatly, with different trends seen at different time periods. This evolution can be seen as a reflection of the analytical theories and engineering practices implemented at the given time. Collapses of suspension bridges due to strong winds have also occurred from time to time, with the most infamous event being the collapse of Tacoma Narrows Bridge in 1940. This accident propelled the study of the effect of aerodynamic forces on suspension bridges, which today is a standard aspect considered in the design process of long-span suspension bridges. In the 1960s, the modern closed box girder made its first appearance. The design of the shape of the closed box girder cannot be said to have converged, however. There is a great variety seen in the shapes used in the world's longest suspension bridges. This chapter will seek to demonstrate this diversity, by presenting drawings of the cross-sectional outer shape of the girders from some of the worlds longest spans. This study is further utilized in the selection of girder shapes to investigate in this thesis. But first, a brief history of suspension bridges is given.

### 3.1 A Brief History of Suspension Bridges

The information in this section is in large part based on the book *Cable Supported Bridges*, by N. J. Gimsing and C. T. Georgakis [19].

The advances in technology and production in the early 1800s allowed for the construction of wrought iron chains, which were implemented in the first major modern suspension bridges. While iron was used for the chains, stone and masonry was used for the towers. A noteworthy example from this early age is the Menai Suspension Bridge (1826) by engineer Thomas Telford, which has a span of 176 meters.



Figure 3.1: Menai Suspension Bridge. Built in 1826. [31]

At this time the calculations heavily relied on the individual brilliancy and intuition of the person in charge of the project, who in most cases functioned as both the engineer and architect. It was in general understood that the stiffness of the girder was important to resist the wind load. This was not rooted in a developed theory, but rather from empirical observations of deformation and collapses of some suspension bridges.

In the second half of the century, further technological advances resulted in the production of steel cables, which left wrought iron chains obsolete. As a result of this improvement, the suspension bridge spans grew rapidly. The bridge girders also began to be built by steel trusses. The Brooklyn bridge from 1883 is an example from of this era. It was the world's longest bridge at the time it was completed, with a span of 486 m, and is actually a hybrid between a suspension and cable stayed bridge.



Figure 3.2: Brooklyn Bridge. Built in 1883. [28]

At the end of the century, structural engineering had evolved into an independent profession, separated from the architect. Engineers began to concentrate more of their efforts on calculations, and less on intuition. Therefore, the complexity of the designs became limited by what was feasible to perform calculations on, with the available tools and knowledge. The theory available at the time was the theory of linear elasticity, which is based on the fundamental assumption of small displacements. This can be seen reflected in the suspension bridges built during this time. They generally have practical designs with very large and stiff truss girders, approaching the assumption of small displacements. An example is the Williamsburg Bridge from 1903. A significant change is seen when comparing it to Brooklyn bridge of 1883. Brooklyn has a very complex and statically undetermined

design, which was no longer sensible to construct in the early 1900s. Despite the large differences between the two bridges, the span of Williamsburg Bridge is only 2 meters longer than the span of Brooklyn. In some respects, the trend to strictly base the design on calculations was a step backwards.



Figure 3.3: Williamsburg Bridge. Built in 1903. [42]

The trend of very stiff bridges lasted for about 20 years, until new advancements in the theory was made. A two-dimensional deflection theory was developed, which had the effect of removing the lower bound for flexural stiffness in the vertical direction of suspension bridge girders. In the 1930s this was extended to a three-dimensional deflection theory, which took into account the horizontal force contribution from the cables as the girder deflects. This removed the lower bound for horizontal flexural stiffness. As a result, a trend of more slender suspension bridges appeared. The 30's became a great decade for long-span suspension bridges, with famous giants such as George Washington, Oakland Bay and Golden Gate bridge. Golden Gate became the world's longest, when it was completed in 1937, with a span of 1280 m. However, the development of increasingly slender suspension bridges would eventually lead to devastation.

The trend of slender suspension bridges accumulated with the collapse of Tacoma Narrows Bridge (TNB) in 1940. The bridge collapsed only four months after its completion, due to a moderate wind speed of 18 m/s. On the day of the collapse, the bridge was observed oscillating vertically, before suddenly changing to a coupled vertical and torsional oscillation. These behaviours were later characterized as galloping and flutter. After approximately one hour of these self-excited oscillations, the hangers began to break in fatigue, and a large portion of the deck fell into the water below. An image of the collapse is shown in figure 3.4.





Figure 3.4: The collapse of Tacoma Narrows Bridge. [12]

TNB was a particularly slender suspension bridge, with a main span of 854 meters and girder height of 2.45 meters. Rather than a traditional stiffening truss, the girder was made as an open plate cross section, which has very little torsional stiffness. The shape of the girder was also particularly bluff, with vertically straight edges on each side. As we know today, the combination of low stiffness and high bluffness is very unfortunate considering aerodynamic stability. Nonetheless, the bridge was dimensioned with adequate safety margins in accordance to the relevant standards at the time. As found from the newly developed deflection theories, little rigidity is required in the bridge girder to withstand the static loads. The shortcoming was that only static loading was considered. The wind loading was included, but only as static pressure.

After the TNB disaster, the importance of the girder stiffness was recognized again. In the following years, old suspension bridges were re-evaluated, and many were altered in order to increase their stiffness. This was the case for George Washington and Golden Gate bridge, where additional truss bracing was added. In new bridges, the stability problem was solved by using conservatively stiff truss girders, leading back to the design trend seen at the start of the century. This change in attitude is clearly seen in the second TNB bridge, built in 1950, shown in figure 3.5 (the closest of the two bridges). However, an innovative solution to the aerodynamic stability problem would soon make the scene.



Figure 3.5: The second Tacoma Narrows Bridge. [39]

The TNB collapse made aerodynamic response of suspension bridges become an important field of research. This problem was treated theoretically and experimentally by several engineers, such as F. Farquharson, F. Bleich, T. Von Karman and A. Selberg. Their findings led to a new procedure for designing suspension bridges, where the aerodynamic stability limit is estimated by with a critical wind speed. Wind tunnel testing was also found to be as a useful tool. This led to the invention of the closed box girder design, which was introduced with Severn bridge in 1966. This girder design was a direct answer to the problems with the TNB girder. A streamlined shape determined through wind tunnel tests was chosen in order to reduce wind forces on the girder, and as a closed box cross section the torsional stiffness was high. Further, the closed box configuration gave notable savings in construction cost, as compared to a truss girder. This was to a large extent due to an efficient fabrication, with the use of automatic welding.

Since then, there has been constructed a diversity of long-span suspension bridges with both truss and closed box girders. The 70s and 80s saw a burst of large suspension bridges in Japan and Europe, and more recent time there has been built some very long spans in Scandinavia and China. While Japan has been heavily influenced in their design by be the American tradition, using deep stiffening trusses and steel towers in many of their bridges, the suspension bridges in Europe generally have streamlined closed box girders and concrete towers.



Figure 3.6: Akashi Kaikyo. The world's longest span. Built in 1998. [15]

As for the record-holder of longest span in the world, the title is today held by Japan's Akashi Kaikyo Bridge, shown in figure 3.6. Completed in 1998, it has a large truss girder and a span length of 1991 m. The worlds longest span with a single closed box girder is the Great Belt Bridge in Denmark, which has a span length of 1624 m.





Figure 3.7: Great Belt Bridge. Built in 1998. [29]

In recent years, further innovation has resulted in the development of twin-box girders. Research has shown that these girders can achieve an even better aerodynamic stability than a single box girder can [18]. An example of a twin-box girder suspension bridge is Xihoumen, which has a span of 1650m.

In Norway, suspension bridges play an integral part of the country's infrastructure. As a land of many rivers, valleys, fjords and islands, one does not simply get far without bridges. As of 2014 there were over 17,200 bridges in the country, where 85 were suspension and cable-stayed bridges [2]. These mostly have moderate spans, but in recent years there has been a trend in the Norwegian construction industry towards mega-projects and long span bridges. Currently, the two longest spans in Norway are of the Hardanger Bridge and the Hålogaland Bridge, with spans of 1310 m and 1145 m respectively. Further, due to the national project of the coastal highway route E39, new long-span bridges are now considered for several fjord crossings along the west coast of the country.



Figure 3.8: Hardanger Bridge. Built in 2013. [22]

## 3.2 Presentation of Box Girder Shapes

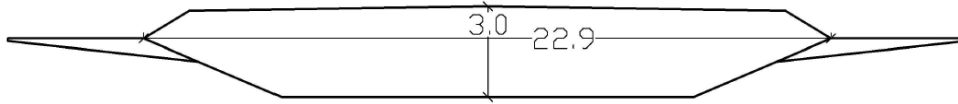
This section seeks to demonstrate the variety seen in the girder design of long-span suspension bridges. Drawings of the outer girder shapes for some of the worlds longest spans is presented. It is the closed box girder suspension bridges that are of particular interest in this thesis, and therefore bridges with truss girders, such as Akashi Kaikyo, are not further considered.

The 15 longest spans in the world (as of June 2020) are presented in table 3.1. Girder drawings for the bridges marked in blue is presented in the following. These are drawn from sources providing various levels of detail, which is considered in the number of decimal places included in the dimensions given. The presentation is ordered chronologically from the years the bridges were built. The information given for these bridges is in large part taken from the book *Cable Supported Bridges*, By N. J. Gimsing and C. T. Georgakis [19].

Table 3.1: The world's longest bridge spans, per June 2020 [44]

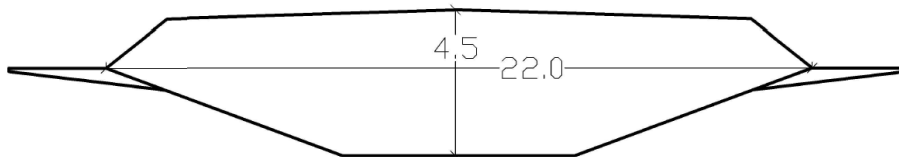
Span Order	Span [m]	Bridge Name	Girder Type	Country	Year Opened
1	1991	Akashi Kaikyo	Truss	Japan	1998
2	1700	Yangsigang	Truss	China	2019
3	1688	Nansha	Box	China	2019
4	1650	Xihoumen	Twin Box	China	2009
5	1624	Great Belt	Box	Denmark	1998
6	1550	Osman Gazi	Box	Turkey	2016
7	1,545	Yu Sun-sin	Twin Box	South Korea	2012
8	1490	Runyang	Box	China	2005
9	1480	Dongtinghu	Box	China	2018
10	1418	Nanjing	Box	China	2012
11	1418	Humber	Box	UK	1981
12	1408	Yavuz Sultan	Box	Turkey	2016
13	1385	Jiangyin	Box	China	1999
14	1377	Tsing Ma	Truss	Hong Kong	1999
15	1310	Hardanger	Box	Norway	2013
(26)	1145	Hålogaland	Box	Norway	2018
(43)	988	Severn	Box	UK	1966

## Severn



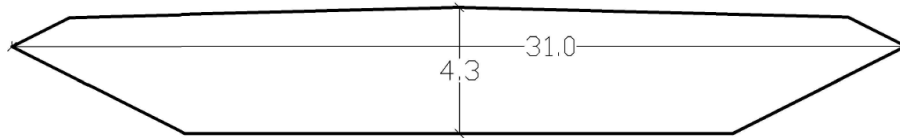
Span:	988 m	Year opened:	1966
Slenderness:	0.0030	Height/Width:	0.13
Other comments:	<p>The world's first closed box girder suspension bridge. Wind tunnel testing was used to decide the shape. Footways are extended on the sides of the girder. Inclined hangers were used to improve the damping characteristics of the bridge.</p>		

## Humber



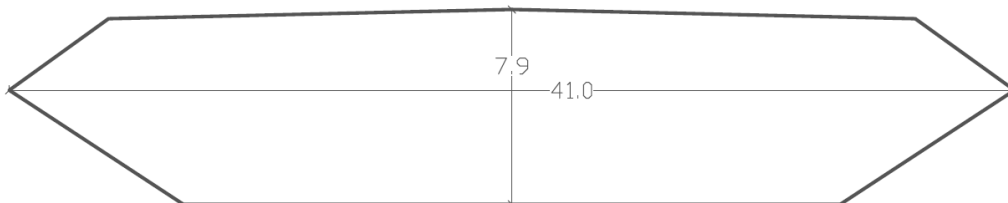
Span:	1410m	Year opened:	1981
Slenderness:	0.0032	Height/Width:	0.20
Other comments:	<p>The height of the girder was increased in order to keep the same slenderness as earlier bridges. However, this may have been unnecessary [19].</p>		

## Great Belt



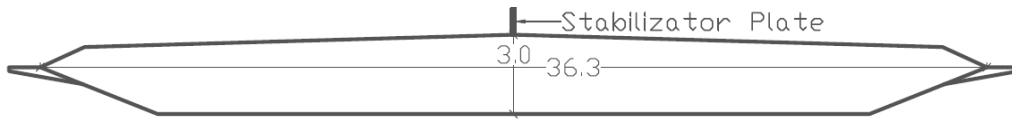
Span:	1624 m	Year opened:	1998
Slenderness:	0.0026	Height/Width:	0.14
Other comments:	The longest span in Europe. The critical wind speed was calculated to be 72 m/s, by wind-tunnel testing [19]. However, vortex-induced vertical oscillations appeared as an issue after construction. Guide-vanes were added as a remedy.		

## Tsing Ma



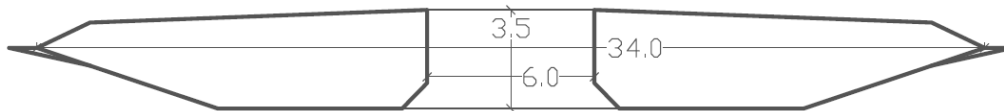
Span:	1377 m	Year opened:	1998
Slenderness:	0.0057	Height/Width:	0.19
Other comments:	The world's longest combined road and rail suspension bridge. The girder is actually a truss, but is covered with steel plates to achieve a streamlined shape. The bridge has the largest cable diameter in the world, of 1.1 m.		

## Runyang



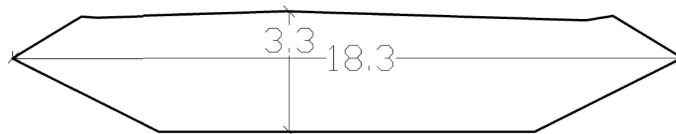
Span:	1490m	Year opened:	2005
Slenderness:	0.0020	Height/Width:	0.08
Other comments:	A stabilizator plate is placed on the top of the deck to alter the aerodynamic properties of the girder.		

## Xihoumen



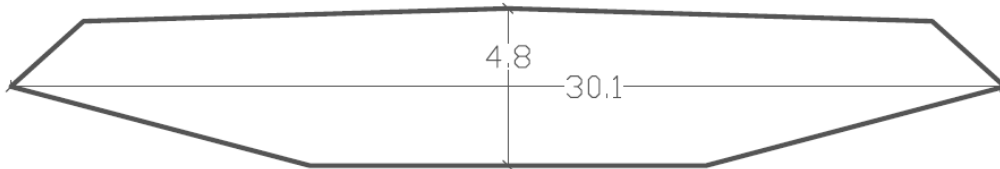
Span:	1650 m	Year opened:	2009
Slenderness:	0.0021	Height/Width:	0.10
Other comments:	It was found that a single-box could not give sufficient critical wind speed of 78.7 m/s [18]. With the twin box girder configuration, the critical wind speed was estimated to be around 88 m/s.		

## Hardanger



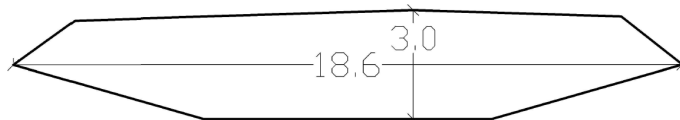
Span:	1310 m	Year opened:	2013
Slenderness:	0.0025	Height/Width:	0.18
Other comments:	The longest span in Norway. Guide vanes have been added to avoid vortex shedding induced oscillations. The girder is not entirely symmetric, due to the inclination criteria from two road lanes and one pedestrian lane.		

## Osman Gazi



Span:	1550 m	Year opened:	2016
Slenderness:	0.0031	Height/Width:	0.159
Other comments:	The girder has a unique shape, with the side edge points positioned quite low, resulting in a sharp angle below the edge points and a more steep angle above.		

## Hålogaland



Span:	1145 m	Year opened:	2018
Slenderness:	0.0026	Height/Width:	0.161
Other comments:	Norway's second longest span. The girder has a similar shape to that of Ozman Gazi, with the edge points positioned quite low. As with Hardanger, the girder is not entirely symmetric, due to carrying two road lanes and one pedestrian lane.		

## Chapter 4

# The Fjord Crossing of Langenuen

This chapter presents the work that has already been conducted on the fjord crossing of Langenuen. This work provided the basis for this thesis.



Figure 4.1: The Langenuen Suspension Bridge as presented by Norconsult in 2015 [6]

### 4.1 Langenuen Suspension Bridge

In 2013, the Norwegian national infrastructure project Coastal Highway Route E39 was initialized. The project is led by the Norwegian Public Roads Administration (NPRA), and has as a long-term goal to construct a continuous highway route between Kristiansand and Trondheim. This means that several fjords must be crossed, either with bridges or tunnels. Hordfast is a major sub-project of Coastal Highway Route E39 and is one of the closest to realization. This project will connect the four cities of Bergen, Leirvik, Haugesund and Stavanger. It includes the crossings of two fjords; Bjørnafjorden in the north and Langenuen in the south, as shown in figure 4.2. The crossing of Langenuen will connect the islands of Stord and Tysnes. Taking into account the width and depth of the fjord, it was found that a single-span suspension bridge would be the appropriate choice for the crossing.

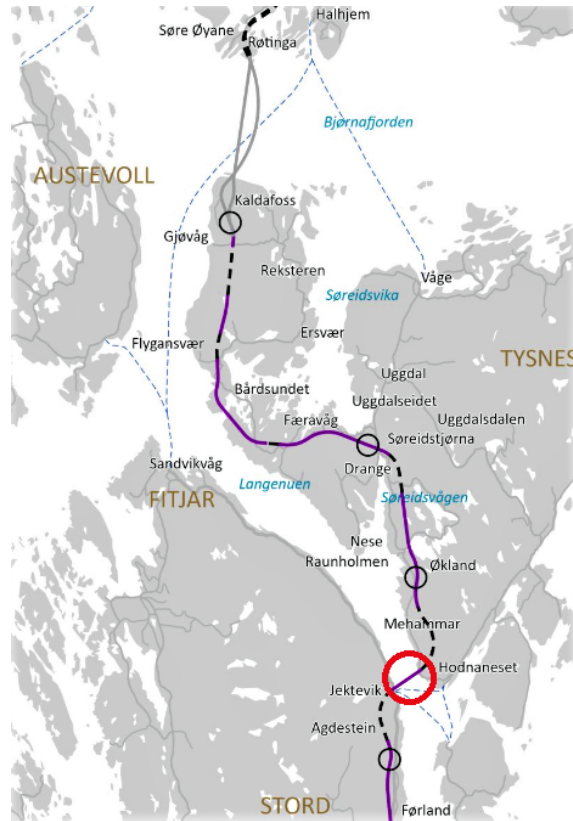


Figure 4.2: Map of the Hordfast project with the Langenuen crossing marked in red [4]

In 2015, a conceptual plan report for the crossing of Langenuen was presented by Norconsult. The report evaluated four different locations for the crossing, with different resulting main span lengths. In September 2019, the decision was made to select the southernmost option [4], where the the span will be 1220 meters [6]. This would rank the bridge as the second longest in Norway today, only 90 meters shorter than Hardanger Bridge. In addition to evaluating the possible fjord crossing locations, Norconsult’s report presented the basis for the global design of the bridge. This included the A-pylons, as seen in figure 4.1, the steel box-girder and the slightly inclined cables and hangers. The bridge was dimensioned to carry four road lanes, two shoulder lanes and one pedestrian lane, as shown in figure 4.3.

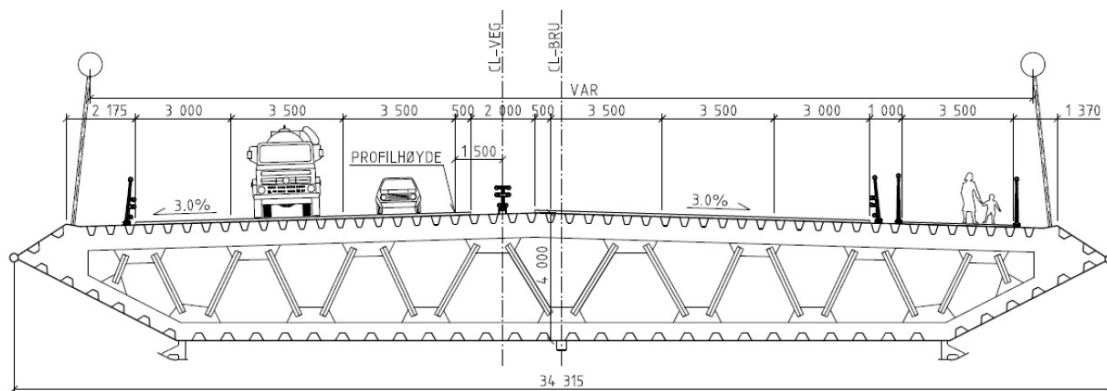


Figure 4.3: The steel box girder as presented by Norconsult in 2015 [6]



## 4.2 Aluminium Girder

The total cost of the Hordfast project has increased significantly since the project was initiated. Therefore, the Norwegian Ministry of Transport has instructed the NPRA to identify potential cost reductions for the project [3]. One of the measures taken is investigating the feasibility and cost of using aluminum as a construction material for the girder in suspension bridges. The fjord crossing of Langenuen was selected as an appropriate case study. A research group was established for the project, consisting of Hydro, Leirvik AS, NPRA, NTNU and Dr.techn. Olav Olsen. By September 2019, a report of their work was presented, discussing the feasibility of using an aluminium girder. This report will henceforth be referred to as "Olav Olsen's report".

### 4.2.1 The Dilemma

Aluminum has about a third of the weight and stiffness of steel, as indicated with in table 4.1. This material difference leads to an interesting discussion, when considering to use aluminium for a suspension bridge girder. As self weight is the dominating gravitational load for long span suspension bridges, an aluminium girder would lead to a considerable reduction of loading on the structure. This may reduce the necessary dimensions of the cable system and pylons. With less material usage, the total cost of the bridge could also be reduced. This was the finding presented in Olav Olsen's report. The aluminium girder in itself would be more expensive than a steel girder, but the increased cost of the girder is outweighed by the cost reductions from the pylons and cable system. Therefore, the aluminium girder is a cost-competitive alternative to the steel girder [27].

Table 4.1: Material properties of aluminum and steel

Material	Density [kg/m <sup>3</sup> ]	E [GPa]
Steel	~ 7800	~ 210
Aluminum	~ 2700	~ 70

However, some challenges also arise due to the material difference. As previously noted, the aerodynamic stability limit of a suspension bridge is dependent upon the modal properties of the bridge, as well as the aerodynamic properties of the girder shape. With aluminium being both less stiff and less dense than steel, this will effect the resulting modal properties of the bridge. Generally, more weight and more stiffness in the girder are both preferable regarding the stability of a suspension bridge. An aluminium girder may therefore seem problematic. However, a solution to this particular problem was also suggested in Olav Olsen's report.

### 4.2.2 Aerodynamic Stability

The design critical wind speed criteria for the fjord crossing is set to 76 m/s. This value comes from the 500-year mean wind velocity, estimated to be 47.4 m/s, multiplied by a safety factor of 1.6 [27].

Dr. techn. Olav Olsen conducted a sensitivity analysis in order to optimize the design of Langenuen suspension bridge, wrt. ultimate stresses, aerodynamic stability and total cost. The analysis was based on varying several parameters, including the height of the girder. The aerodynamic stability calculations were based on the aerodynamic derivatives (ADs) from the girder of Julsundet, seen in figure 4.4, and serve therefore only as approximate

estimations. Nonetheless, the results showed that a sufficient stability could be achieved by selecting a girder with a height of 5.5 m. This corresponds to an increase of 1.5 m from the original steel girder design height of 4 m, seen in figure 4.3. The resulting stability limit was estimated to be equal to the design critical wind speed criteria of 76 m/s [27]. A key factor for this result was identified to be the increased torsional stiffness of the girder, due to the 1.5 m height increase.

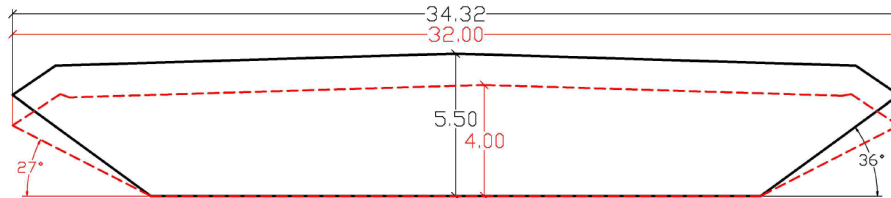


Figure 4.4: Dr.techn. Olav Olsen’s proposed cross section in black line and a Julsundet cross section in red dashed line. The cross sections is scaled to equal width.

The cross section of the girder of Julsundet is shown in a red dashed line in figure 4.4, in comparison to the final proposed design for the girder, in a black solid line. Due to the computational method of using the ADs from Julsundet, the possible girder shapes were limited to those with reasonable similarities to it. The choice was made to strictly scale the height of the girder, not considering other aspects of the shape. Still, the notable shape-wise difference of the two girders indicates the uncertainty in the stability calculations performed. In order to accurately estimate the aerodynamic stability, one must conduct wind tunnel tests for the given girder shape, in order to attain the correct ADs. This was suggested in the Olav Olsen’s report as further work that should be done.

### 4.2.3 Panel Girder Design

Olav Olsen’s report presented a panel girder design concept, which uses so-called ”sandwich panels” in the walls of the girder. This girder design is used as the basis for the girders that are going to be evaluated in this thesis. The cross section of this design is shown in figure 4.5. The panels exploits the advantages of aluminum in production, using methods of extrusion and friction stir welding. In addition, the panels are known for having high strength relative to weight, and are used in some areas of the construction industry, such as in offshore living quarters [27].

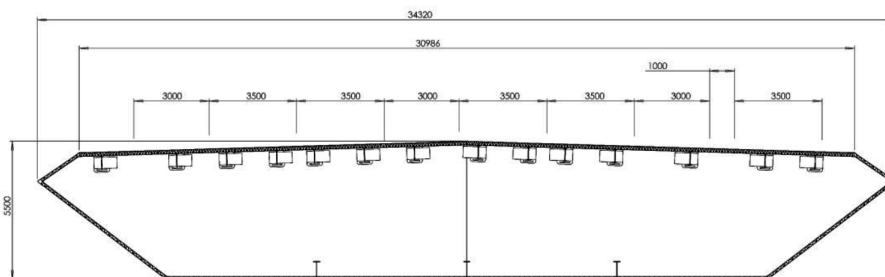


Figure 4.5: Panel girder cross section, as presented in Olav Olsen’s report

The proposed aluminium panels consist of a top and a bottom plate, connected by webs. The web configuration forms a regular pattern in the panels, as shown in figure 4.6. The panel geometry forms a number of ”cells”, which are the triangular open areas enclosed by the the webs and flanges of the panel. There are two different panels used in the girder, namely the deck panels and the other panels. As shown in figure 4.6, the height of the deck panel is 150 mm, while the height of the other panels is 115 mm. Further, the thickness

of the top and bottom plates is 10 mm in all panels, while the webs are 3 mm thick in the deck panel and 4 mm thick in the other panels. These specific dimensions are applied in the calculations performed in chapter 6.

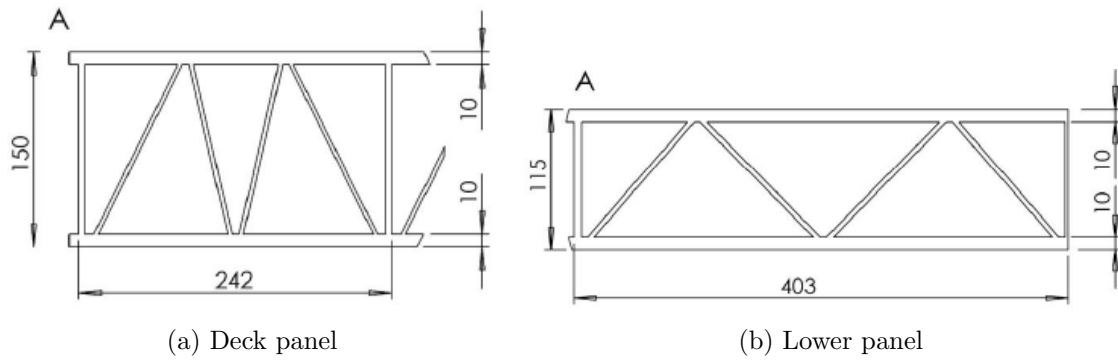


Figure 4.6: Close up of the panel geometry

Longitudinal I-beams are placed below the deck panels in order to provide additional support to carry the traffic loads, while longitudinal T-beams are added to the bottom panel in order to prevent local buckling. There is also included stiffening bulkheads every 12 meters in the girder, as seen in figure 4.7. These bulkheads coincide with the placement of the hanger heads.

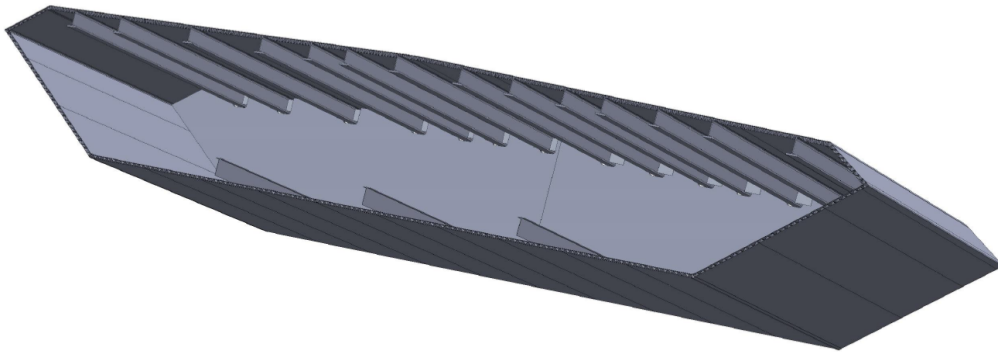


Figure 4.7: Panel girder section in 3D

## Chapter 5

# Parametric Girder Shape

The goal of this thesis is to find a girder shape with sufficient stability for Langenuen suspension bridge. For this purpose, several girder shapes of interest will be wind tunnel tested, in order to estimate their aerodynamic stability limits. The process of selecting these girder shapes is described in this chapter.

### 5.1 Parametrization

In order to investigate the girder shape, a parametric approach was applied. The cross-sectional shape of a box girder is uniquely determined by the coordinates of seven points, as indicated in figure 5.1.

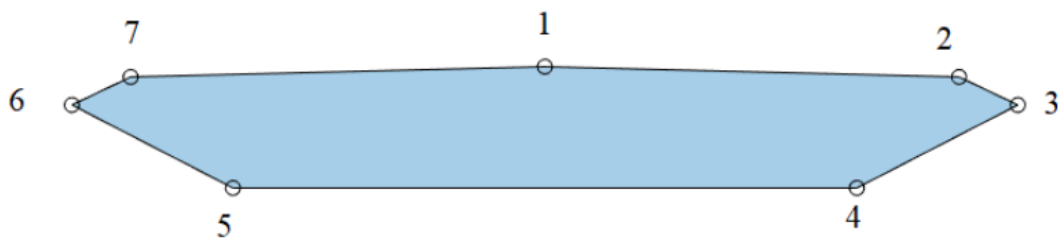


Figure 5.1: The 7 points defining the shape of the box girder cross section

By choosing the top point to be in the center, and keeping the shape symmetric, this is reduced to three points. By further constraining the total width and inclination of the deck of the girder, which is set to 31 meters and 3% for Langenuen [27], there is only two points left to determine. These are the points 3 and 4, marked in red in figure 5.2. In other words, there are now four variables deciding the shape of the girder, i.e. the horizontal and vertical coordinates of point 3 and 4. By implementing a parametrization, where a dependency between these coordinates is specified, the number of unknowns can be reduced further.

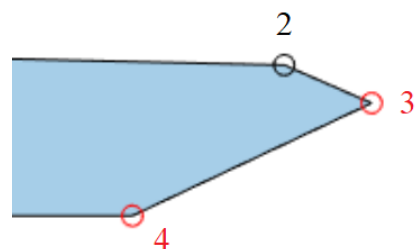


Figure 5.2: The remaining 2 points defining the shape

It was decided to make the girder shape uniquely determined by the total height of the girder,  $H$ , and the angle below the edge of the girder,  $\theta$ . To achieve this, the angle above the edge point was constrained to 30 degrees, and the horizontal distance from the edge of the deck (point 2 and 7) to the edge of the girder (point 3 and 6) was set to  $0.4 \cdot H$ . Thus, the girder shape is determined by the two parameters  $H$  and  $\theta$ .

Both the shape presented by Dr. techn. Olav Olsen, shown in figure 4.5, and the girder shapes of the worlds longest spans, presented in chapter 3, were considered when choosing this parametric model. The parametrization is illustrated in figure 5.3.

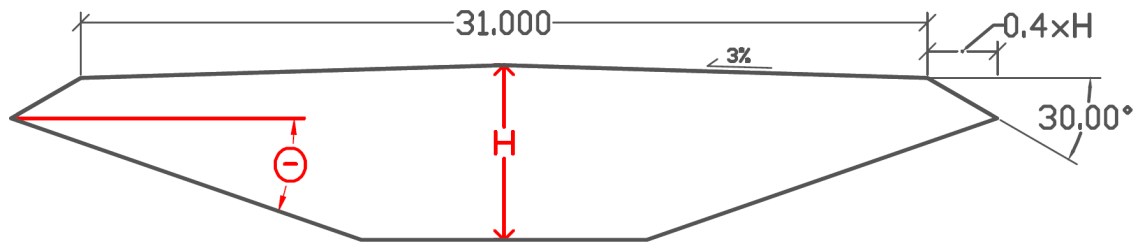


Figure 5.3: Parametric girder

When the height of the parametric girder model is increased, the total width also increases, and the edge points of the girder (point 3 and 6) travel vertically downwards.

The parametrization was implemented in the Dynamo-script *ParamericGirderShape.dyn*, which provides a useful visualization of the girder shape. The script takes  $H$  and  $\theta$  as input values, and by changing their values with a "number slider" the girder shape is automatically updated in the background, as indicated in figure 5.4.

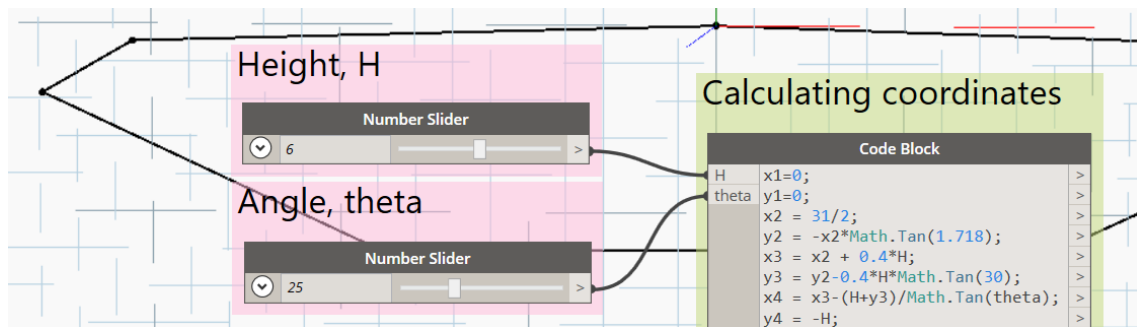


Figure 5.4: Parametric girder Dynamo script

## 5.2 Torsional Stiffness Estimation

With the girder shape defined as a function of  $H$  and  $\theta$ , the critical wind speed  $V_{cr}$  may also be thought of as a function of these two parameters. In order to decide what combinations of  $H$  and  $\theta$  to further select girder shapes from, an additional quantity was considered: the torsional stiffness.

As presented in Chapter 4, Dr. techn. Olav Olsen increased the height of the girder to 5.5 m to achieve a sufficient aerodynamic stability limit estimation. This was mainly attributed to the increase of torsional stiffness. In their preliminary calculations, the St. Venant torsional stiffness constant of the girder was be estimated with Bredt's 2. formula

[27]. The formula is given by [23]:

$$I_T = \frac{4A_m^2}{\oint \frac{ds}{t}} \quad (5.1)$$

Where  $A_m$  is the cross-sectional area measured from the midline of the walls, and  $t$  is the wall thickness. The formula applies for closed thin-wall cross section. It is seen from this formula that the torsional stiffness is strongly dependent upon the enclosed cross-sectional area. Using this formula is a simplification for the panel girder cross section. However, Dr. techn. Olav Olsen applied it with an effective wall thickness of 22.5 mm, and estimated the torsional stiffness constant of their panel girder to be  $31 \text{ m}^4$ .

By using Breddts 2. formula with the same effective wall thickness as Olav Olsen used, a function for the torsional constant  $I_T$  taking the parametric girder shape as input was made. This is implemented in the matlab function *TorsionalStiffnessConstant.m*, which takes  $H$  and  $\theta$  as input values. This function was further used to calculate the torsional constant for a range of  $H$  and theta values, with the matlab script *TorsionalStiffness-Grid.m*. The resulting surface plot of the stiffness constant is shown in fig 5.5.

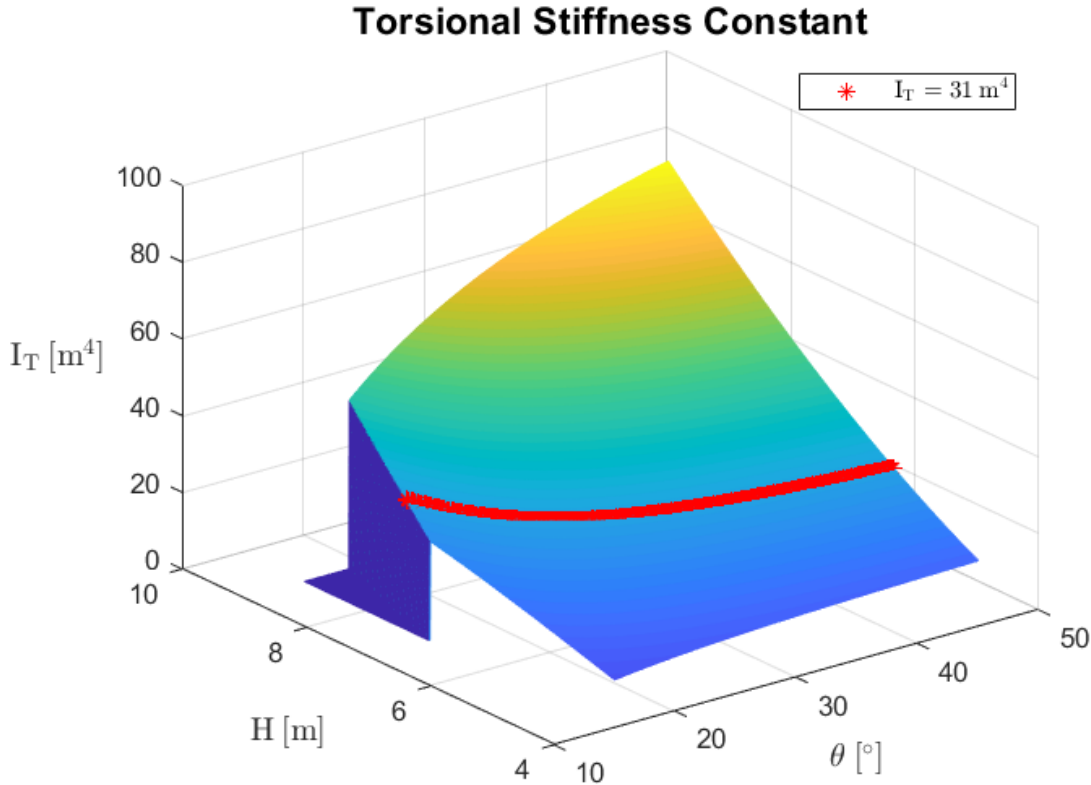


Figure 5.5: Surface plot of the torsional stiffness constant  $I_T$  as a function of  $H$  and  $\theta$ , by Breddts 2. formula. Red stars indicate points at a value of  $I_T = 31 \text{ m}^4$

In this plot, the torsional constant is constrained to zero when the combinations of  $H$  and  $\theta$  result in an invalid geometry, when the two bottom points 4 and 5 cross each other. In order to identify the combinations of  $H$  and  $\theta$  which provide the torsional constant  $I_T = 31 \text{ m}^4$ , the surface plot was "sliced" at this value. The resulting points are marked with red stars in figure 5.5. Further, a data-fitting procedure was implemented in order

to find a function for the curve in the  $H$ - $\theta$ -plane from these points. The resulting rational function is given in figure 5.6, with  $\theta$  expressed as a function of  $H$ .

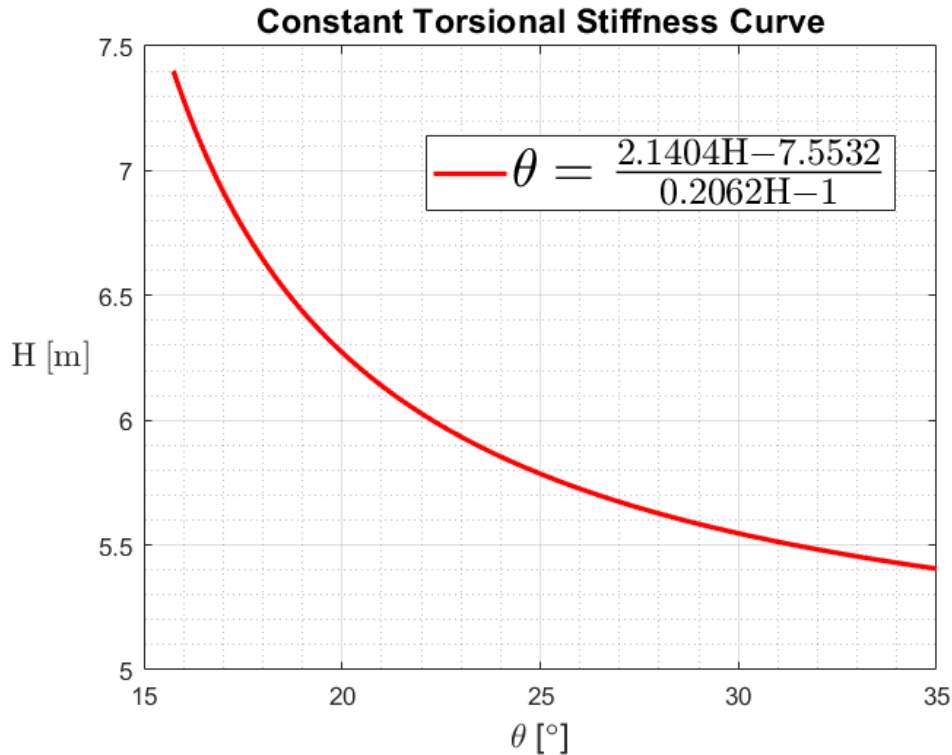


Figure 5.6: Constant torsional stiffness curve,  $I_T = 31 \text{ m}^4$

It is seen from this identified curve that the height of the girder shapes increase as the angle is reduced, when the torsional stiffness is constant. Roughly speaking, the girder shapes in the area below the curve are more streamlined, but less stiff, while the shapes above the curve are stiffer, but more bluff. As for the girder shapes on the curve, they all have the same torsional stiffness, while their relative aerodynamic performance is hard to compare. By only considering the girder shapes on this curve, the shapes become uniquely determined by one single parameter; either  $H$  or  $\theta$ . In the following,  $H$  will be referenced as the standard input.

The entire computational procedure that has been described in this section is executed by the matlab script *TorsionalStiffnessGrid.m*, which uses the function *TorsionalStiffnessConstant.m*. The Dynamo-script *ConstantTorsionalStiffness.dyn* provides a visualization of the girder shapes on the constant torsional stiffness curve, with only  $H$  as input. The start of the script is shown in figure 5.7.

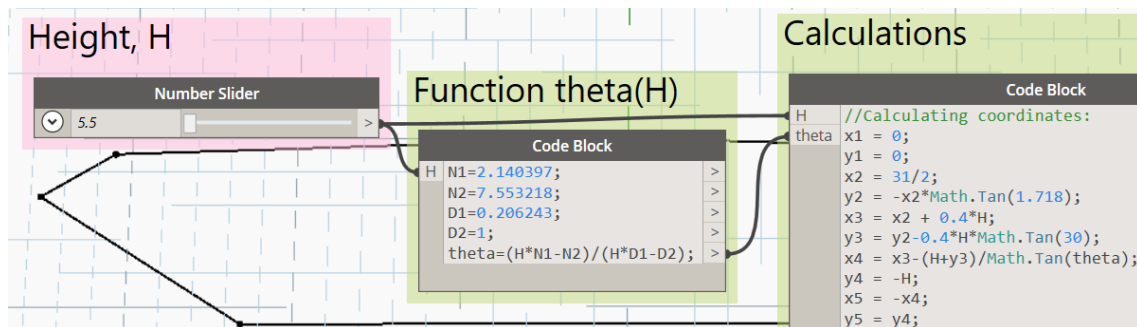


Figure 5.7: Dynamo script implementing the function  $\theta(H)$

### 5.3 Selecting Girder Shapes

It was decided to select a total number six girder shapes. These were extracted from the curve of constant torsional stiffness, in a range between height of 5.5 and 7 meters, with a step length of 0.3 meters. These selected girder shapes are visualized in figure 5.8.

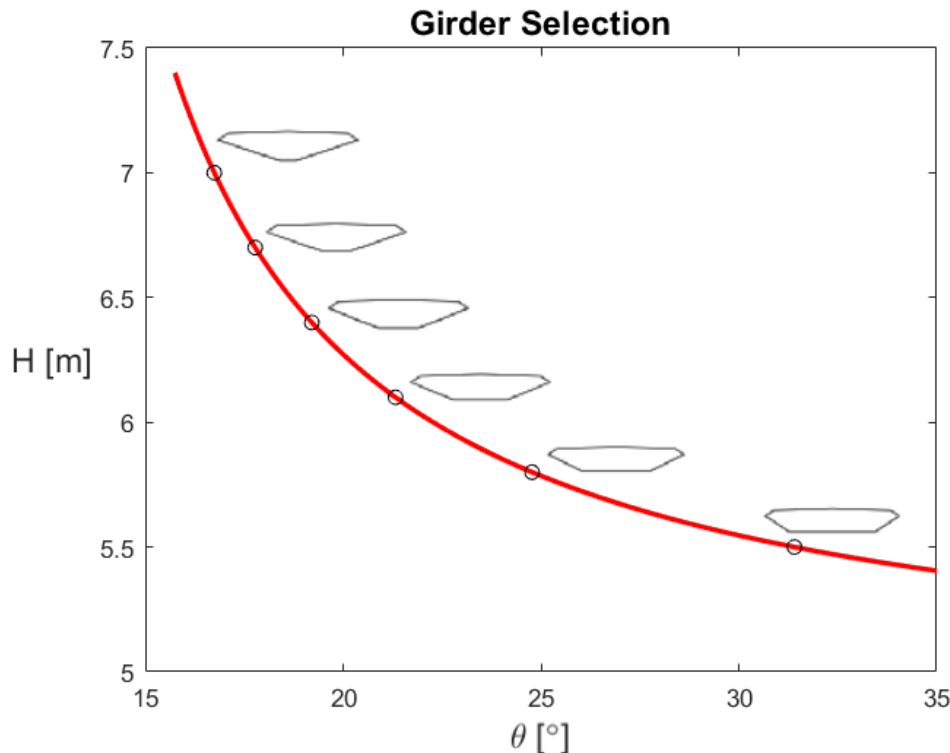


Figure 5.8: Six selected girder shapes

While the height of the selected girder shapes varies between 5.5 and 7 meters, the angle varies between 17 and 31 degrees. When the height is increased, the angle decreases. It can be seen that the girder shape with height 5.5 m is quite similar to the panel girder design presented in Olav Olsen's report, and it also draws some resemblance to the girder shape of Great Belt Bridge. As for some of the higher girder shapes, a resemblance can for instance be drawn to the girder shape of Humber Bridge. A similar height-to-width ratio is also found in the girders of Hardanger and Tsing Ma. These can all be seen in chapter 3. In general, the selected girder shapes are quite high in comparison to most of girder shapes of the long-span bridges in the world today. This may be concerning when remembering that the drag force is proportional to the height. However, the wind flow around a girder is a complex, and only wind tunnel testing can reveal the full picture. It should be acknowledged that an unconventional girder shape may be necessary when using aluminium as material instead of steel.

An advantage of selecting girder shapes on the basis of constant torsional stiffness is that the resulting cross-sectional area and perimeter also remain roughly unchanged. This implies further that the amount of material usage also should be about the same, and therefore so should the cost of the girders. This is recognized as an important factor for the relevancy of the selected shapes. In addition, equal material usage would also mean equal mass, which is a main factor for the modal properties of the bridge. Having said that, the mass and stiffness of the girders will be estimated in detail in the next chapter.









The six selected girder shapes, along with specific geometric properties, are presented in table 5.1. These properties are calculated using the Dynamo-script *GeometricProperties.dyn*. The area and perimeter are measured around the outer edge of the shape, and are therefore not to be confused with the values applied in Bredts 2. formula. The area should also not be confused with the solid material area of the girder cross section. Drawings with detailed dimensions for the six girder shapes are given in the appendix A.

#### **A note on inaccuracies:**

There was a minor error in the algorithm used to execute the slicing of the plot in figure 5.5. This lead to the points being extracted at a mean value of  $30.8 \text{ m}^4$  rather than  $31 \text{ m}^4$ , and to the variation of the stiffness being about 0.6%. In any case, this inaccuracy is deemed as insignificant, as the selected girder shapes still approximately have the same torsional stiffness as intended. This error has been corrected in the script *TorsionalStiffnessGrid.m* given as an electronic attachment, and it will therefore not produce the exact same rational function for the curve as shown in figure 5.6.

There was also made a slight error in the application of Bredts 2. formula. The line used as reference for the area and the circumference was the line of a distance of  $t_{\text{ef}}/2 = 22.5\text{mm}/2 = 11.25\text{mm}$  inside the girders, rather than the midline of the panels in the girders. This lead to 4.5% higher estimates than would be attained using the midlines. Of course, the estimates also depend upon the effective thickness used. A full evaluation of the use of Bredts 2. formula is conducted at the end of the next chapter, and the exact stiffnesses are also estimated.

Table 5.1: Selected girder shapes

H [m]	$\theta$ [°]	Girder Shape	Geometric Properties
5.5	31.4		<ul style="list-style-type: none"> <li>• Width = 35.4 m</li> <li>• H/Width = 0.16</li> <li>• H/Span = 0.0045</li> <li>• Area = 159.4 m<sup>2</sup></li> <li>• Perimeter = 73.6 m</li> </ul>
5.8	24.8		<ul style="list-style-type: none"> <li>• Width = 35.64 m</li> <li>• H/Width = 0.16</li> <li>• H/Span = 0.0048</li> <li>• Area = 159.7 m<sup>2</sup></li> <li>• Perimeter = 73.8 m</li> </ul>
6.1	21.3		<ul style="list-style-type: none"> <li>• Width = 35.88 m</li> <li>• H/Width = 0.17</li> <li>• H/Span = 0.005</li> <li>• Area = 160.2 m<sup>2</sup></li> <li>• Perimeter = 74.1 m</li> </ul>
6.4	19.2		<ul style="list-style-type: none"> <li>• Width = 36.12 m</li> <li>• H/Width = 0.18</li> <li>• H/Span = 0.0052</li> <li>• Area = 160.8 m<sup>2</sup></li> <li>• Perimeter = 74.6 m</li> </ul>
6.7	17.8		<ul style="list-style-type: none"> <li>• Width = 36.36 m</li> <li>• H/Width = 0.18</li> <li>• H/Span = 0.0055</li> <li>• Area = 161.2 m<sup>2</sup></li> <li>• Perimeter = 75.0 m</li> </ul>
7.0	16.7		<ul style="list-style-type: none"> <li>• Width = 36.6 m</li> <li>• H/Width = 0.19</li> <li>• H/Span = 0.0057</li> <li>• Area = 161.5 m<sup>2</sup></li> <li>• Perimeter = 75.5 m</li> </ul>

# Chapter 6

## Cross Sectional Parameters

The cross-sectional parameters of the six girders must be determined. This includes the axial, bending and torsional stiffness. The parameters determining these stiffnesses are the cross sectional area -  $A$ , the 2nd moments of area about the principal axes -  $I_y$  and  $I_z$ , and the St Venant torsional stiffness constant -  $I_T$ . The computation of these parameters will be presented in this chapter. Special emphasis will be put on the computation of the torsional stiffness constant, as this is the most complex exercise. Two main methods of analysis are performed, namely a finite element method (FEM) approach, using a beam cross section module in Abaqus, and a thin-wall theory based approach, using CrossX. The thin wall analyses are performed both on models with exact panel geometry, and on models with simplified geometry. The results of the analyses are compared in order to decide the cross-sectional parameter values to be used in further aerodynamic stability analysis. The estimates found for the torsional constant are also used to evaluate the use of Bredt's 2. formula.

### 6.1 St. Venant Torsion

The torsional moment  $M_x$  can generally be divided into a St. Venant and warping contribution,  $M_x = M_{x,St.V.} + M_{x,Warp.}$ . However, warping is primarily relevant for open thin-walled cross sections [9]. It is therefore assumed negligible for the girders in this thesis, and only St. Venant torsion will be considered. The St. Venant torsion theory is based on the assumptions [23]:

- The material follows Hooke's law
- The deformations (rotations) are small
- The cross sectional shape remains unchanged along the length axis
- Warping deformations are not restricted

These assumptions are considered reasonable for the girders in this thesis.

St. Venant torsion theory applies the following equations for the displacements of the cross section [9]:

$$u = \theta\psi(y, z) \tag{6.1a}$$

$$v = -\theta xz \tag{6.1b}$$

$$w = \theta xy \tag{6.1c}$$

Where  $u$ ,  $v$  and  $w$  are the axial, horizontal and vertical displacements, respectively.  $\psi(y, z)$  is called the "warping function", and  $\theta$  is the "rate of twist". At the longitudinal coordinate  $x$ , the twist angle of the cross-section is given by  $\phi = \theta x$ . Further, the rate of twist  $\theta$  is determined by the outer torsional moment and the torsional stiffness of the cross-section [9]:

$$\theta = \frac{M_x}{GI_T} \quad (6.2)$$

There is no generally applicable analytical formula for the St. Venant torsional stiffness constant,  $I_T$ , of arbitrary cross sections. It comes down to how the shear stresses distribute over the cross sectional area, when loaded under torsion. Only numerical methods can solve the St. Venant torsion problem for arbitrary cross sections. However, for the special case of thin-walled cross sections, there are available formulas, such as Bredt's 2. formula. In the following, calculations are presented from both FEM and thin-wall theory based analysis.

## 6.2 Finite Element Analysis

For arbitrary cross sections the St Venant torsional constant can only be estimated with numerical methods. One practice is to use a FEM formulation with the warping function as the field variable. The degrees of freedom are the point values of the axial displacement  $u$ , or the warping function  $\psi$ , when the rate of twist is set to unity [8]:

$$\psi = u = \mathbf{N}\mathbf{v} \quad (6.3)$$

Here,  $\mathbf{N}$  is the interpolation functions, and  $\mathbf{v}$  is the DOF vector. The values of the DOFs are identified by solving the system equation  $\mathbf{K}\mathbf{r} = \mathbf{R}$ . Further, the shear stresses,  $\tau_{xy}$  and  $\tau_{xz}$ , of the individual elements are identified, and the total torsional stiffness is estimated by taking the sum of the contributions from each element. For a uniform cross-section, the torsional constant can be expressed by the formula [8]:

$$I_T = \sum_{\text{nels}} \delta I_T = \sum_{\text{nels}} \left( \int_{A_e} [\mathbf{y}^T \ \mathbf{z}^T] \begin{bmatrix} \mathbf{0} & \mathbf{N}_1^T \\ -\mathbf{N}_1^T & \mathbf{0} \end{bmatrix} \left( \mathbf{B}\mathbf{v} + \begin{bmatrix} \mathbf{0} & -\mathbf{N}_1 \\ \mathbf{N}_1 & \mathbf{0} \end{bmatrix} \begin{bmatrix} \mathbf{y} \\ \mathbf{z} \end{bmatrix} \right) dA \right) \quad (6.4)$$

where  $\mathbf{y}$  and  $\mathbf{z}$  are the corner node coordinates, and  $\mathbf{N}_1$  are the interpolation functions.

As for the practical procedure applied, the Abaqus beam section analysis procedure described on the website [37] was followed. To model the cross sections geometry of the girders, the CAD-software AutoCAD was used. It enables an efficient multiplication of repeating patterns, which was useful for the panel geometry. The local panel dimensions used are based on the panel drawings presented in Dr. techn. Olav Olsen's report, seen in chapter 4.2.3. The resulting CAD-files were imported into the Abaqus CAE as "2D-sketches". A sketch of the 7.0 m girder is shown in figure 6.1

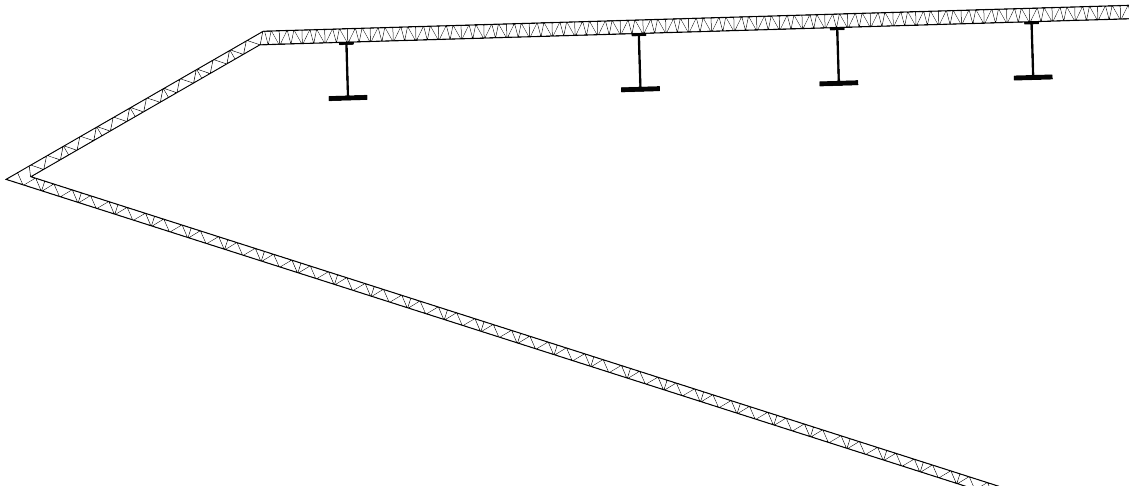


Figure 6.1: Part of the imported CAD-geometry

Using Abaqus CAE, the sketches were meshed with mainly quadrilateral, and some triangular, 2D warping elements. These have 4 and 3 nodes, respectively, and have one DOF per node, which corresponds to the value of the warping function.

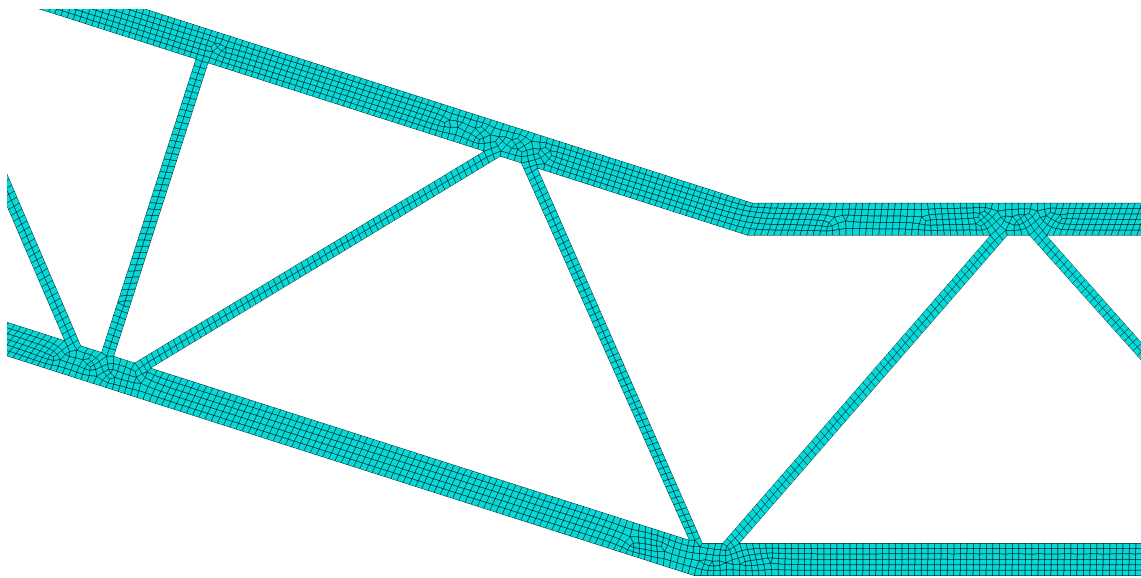


Figure 6.2: FE Mesh of the 7.0 m girder

The meshed models were further sent to analysis by submitting "jobs" from within Abaqus CAE. The analyses generate a number of result files. Among these, the .DAT-files were inspected in order to uncover possible errors, while the .BSP-files were used to extract the results in terms of the cross-sectional parameters. The analysis also provided rotational inertia forces, which are presented in the next chapter.

A simple sensitivity analysis of the mesh size was performed to ensure convergence of results. This revealed that the analysis was not very sensitive to the mesh grid size.

### 6.3 Thin-Wall Analysis

For closed thin-walled cross-sections, the shear stresses are assumed to be constant over the wall-thickness, and propagate as a one-directional cyclic flow [23]. Bredt's 2. formula, given in equation 5.1 in the previous chapter, can be applied to such cross-sections to calculate the torsional constant. However, this is an approximation for the girders in this thesis, as their panel walls are not of solid thickness, but consists of many "cells", which are formed between the webs and the top and bottom plates in each panel. The girders are therefore multi-celled cross-sections. Each cell will have its own cyclic shear flow, and therefore the shear flow in the webs separating the cells will be bi-directional. Each cell will "take up" a part of the outer torsional moment, and the sum over all cells will be equal to the total torsional moment load. For such a cross section, the torsional constant can be estimated by solving a linear system of equations for the shear flow in each cell. This is the method used by the thin-wall module in the software CrossX, which was developed locally at NTNU by Professor Kolbein Bell. A thin-wall model is created by a number of straight lines, or "segments", connected at nodes. The following formulas are taken from the User's manual of CrossX [10]. The program identifies all cells in the model, and solves the system of linear equations:

$$\mathbf{B}\mathbf{p} = \mathbf{a} \quad (6.5)$$

where  $\mathbf{B}$  is a coefficient matrix,  $\mathbf{a}$  is a vector containing the respective enclosed cell areas, measured from the midline of its walls.  $\mathbf{p}$  is the vector of unknown shear flows around each cell. Therefore, the number of unknowns is the number of cells in the cross-section, which is more than a thousand for the girders in this thesis. The diagonal elements in the coefficient matrix  $\mathbf{B}$  are:

$$B_{rr} = \sum_{k=1}^{n_{rr}} \frac{\Delta l_k}{G_k t_k}, \quad (6.6)$$

where the sum is taken over all line segments of the cell, with  $k$  denoting the segment number for cell number  $r$ .  $\Delta l_k$ ,  $G_k$  and  $t_k$  are the length, shear modulus and thickness of the respective segment. The off-diagonal elements are given by:

$$B_{rs} = B_{sr} = \sum_{k=1}^{n_{rs}} \frac{\Delta l_k}{G_k t_k}, \quad (6.7)$$

where the sum is taken over the line segments which are common to both cells  $r$  and  $s$ . If cell  $r$  and  $s$  have no common segments, the term is equal to 0.

When the system of linear equations is solved for  $\mathbf{p}$ , the total torsional stiffness of the section is found by the formula:

$$GI_T = 4\mathbf{p}^T \mathbf{a} + \frac{1}{3} \sum_{k=1}^{n_f} G_k t_k^3 \Delta l_k \quad (6.8)$$

where the first term accounts for the cells of the cross-section, and the second term accounts for the open parts.

For the girders modelled with exact geometry, every web in every panel was included as an individual segment. This results in over thousand cells and more than two thousand segments. In order to produce such a detailed sketches for the six girders, a paramet-

ric Dynamo-script developed. The Dynamo software was chosen over other programming software because of its ability to visualize the computations being conducted. The script is called *CrossX\_ExactGirderSketch.dyn* and is given as an attachment. The output is a .TXT-file that can be imported into CrossX to produce the model. Each line in this file contains 5 data values defining one segment, namely: the coordinates of its start and end point, and the thickness of the segment.

The script starts out with only one input parameter, the girder height H, equal to that shown in figure 5.7. From here, the midlines of the top and bottom plates of the panels are identified through translation, indicated in figure 6.3.

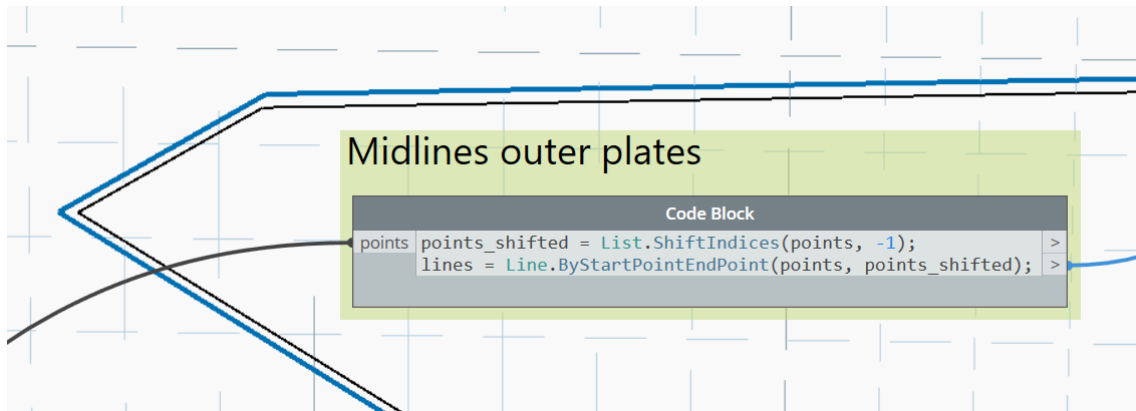


Figure 6.3: Midlines of outer and inner panel plates. Outer midlines are marked in blue.

These lines are further used as guide lines to extract the points for every node in the panels. The panel geometry follows a regular pattern, which is taken advantage of to find the points for the nodes. The points are identified by translating the corner points of the midlines the given regular distances in the direction of the midlines. The resulting points are shown in figure 6.4.

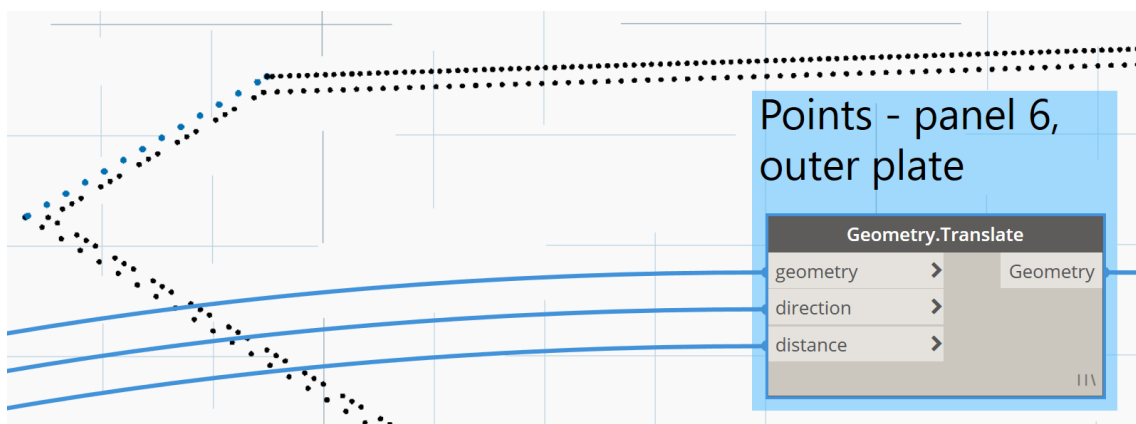


Figure 6.4: Node points. Outer points line 6 are marked in blue.

After having identified all node points, the combinations of these points constructing every line segment of the cross section had to be determined. The regular patterns of the web configurations are identified and used in order to extract lists of points providing the combinations constructing the web segments. This was achieved using Python scripts inside the Dynamo script. In these scripts, looping structures was used. The loops iterate

through the node points of the outer and inner plate midlines, and use the modulo operator on the loop iteration counter to construct new lists of points defined by the regular pattern. An example for the outer connection points of line 6 is shown in figure 6.5.

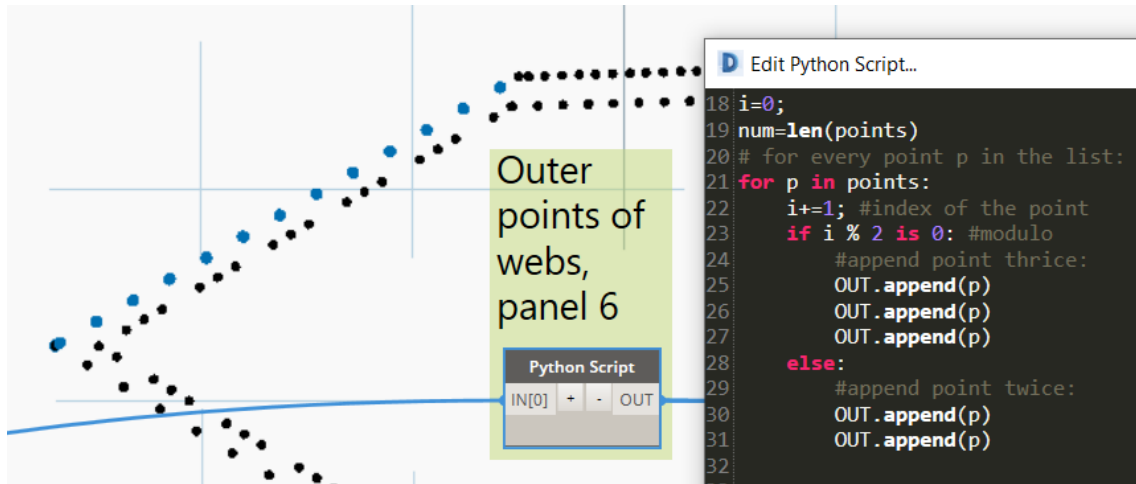


Figure 6.5: Python script

After having identified the combinations of start and end points of the webs, their segments can readily be drawn. This is shown in figure 6.6. As for the segments of the top and bottom plates, the combinations of start- and endpoints are simply found by shifting the indices of the end points in relation to the start points by one index.

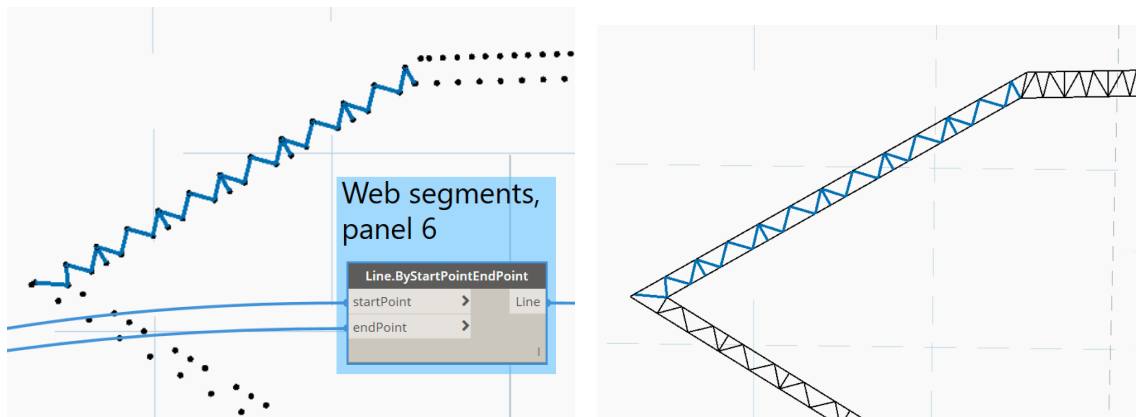


Figure 6.6: Web segments

When the start and end point combinations for every segment in the entire girder is identified, a string is written with their coordinates and segment-thicknesses. This string is written on the format which is readable to CrossX. It is further saved as .TXT-file at the end of the script, as shown in figure 6.7.



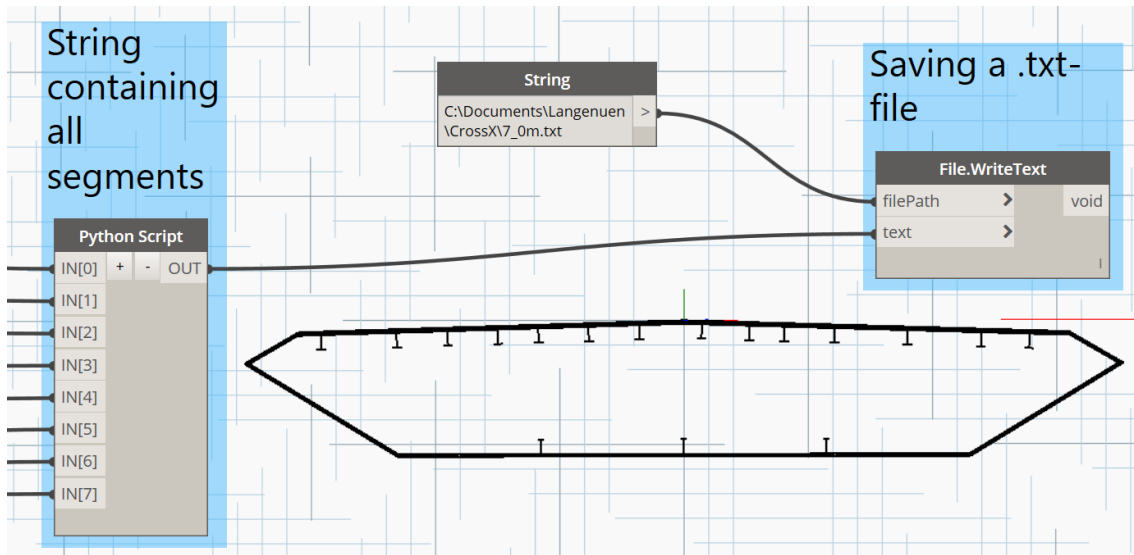


Figure 6.7: The Dynamo script saves the .txt-file of the sketch

Since the Dynamo script takes only the girder height  $H$  as input, it can create a sketch for any girder shape along the curve shown in figure 5.6. It was used to create .TXT-files all six selected girder shapes, and these were further imported into CrossX. The resulting sketches contain over two thousand segments and over one thousand nodes and cells, respectively. After the six sketches had been uploaded, they were visually inspected in order to detect errors, before the calculations were performed. A close up of the deck panel of a sketch as seen from inside CrossX is shown in figure 6.8.

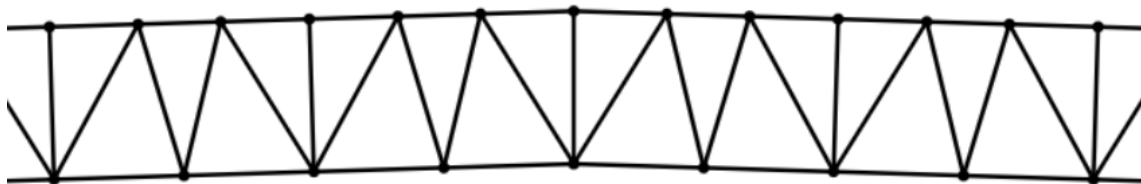


Figure 6.8: Close up of the deck panel as seen in CrossX.

When the segments are joined at the nodes in CrossX, their respective surfaces overlap each other. This is shown in figure 6.9, with a close-up of a node of the deck panel. This overlap leads to some extra material area at the joint, which accumulates for every node in the sketch. This leads to a certain amount of excessive material area as compared to the original geometry. This effect is pointed out by the author of the CrossX, Kolbein Bell, in his book *Fas-thetslære* [9]. This area exaggeration becomes apparent when it is compared to the area of the Abaqus model in the next section. It is worth mentioning that the panel geometry applied in this thesis does not include rounding at the joints. If this in reality should be included, it

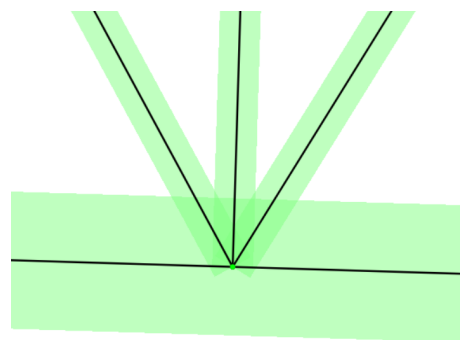


Figure 6.9: Close up of a node in a the exact CrossX model

can be argued that the "excessive" material in the CrossX model is closer to the reality.

In addition to the exact modelling method just described, a simplified modelling method was also implemented. The motivation for this was mainly to investigate if such a method can provide sufficient quality of results. In this method the panels of the girders were modelled as solid thickness walls. These walls were positioned on the midlines of the panels, and their thicknesses were determined in order to result in the same total material area as the exact models result in. The simplified method will be evaluated by comparing the results from it to those of the exact method. Through this comparison it will be apparent how accurately the girder must be modelled to get good results. The comparison will also give an indication of the validity of using Bredts 2. formula for the torsional stiffness constant, as it is based on a cross section with a solid wall thickness. A simplified model of the 5.5 m girder is presented in figure 6.10:

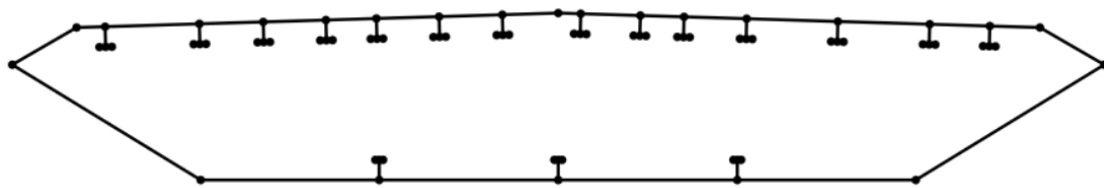


Figure 6.10: Simplified model of the girder of height 5.5 m

## 6.4 Results

The results from the analyses with Abaqus and CrossX are presented in this section. To summarize, three methods of analysis has been performed for each of the six selected girders, one with FEM in Abaqus, and two with thin wall theory in CrossX.

In order to compare the results between the different analysis methods for the different girder shapes, the resulting values are plotted as data points, and a 2nd order polynomial fit between these points is plotted for each analysis method. This polynomial fit clearly indicates the development of the given cross sectional parameter as the girder shape changes. This visualization technique is used in large parts of the thesis, in order to compare results between the six girders. The legends of the plots may refer to the data fitted 2nd order polynomials, and not the data points of each analysis method. However, these curves should generally not be regarded as continuous functions, rather only tools to visualize the differences between identified data points.

### 6.4.1 Solid Cross Sectional Area

The area presented in this section, should not be confused with the total enclosed area of the outer girder shapes presented in Chapter 5. The area in this section is the solid material area of the girder cross-sections. The axial stiffness of the girders is proportional to this area, and it is also an important factor for the cost of the girder.

As mentioned in the previous section, the CrossX model slightly exaggerates the solid cross sectional area. The relative increase in area from the Abaqus model to the CrossX models is about 1.6 %, and is clearly visible in the gap between the curves shown in figure 6.11. The stiffness parameter results from the Abaqus and CrossX analyses should be seen in the light of this difference in material area.

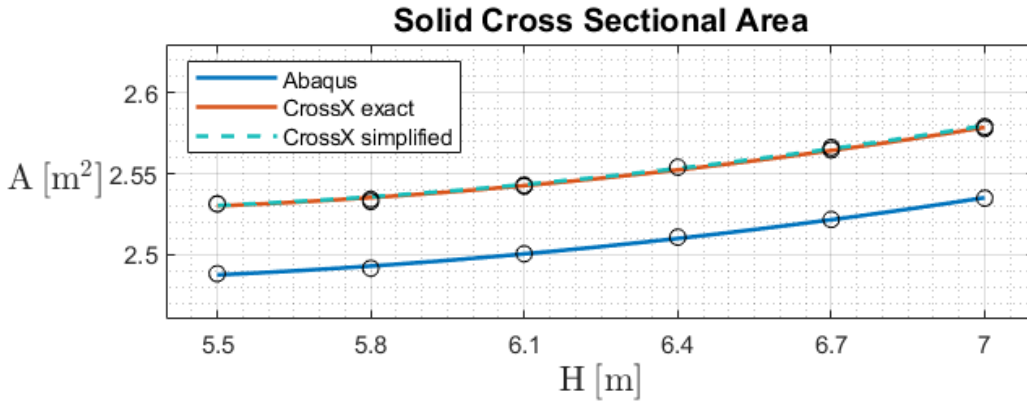


Figure 6.11: Solid material cross sectional area

It is also seen in the figure that the area increases slightly with the height of the girder. The total relative increase from the girder of height 5.5 m to the girder of height 7.0 m is of about 1.9 %. Further, the correlation coefficients between the three methods are equal to 1.0 down to eight decimal places for all combinations, indicating a near perfect correlation. This means that the area development of the three methods is proportional, separated by a scale-factor only. Naturally, the areas of the two CrossX modeling approaches are the practically the same, as this was the intention when selecting the wall thicknesses of the simplified model.

### 6.4.2 2nd Moment of Area

The flexural stiffness of the girders in the vertical and lateral direction is proportional to the 2nd moment of area about the horizontal and vertical axes,  $I_y$  and  $I_z$ . These parameters have been calculated with the three methods described, and are plotted and

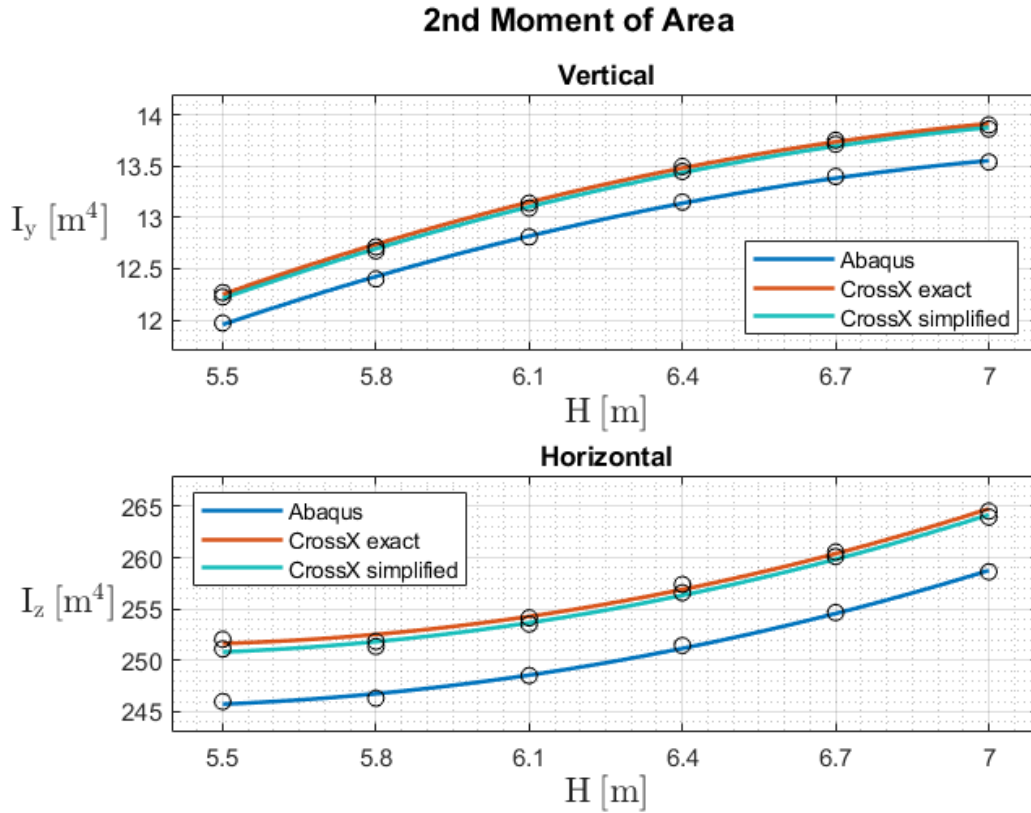


Figure 6.12: Vertical and horizontal 2nd moment of area

The effect of the difference in material area between the Abaqus model and the CrossX models is clearly seen in the resulting stiffnesses. The increase in stiffness from Abaqus to CrossX exact is about 2 %, both vertically and horizontally. There is also a slight difference between the stiffnesses obtained from the exact and simplified models in CrossX, with the exact models having the highest estimates. This is due to the effect of the Steiner contribution, giving higher stiffness for material is spread out across space than being centered. As is the case for the panel geometry of the exact model, while for the simplified model centers the material on the midline. However, the difference is minimal, only about 0.3 %. The relative increase in vertical stiffness between the 5.5 m girder and the 7.0 m girder is about 13%, while the increase of horizontal stiffness is about 5 %.

### 6.4.3 Torsional Stiffness Constant

The estimates of the torsional constant from the three analysis methods can be seen in figure 6.13.

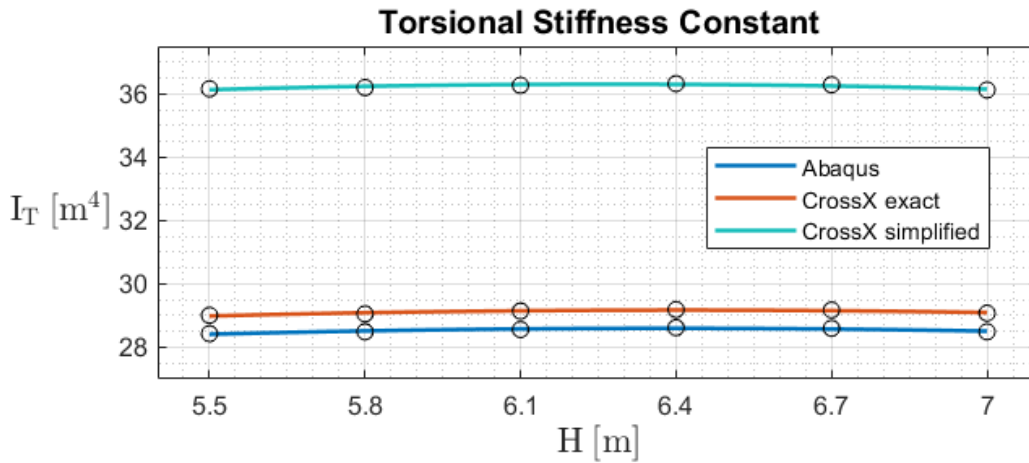


Figure 6.13: Torsional stiffness constant of three different calculation procedures

As expected, the torsional stiffness among the six girders remain roughly constant for all analysis methods. The relative variation is only about 0.6 % for the three methods, identical to the difference found when extracting the girders with Bredts 2. formula.

It is only estimates from Abaqus and the exact model in CrossX that can be considered to be accurate. This is because only they account for the actual geometry of the panels. The two methods estimate a torsional stiffness constant of about 28.5 m<sup>4</sup> and 29.1 m<sup>4</sup>, respectively. This is a difference of about 2 %. The difference is assumed to be directly correlated to the difference in material area.

The simplified model with constant wall thickness largely overestimates the torsional constant, giving a value of about 36 m<sup>4</sup>. This overestimate was expected, as it was already decided in chapter 5 to estimate the torsional constant using Bredts 2. formula with an effective thickness of  $t_{ef} = 22.5\text{mm}$ , which is smaller than the thickness used in the simplified model.

As explained in chapter 5, the midline used in the torsional stiffness calculations was not placed far enough inside the cross-section, therefore yielding in slightly too large torsional constant estimates. These estimates are plotted and indicated with the solid red curve in figure 6.14.

Estimates with the midline placed correctly, and with the same  $t_{ef}$ , result in a value of about 29.6 m<sup>4</sup>. These estimates are indicated with the middle curve in figure 6.14. Comparing these values with the estimates Abaqus and CrossX it is seen that the estimates of Bredt's 2. formula are higher, and that  $t_{ef}$  of 22.5mm therefore must be slightly too large. By trial, it was found that using Bredts 2. formula with the correct midline and an  $t_{ef}$  equal to 21.75mm and 22.2mm result in the same estimates as provided by Abaqus and the CrossX (exact geometry), respectively. The estimates of Bredt's formula with  $t_{ef} = 22.5\text{mm}$  are indicated with a dashed line in figure 6.14. These values correspond to those of the Abaqus analysis shown in figure 6.13.

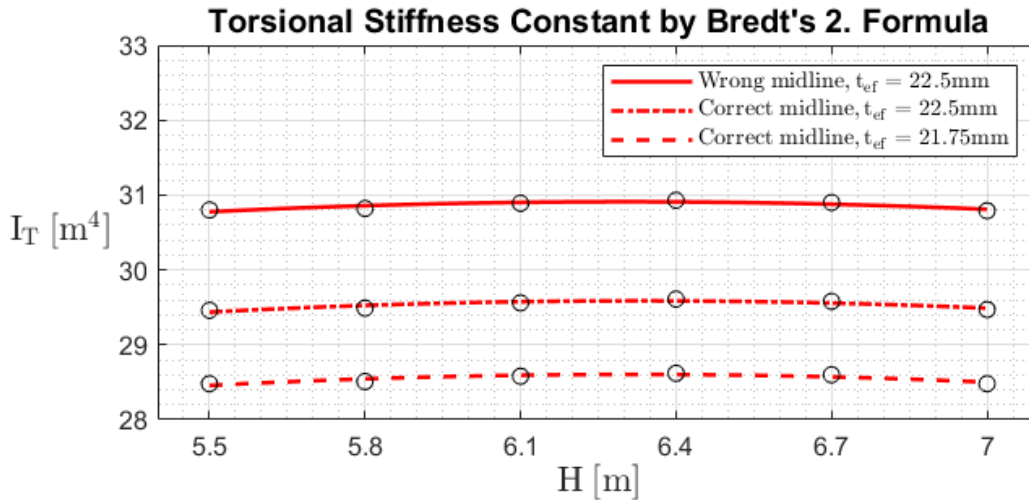


Figure 6.14: Torsional stiffness constant of from estimation with Bredts 2. formula

#### 6.4.4 Summary







The three analysis approaches show a near perfect correlation, but are slightly scaled in relation to each other. The effect of the difference of material area in the three computational models is seen in the stiffness parameter estimates. The simplified modelling method in CrossX performs well for the estimation of 2nd moment of area, but misses for the estimation of the torsional stiffness constant. For this estimate, a properly selected effective wall thickness must be selected for a simplified thin-wall section estimate to be accurate.

In conclusion, the results confirm that the selected girders do in fact have the same torsional stiffness (within a margin of 1 percent), which was the intention when selecting the shapes. However, the constraint value of  $31\text{m}^4$  used in chapter 5 is slightly overestimates the stiffness. It is further found that Bredts 2. formula is capable of providing accurate estimations for the torsional constant, given that the effective wall thickness is selected correctly. For a panel girder, this can only be done by adjusting it to the torsional constant estimate from an exact analysis (such as that of Abaqus or CrossX exact). Therefore, it is conceivable to perform only one exact girder analysis, while using Bredt's 2. formula with the adjusted effective wall thickness for the other girders. The 2nd moments of area about the principal axes can be determined by a simplified model.

Due to the overlap of material area in the CrossX, which resulted in correspondingly higher stiffnesses, the decision was made to use the stiffnesses attained from Abaqus in the further analysis in this thesis. Although the difference in stiffnesses is not large, this is chosen as the conservative measure. It is worth noting that if the panels in reality have more material around the joints due to rounding, the estimates of CrossX will be closer to the truth. However, this is not accounted for, as the only basis used for the panel geometry is the drawings presented in figure 4.6.

The cross sectional parameters used in further analysis for each of the six selected girders, are is summarized and presented in the table below.

Table 6.1: Calculated parameters of selected girders

H [m]	Girder Shape	Parameters
5.5		<ul style="list-style-type: none"> <li>• <math>A = 2.49 \text{ m}^2</math></li> <li>• <math>I_y = 12.0 \text{ m}^4</math></li> <li>• <math>I_z = 246.0 \text{ m}^4</math></li> <li>• <math>I_T = 28.4 \text{ m}^4</math></li> </ul>
5.8		<ul style="list-style-type: none"> <li>• <math>A = 2.49 \text{ m}^2</math></li> <li>• <math>I_y = 12.4 \text{ m}^4</math></li> <li>• <math>I_z = 246.3 \text{ m}^4</math></li> <li>• <math>I_T = 28.5 \text{ m}^4</math></li> </ul>
6.1		<ul style="list-style-type: none"> <li>• <math>A = 2.50 \text{ m}^2</math></li> <li>• <math>I_y = 12.8 \text{ m}^4</math></li> <li>• <math>I_z = 248.5 \text{ m}^4</math></li> <li>• <math>I_T = 28.6 \text{ m}^4</math></li> </ul>
6.4		<ul style="list-style-type: none"> <li>• <math>A = 2.51 \text{ m}^2</math></li> <li>• <math>I_y = 13.2 \text{ m}^4</math></li> <li>• <math>I_z = 251.4 \text{ m}^4</math></li> <li>• <math>I_T = 28.6 \text{ m}^4</math></li> </ul>
6.7		<ul style="list-style-type: none"> <li>• <math>A = 2.52 \text{ m}^2</math></li> <li>• <math>I_y = 13.4 \text{ m}^4</math></li> <li>• <math>I_z = 254.7 \text{ m}^4</math></li> <li>• <math>I_T = 28.6 \text{ m}^4</math></li> </ul>
7.0		<ul style="list-style-type: none"> <li>• <math>A = 2.53 \text{ m}^2</math></li> <li>• <math>I_y = 13.5 \text{ m}^4</math></li> <li>• <math>I_z = 258.6 \text{ m}^4</math></li> <li>• <math>I_T = 28.5 \text{ m}^4</math></li> </ul>

## Chapter 7

# Global Element Model

To be able to calculate the aerodynamic stability limits of the six selected bridge girders, the modal properties of the corresponding six suspension bridge element models first have to be determined. These modal properties have been extracted from global element models established with the use of Abaqus Scripting. A great time saving measure, was conducted when utilizing the former work of Mari Voll Dombu and Markus Gjelstad. In their master thesis of 2019, *Parametric modelling of a suspension bridge with an aluminium girder* [20], they presented a parametric model of the Langenuen Suspension Bridge, with the use of a Python script. This script writes a .INP-file, which uses Abaqus keyword references [35], to create the model. Some necessary changes were made to the script in order to achieve the desired global dimensions, and doubling the density of hangers. The script was investigated to ensure that the assumptions and weaknesses of the model is sufficiently known to the authors of this thesis. In addition, the calculated cross sectional properties were implemented for the six girders, respectively. This chapter will describe the process of establishing the element models, and present the resulting modal properties.

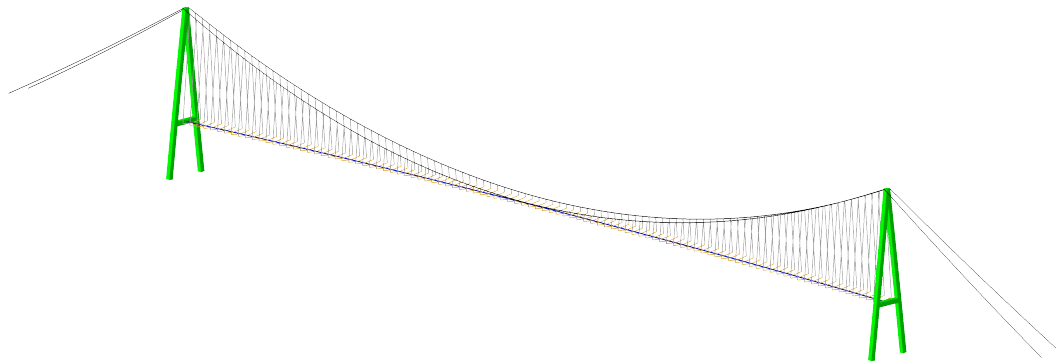


Figure 7.1: Abaqus Model of Langenuen Suspension Bridge

### 7.1 Global Design

The global design implemented is based on the design presented for the panel concept in Olav Olsen's report. However, some modifications were made. In the report, the chosen location of the fjord crossing resulted in a span length of 1235 m, but since then the location has been changed resulting in a span of 1220 m. Therefore, the span is set to 1220 m in the element models. Further, the side span lengths are set to be equal in the models, with



dimensions taken from Norconsult’s report of 2015. The rest of the global dimensions are based on the panel concept in the Olav Olsen’s report. The main dimensions are presented in figure 7.2.

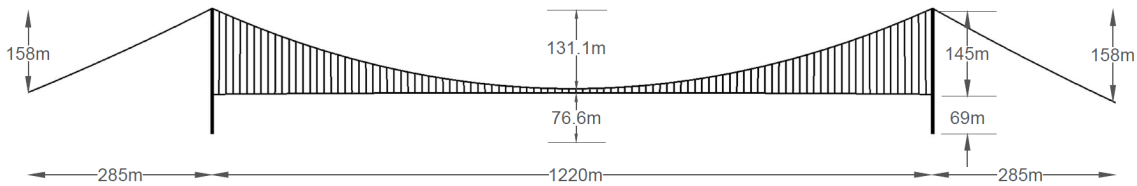


Figure 7.2: Global dimensions of FE-models

The dimensions presented in the figure are the dimensions of the bridge while under gravity load. The line representing the girder goes through it’s center of gravity. The vertical position of the center of gravity varied less than 30 cm, defined from the bridge deck. Therefore, a simplification was made by not changing the height of this center line for the different girders. The pylons are modelled with a simplified constant cross section, and not linearly varying, as in Olav Olsen’s design. Studies show that the modal properties of long span suspension bridges are not sensitive to pylon stiffness [13], so therefore this simplification is considered just. The cable planes of the models are inclined, in correspondence with the A-shaped pylons. The section properties of the different components of the global element model are given in table 7.1.

Table 7.1: Section properties

Component	Cross Section Geometry	A [m <sup>2</sup> ]	Material	E [GPa]	$\nu$	$\rho$ [kg/m <sup>3</sup> ]
Girder	See table 6.1	See table 6.1	Aluminium	70	0.32	2700
Main cables	Circular	0.3642	Steel	200	0.3	7850
Hangers	Circular	0.001521	Steel	210	0.3	7850
Pylons	Hollow rectangle	16	Concrete	35	0.2	2650

## 7.2 Modelling

For the modelling of the pylons, main cables and hangers, B33 elements have been used, which represent beam behaviour according to Euler Bernoulli theory [36]. As for the girder, the so-called ”spine-beam approach” has been implemented, where the bridge girder is modelled as 1D wire elements located through the center of mass of the cross section. This method has been proven to represent adequate global behaviour when modelling long-span suspension bridges [33]. The element type used for the girder is the B32 Timoshenko element. These have generalized cross sections, where the properties for each of the six selected girders can be implemented. These properties include solid material area, 2nd moments of area, torsional stiffness constant, Youngs modulus, Poission’s ratio and density. Additional inertia force contributions, due to different extra girder components such as the asphalt on the deck, must also be included. The details regarding this is explained in the next section. The girder is further connected to the hangers with the use of special connection elements, which are mass-less and have superficially high stiffness. These are highlighted with brown color in figure 7.3.

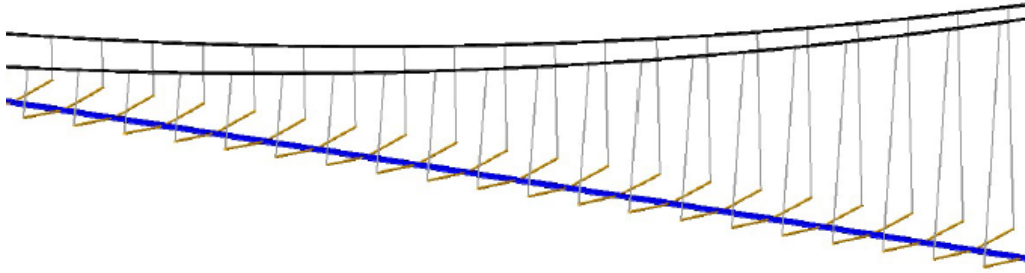


Figure 7.3: Connection elements between the hangers and the girder

The idea is that the spine-beam approach will result in sufficiently similar modal properties as a girder modelled with shell elements, but is less time consuming to implement.

The boundary conditions used in the model are indicated in figure 7.4. The anchorage points are fixed in translation, while the pylons are both fixed in translation and rotation. The interaction between the bridge girder and the pylons uses a horizontal spring to be able to imitate roller sections. All of the other part interactions are tied as fixed connections. Using fixed connections between the main cables and the hangers is not perfectly accurate and has to be considered when evaluating the modal properties.

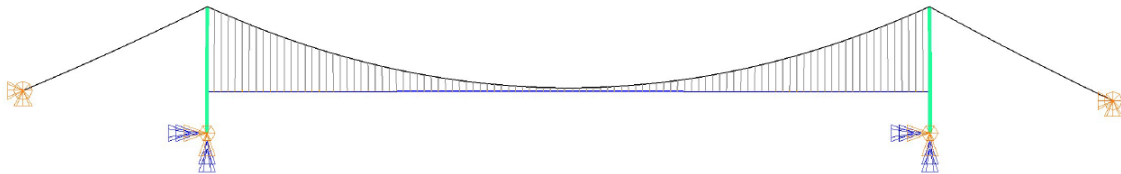


Figure 7.4: Boundary conditions of the FE-models

The gravity load is applied in three steps. First, it is applied to the pylons, secondly, to the main cables, and thirdly, it is applied to the girder and hangers. It is first after all these gravity load steps have been executed that the global dimensions shown in 7.2 are attained.

### 7.3 Girder Inertia

The solid material area of the girders, given in table 6.1, does not account for all material attached to the girder. There are additional components, such as bulkheads, asphalt and hanger heads, that must be included, in order to provide the true mass of the girder. In the python script, these components are accounted for by adding their respective inertia force contributions, one by one. The keyword command for used for this operation is `*BEAM ADDED INERTIA` [20]. The code used for girder 5.5 m can be seen in figure 7.5.

```

734 # -----
735 # ----- ADD BEAM GIRDER INERTIA -----
736 # -----
737 mdb.models['Model-1'].keywordBlock.synchVersions(storeNodesAndElements=False)
738 mdb.models['Model-1'].keywordBlock.replace(111, """
739 *Beam General Section, elset="Girder set", poisson = 0.32, density=0., section=GENERAL
740 2.4881, 11.97, 0., 245.98, 28.43
741 0.,1.,0.
742 7e+10, 2.6515e+10
743 *BEAM ADDED INERTIA
744 6718, 0., 0, 0., 32307, 664136, 0.
745 902, 0., 0, 0., 1786, 67799, 0.
746 4820., 0., 2.024, 0., 402, 212482., 0.
747 40.5, -15.5, 1.792, 0., 0., 0., 0.
748 40.5, 15.5, 1.792, 0., 0., 0., 0.
749 534., 0., 0, 0., 0., 0., 0. """)
750 """
751
752 From above
753 1: Aluminum panels + beams
754 2: Bulkheads
755 3: Asphalt
756 4: Hanger heads left
757 5: Hanger heads right
758 6: Equipment, fences and other mass
759 """

```

Figure 7.5: Python code for adding beam girder inertia, for girder 5.5 m

The respective mass components included are listed in the lower section of the code. One line of code is given for each component, containing the six properties [38]:

1. Linear mass [kg/m]
2. Horizontal eccentricity  $e_y$  [m]
3. Vertical eccentricity  $e_z$  [m]
4. Orientation angle [ $^\circ$ ]
5. Local rotary inertia about the horizontal axis  $I_{11}$  [kgm<sup>2</sup>/m]
6. Local rotary inertia about the vertical axis  $I_{22}$  [kgm<sup>2</sup>/m]

Many of the properties vary between the six girders. They have all been individually calculated and implemented in the respective python scripts. The different properties are given in table 7.2. All varying properties are given in detail in appendix C.

Table 7.2: Input for beam girder inertia

Inertia component	Linear mass [kg/m]	$e_z$ [m]	$e_y$ [m]	Rotational inertia $I_{11}$ [kgm <sup>2</sup> /m]	Rotational inertia $I_{22}$ [kgm <sup>2</sup> /m]
Girder	6718 - 6844	0	0	32307 - 36562	664136 - 698294
Bulkhead	902	0	0	1786 - 2376	67799 - 60377
Asphalt	4820	0	2.024 - 2.058	212482	402
Hanger head	81	+/- 15.5	1.792 - 1.826	0	0
Other equipment	534	0	0	0	0

The resulting total inertia forces for the six girders, have also been calculated manually, and are visualized presented in figure 7.6. The values can also be read in appendix C.

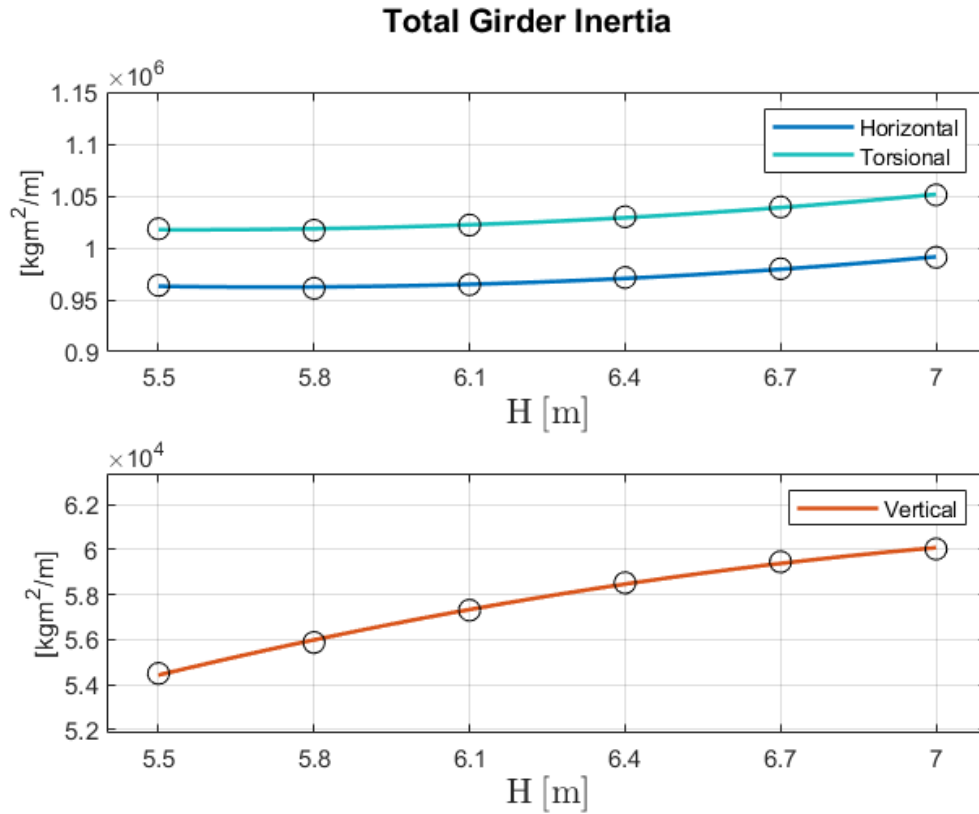


Figure 7.6: The torsional, horizontal and vertical mass of the six girders

The variation between the six girders is about 3% for the torsional and horizontal inertia forces, while it is about 10 % percent vertically. It is seen from figure 7.6 that the inertia forces generally increase with the height of the girder. However, it is the girder of height 5.8 m that has the smallest total torsional and horizontal mass. The reduction in inertia from the 5.5 m to the 5.8 m girder, comes from the bulkhead inertia contribution, which is plotted for every girder and shown in figure 7.7.

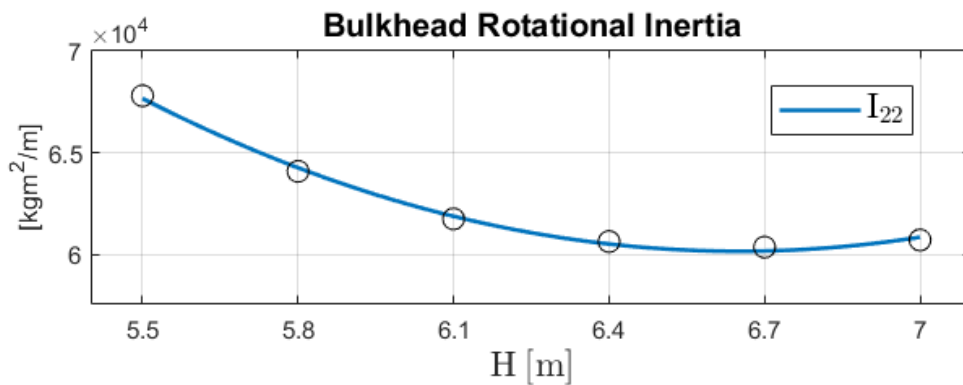


Figure 7.7: The rotational inertia  $I_{22}$  of the bulkheads of the six girders

Considering the total torsional mass, it is the main contributor is the inertia forces are the girders themselves. They account for more than 70 %. The bulkheads contribute about

6 %, the asphalt about 21 % and the hangers about 2%. All values for the total inertia forces are given in appendix C.

## 7.4 Modal Properties

The eigenfrequencies, mode shapes and generalized masses from the six global element models were identified by performing modal analysis in Abaqus. This section presents the results from the element model with the 5.5 m girder, while the results from all six element models are summarized in Appendix D.

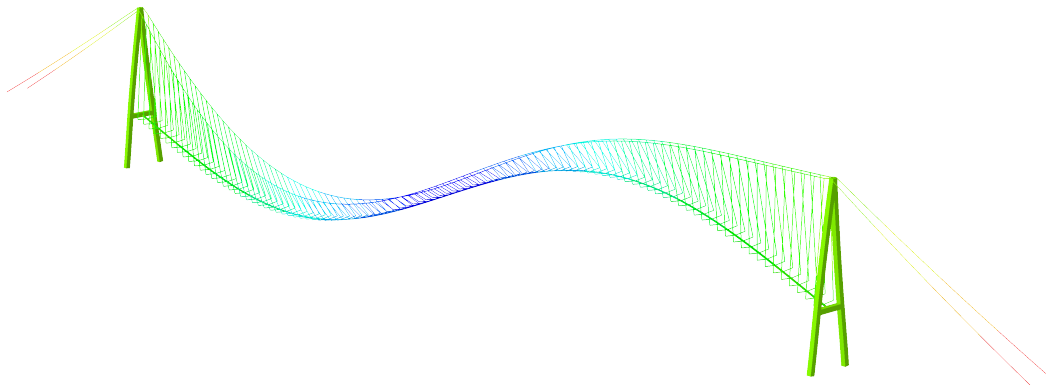


Figure 7.8: First vertical mode shape

The analyses for the six element models are instructed in each of the six python scripts *ElementModel\_5\_5m*, ..., *ElementModel\_7\_0m*, which are given as electronic attachments. The resulting mode shapes were visually inspected in the .ODB-files, and by considering the participation factors in the three degrees of freedom (horizontal, vertical, torsion) in the .DAT-files. In addition, the .DAT-files were inspected to uncover potential errors. Through this evaluation, the global mode shapes, dominated by girder deformation, were identified. The modes dominated by deformation in the cables and hangers are not relevant for the stability of the bridge, and were thus not further considered.

The modal properties from the element model with girder of height 5.5m, is shown in table 7.3. All the global mode shapes identified in the first 40 modes from Abaqus are included. The notation used for the global modes is based on their main DOF direction of motion (H/V/T), as symmetric or asymmetric (S/A), and a numbering for this combination. This categorization is useful to determine the mode combinations included in the critical wind speed calculations.

Table 7.3: Modal properties 5.5 m

Mode	Abaqus no.	Generalized mass $\tilde{M}_i$ [kg]	Frequency [Hz]	Displacement Plot		
				Horizontal	Vertical	Torsion
1HS	1	$1.103 \cdot 10^7$	0.057			
1VA	2	$1.195 \cdot 10^7$	0.107			
1VS	3	$6.262 \cdot 10^6$	0.143			
1HA	4	$1.024 \cdot 10^7$	0.156			
2VA	6	$1.063 \cdot 10^7$	0.219			
2VS	7	$1.012 \cdot 10^7$	0.220			
3VS	11	$9.845 \cdot 10^6$	0.298			
2HS	13	$5.414 \cdot 10^6$	0.310			
3VA	23	$1.155 \cdot 10^7$	0.377			
3HS	26	$5.303 \cdot 10^6$	0.395			
1TS	27	$5.198 \cdot 10^6$	0.415			
1TA	28	$6.692 \cdot 10^6$	0.456			
4VS	29	$1.112 \cdot 10^7$	0.475			
4VA	37	$1.143 \cdot 10^7$	0.583			
2HA	38	$9.529 \cdot 10^6$	0.612			

It is seen that the first mode shape is the symmetric horizontal mode shape with one wave top, which has a natural frequency of 0.057 Hz. The first vertical mode shape has two wave tops and a natural frequency of 0.107 Hz. The absence of a vertical mode shape with one wave top is expected for a suspension bridge, as such a motion is restricted by the cable geometry. The first and second torsional modes appear as mode no. 27 and 28 in the Abaqus analysis, with a natural frequencies of 0.415 and 0.456 Hz.

The modal properties from the six different element models were further inspected and compared. The comparison showed that the fundamental mode shapes are the same, and their eigenfrequencies vary little. The frequencies of the global mode shapes, up to the second asymmetric horizontal mode, have been plotted for the six different models, which is shown in figure 7.9. A 2nd order polynomial fit has been implemented to illustrate the development of the frequencies between the different girders.

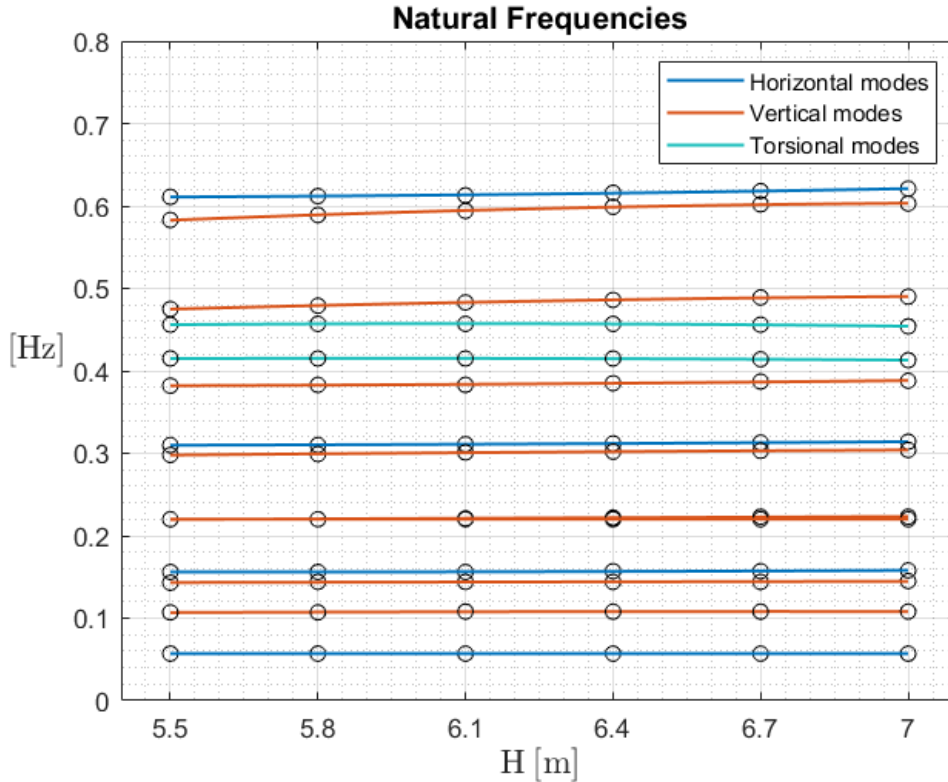


Figure 7.9: Comparison of the natural frequencies between the six element models

The results show that both the horizontal and vertical frequencies increase slightly when the girder height increases. This relative difference becomes larger for the modes of higher frequencies. For the plotted modes, the maximum horizontal frequency variation is 1.6% (the 2HA-mode), and the maximum vertical frequency variation is 3.4% (the 4VA-mode). As for the torsional mode shapes, the natural frequencies decrease slightly when the girder height increases. The frequency of the first torsional mode decreases 0.5% from girder 5.5 to girder 7.0 m, while the second mode decreases 0.7%. All in all, these variations are considered to be quite small.

The frequencies of the mode shapes are effected by the stiffness and mass of the girders, in addition to contribution from the cables and hangers. The increase of horizontal and vertical stiffness in the girders, as shown in chapter 6, contributes to an increase of frequencies, while the increase of inertia forces, as shown in the previous section, contributes to a decrease. It is therefore seen that the frequency-increasing effect of the stiffness slightly outweighs the frequency-decreasing effect of the mass, for the horizontal and vertical modes. The fact that the variation in frequency is higher for higher modes can be because the girder stiffness has a higher participation to the global stiffness for higher vertical modes than for the lower modes. As for the torsional modes, the slight decrease in natural frequencies is due to the increase of torsional inertia forces, since the torsional stiffness is constant.

All in all, the natural frequencies remain relatively unchanged among the six element models. This was identified as one of the possible benefits of selecting girder shapes based on constant torsional stiffness, as described in chapter 5. With approximately the same modal properties, it can be assumed that the effect of the aerodynamic properties of the girder shapes are essentially isolated in results from the aerodynamic stability calculations.

# Chapter 8

## Wind Tunnel Tests

Wind tunnel tests were performed on section models of each of the six selected girder shapes. The tests were conducted at the Fluid Mechanics Laboratory at NTNU. The resulting wind tunnel test data was further used to identify the static coefficients and aerodynamic derivatives of each of the sections, by the methods described in chapter 2.8 and 2.9.

When the COVID-19 pandemic reached Norway in March, NTNU went into a lock-down. This put the planned wind tunnel tests in jeopardy. However, about 5 weeks later, the university gradually opened again. The access to the laboratories was first granted to the employees. Therefore, the wind tunnel tests was conducted by Professor Ole Øiseth and Staff Engineer Per Øystein Nordtug. The authors are grateful for their work.

### 8.1 Section Models

Six section models were made from the selected girders, in a scale of 1:70. The function of the models is solely to represent the outer shapes of the girders. For practicality, it is ideal that the models are as light and stiff as possible. This is to minimize effects of mass inertia which can disturb measurements if they become too significant. They were made with the material divynycell H, which has high stiffness and low weight. The process of milling and assembling the models was lead by Gøran Loraas and Ole Øiseth. The authors gratefully acknowledge this help.

Each model was constructed by two plates of divynycell H, which were glued together. A circular aluminum pipe, with an outer diameter of 40 mm and a wall thickness of 1 mm was placed in the center. This pipe gives the models their rigidity, and serves as the connection points for the model to the test rig. In addition, two cylindrical cavities were milled to further reduce the mass of the models. When the glue connecting the plates had dried up, the outer shapes of the models were milled, as seen in figure 8.1. This milling was an effective and accurate process, resulting in the completion of 6 complete section models in a span of 3 days. The code instructing the milling was developed by supervisor Ole Øiseth.



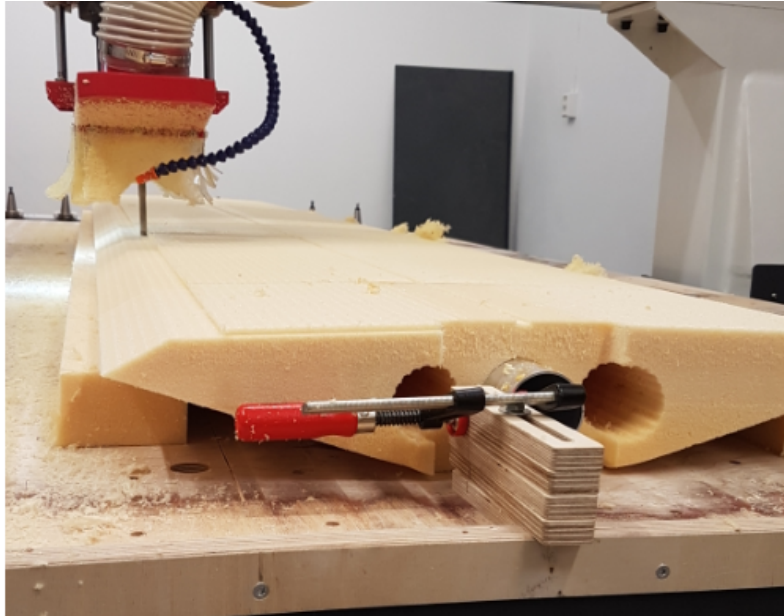


Figure 8.1: Milling of the 7.0 m model section at NTNU

The resulting section models have heights varying between 7.86-10.00 cm, and widths varying between 50.57-52.29 cm. The surfaces of the models were lacquered in order to avoid dust and marks to attach to the porous material.

### 8.1.1 Fences

Studies conducted by Siedziako and Øiseth [34] on Hardanger suspension bridge showed that including girder details such as fences, rails and guide vanes had a significant effect on the estimates critical wind speed. Fences are included in the wind tunnel tests in this thesis. Their exact position can be seen in figure 4.3. It has not yet been determined if, and how, rails and guide vanes applied, and these are therefore not considered.

In the past, fences used in wind tunnel tests at NTNU have been fabricated using a 3D printer. Although the method provides high accuracy, it is time consuming. A more simple method was used in this thesis, where the fences were milled from a plastic plate, with the same machine that milled the bridge girders. This is a much more time efficient, but a little less accurate. Therefore, the level of detail in the fences had to be reduced. This was done by making the member cross sections rectangular instead of round, and reducing the density of members. The width of the members were increased in order to maintain the same surface area opposing the wind. By doing this, the simplified fences are expected to provide the same drag force as the original design. The basis for the rectangular fence design was a former design used at wind tunnel tests related to the Bjørnafjorden Bridge. It was further useful to produce the fences in a CAD-software, seen in figure 8.3, to provide the coordinates to be used in the milling.

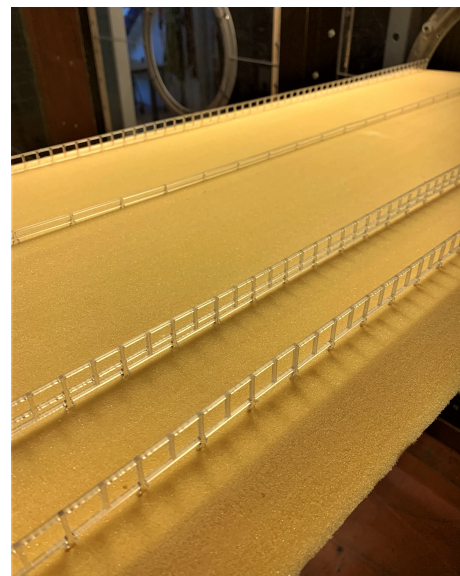


Figure 8.2: The fences mounted on the bridge deck

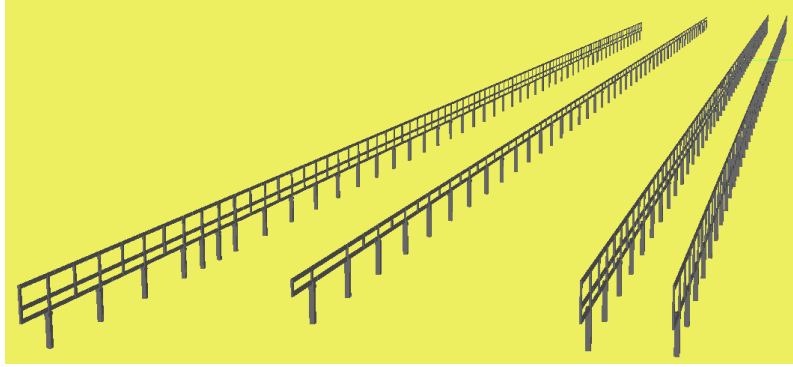


Figure 8.3: CAD-model of the fences

## 8.2 Experimental Setup

The tests are performed at the Fluid Mechanics Laboratory at NTNU. The experimental rig set up (presented in chapter 2.5) is able to perform a forced vibration test in arbitrary motion in the three DOFs: horizontal, vertical and torsion. The wind tunnel is a low-speed closed loop, with a 2.7 m wide, 2.0 m high and 11 m long test area. Therefore, the area of the exposed cross section of the section models is therefore less than 6% of the wind tunnel test area, which ensures no presence of the blockage effect described in section 2.6.1. The wind velocity profile at the inlet is uniform and close to laminar, with a turbulence intensity of about 0.2% [7]. Figure 8.4 shows one of the models mounted in the wind tunnel.



Figure 8.4: A section model mounted inside the wind tunnel

The actuators providing generating the motion of the section models are mounted outside the wind tunnel. The load cells, which measure the loads at each end of the model, are placed in the center of the circular holes on each side with a diameter of 25 cm [7].

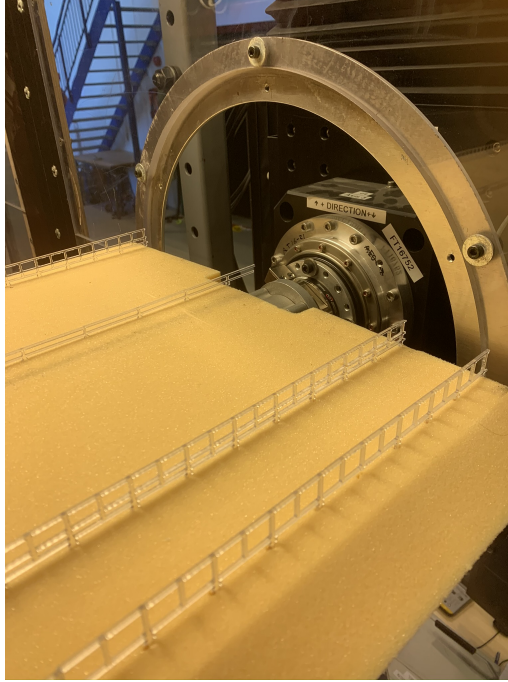


Figure 8.5: The section model connected to the load cells and actuators

### 8.3 Test Description

The wind tunnel test procedure used for the six section models is divided into three parts:

1. **Vortex shedding tests:** In this test, the wind speed is increased evenly while the section models are statically held in place, to observe if there is any occurrence of vortex shedding induced vibrations. The wind speeds resulting in vibrations are avoided in the next tests, as they create a major disturbance in the recorded loads.
2. **Quasi-static tests:** Quasi-static tests are performed to determine the static coefficients. As described in section 2.2, the coefficients are functions of the torsional rotation of the section models. During the wind flow, the section models are quasi-statically (slowly) rotated with a frequency of 0.05Hz, not cause inertia forces. This is done with wind speeds of 5.5, 9.3 and 12.2 m/s, respectively, in order to uncover if the models are dependent of the Reynolds number, i.e. if different wind speeds render different values for the static coefficients. The amplitude of the torsional motion is  $\pm 8$  deg. The procedure used for the identification of the static coefficients is presented in chapter 2.6.
3. **Single harmonic forced vibration tests:** This test is conducted to identify the ADs. As in the quasi-steady test, a reference still-air test is first performed to measure the inertia forces. Further, in-wind tests are performed with the sections subjected to single-harmonic oscillations in one of the DOFs: horizontal, vertical and rotational motion. Each of these tests provide data for the identification 6 ADs. The tests are conducted at two different wind speeds, and eight different oscillation frequencies, in order to provide in total 16 data points for each AD. Each of these points correspond to a different value of the reduced wind velocity,  $V_{red}$ . The procedure applied to identify the ADs is presented in chapter 2.7. An overview of the frequencies and amplitudes used in the test is given in table 8.1.

The air density varied between 1.170 and 1.184 kg/m<sup>3</sup> throughout the tests. As a conservative measure, 1.25 kg/m<sup>3</sup> is used in the estimation of the critical wind speed. An overview of the frequencies and amplitudes used in the tests is provided in table 8.1:

Table 8.1: Considered test values in the forced vibration test

Amplitude of vertical vibrations:	$\pm 1$ cm	Tested velocities:	Varies between models
Amplitude of horizontal vibrations:	$\pm 2$ cm	Tested frequencies:	0.25, 0.5, 0.8, 1.1, 1.4, 1.7, 2.0 and 2.5 Hz
Amplitude of torsional vibrations:	$\pm 2.0^\circ$ ( $\pm 1.0^\circ$ )	Reduced velocity range:	From 0.72 up to 3.64
Sampling frequency:	200 Hz	Duration of time series:	ca. 220 s

## 8.4 Test Observations

The tests were conducted successfully. Vortex shedding induced vibrations were observed to be most prevalent for the two lowest section models, corresponding to girder 5.5 and 5.8 m. Further, the observed magnitude of vibrations decreased as the heights of the section models increased, until the highest section model, which had significant vibrations. The wind velocities causing these vibrations were avoided in the forced vibration tests. The data needed for the identification of static coefficients and aerodynamic derivatives was successfully measured. The results are presented in the next chapter.

Due to a non-linearity seen in the static coefficient plot of the two highest section models, additional torsional oscillation tests were conducted for these models with a lower amplitude of  $\pm 1.0^\circ$  to stay within the area with linear behaviour. The data from these tests were used in the identification of ADs of these two girders.

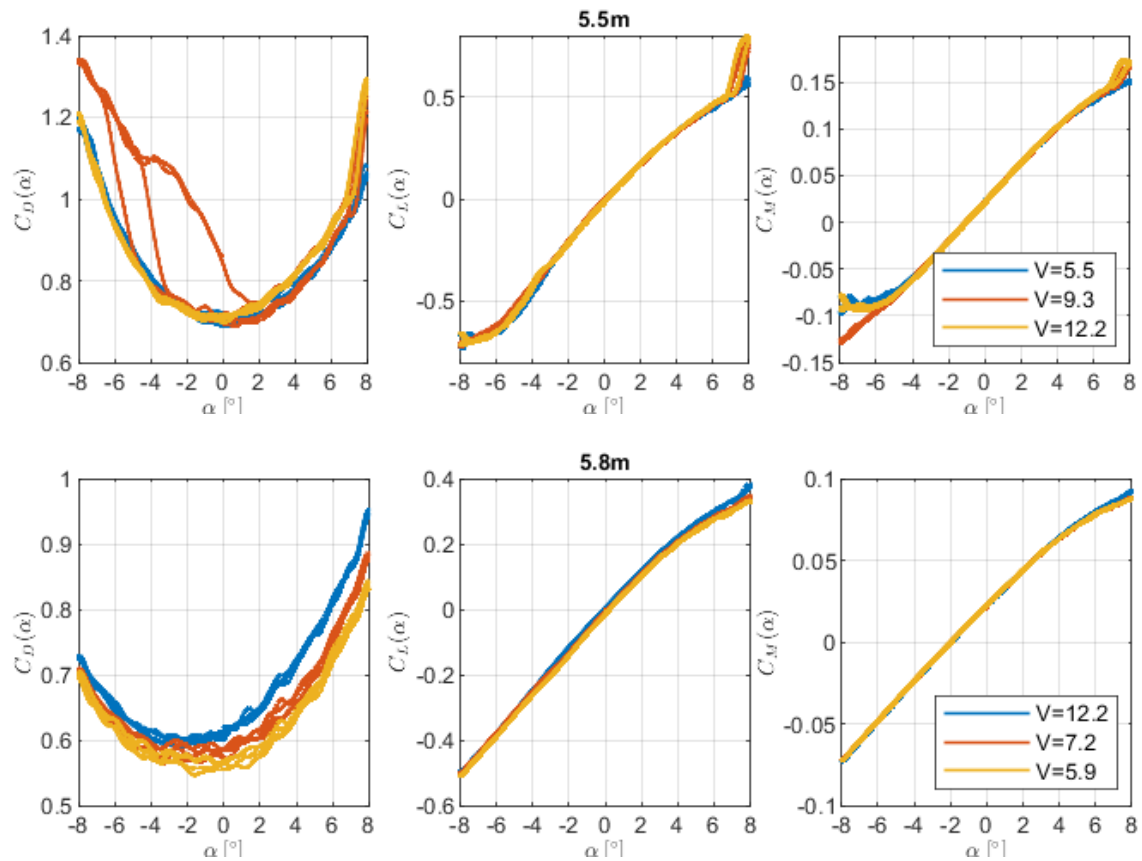
## Chapter 9

# Experimental Results and Predicted Stability Limits

This chapter presents the processed data from the wind tunnel test, i.e. the static coefficients and aerodynamic derivatives, and the results from the critical wind speed calculations. The instability behaviour of the respective girders is also investigated. Further, the results are compared between the six girders. A summarizing discussion regarding the results is conducted at the end of the chapter.

### 9.1 Static Coefficients

The static coefficients of the six girders were calculated for wind speeds of 5.5, 9.3 and 12.2 m/s, respectively. Plots of these directly generated by the code provided by the supervisor is presented below. The rotational amplitude used is in the range of  $\pm 8^\circ$ . It should however be noted that this is far beyond expected deformations a bridge girder.





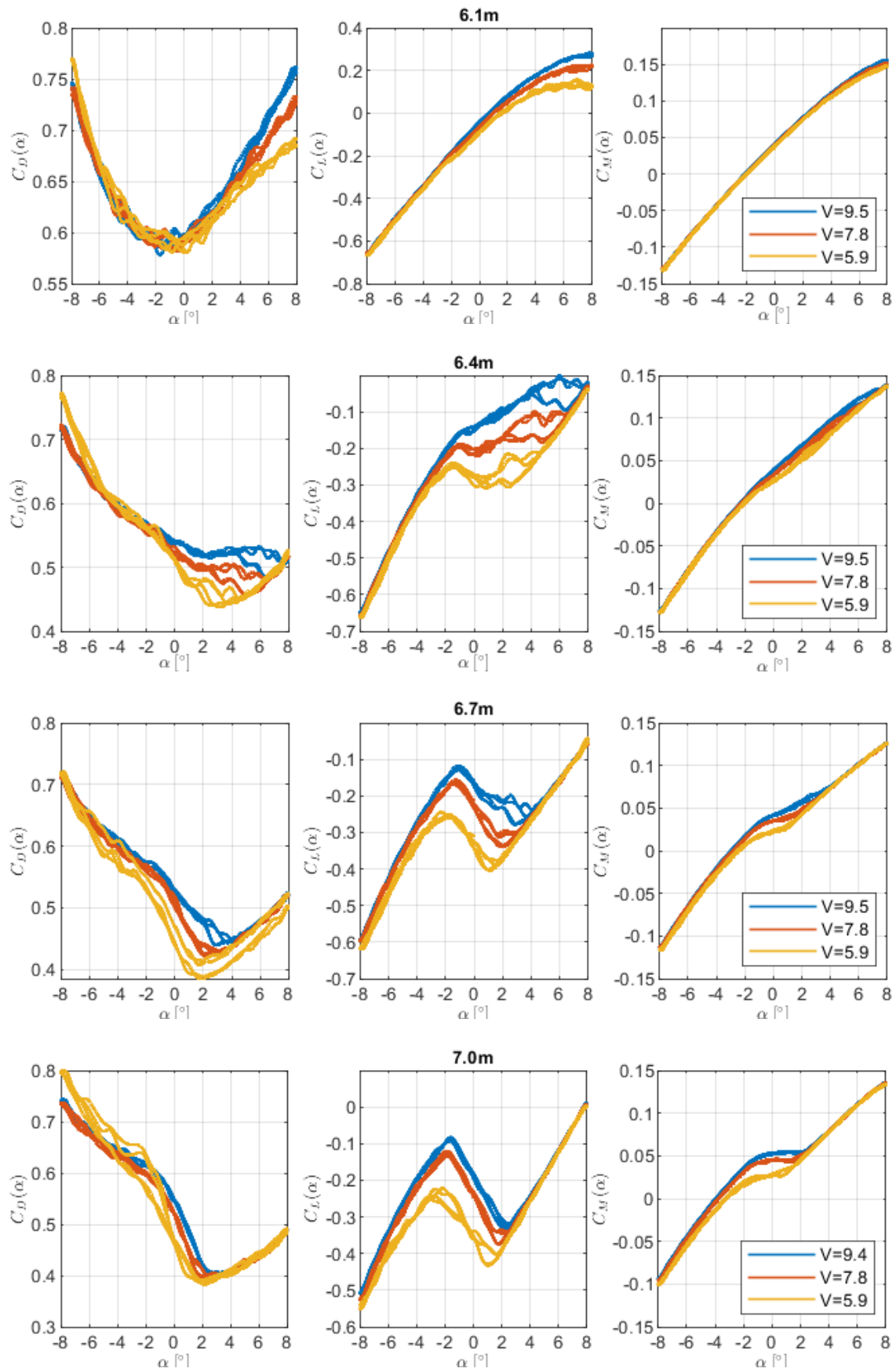


Figure 9.1: Static coefficients

It is seen from the plots that all three coefficients  $C_D$ ,  $C_L$  and  $C_M$  have some variation between the six girders. The smallest variation is seen in the moment coefficient  $C_M$ . It attains a relatively linear development throughout. The lift coefficient  $C_L$  also has a relatively linear development for the lower girders, but for the higher girders a non-linearity appears. The lift also becomes more negative as the girder height increases. The drag coefficient  $C_D$  has a typical parabolic shape for the lower girders, but its shape is radically changed for the three highest girders. It should be noted that the static coefficients are scaled by the varying width of the girders. This influences the translation of the coefficients between the girders. A better comparison between the coefficients could perhaps be attained by normalizing them by the constant width of the road lanes.

Because of the clear non-linearity in the lift coefficient of the two highest girders, 6.7 m and 7.0 m, the single harmonic torsional oscillation test was conducted with an amplitude from  $\pm 2^\circ$  to  $\pm 1^\circ$ , where the behaviour is linear. The negative lift coefficient for the higher girders makes sense when comparing the girder shapes to that of an airplane-wing. For a wing, the lift is achieved by making the air travel a longer path on the upper side, causing a pressure difference. The higher girder shapes can be considered as the shapes of an upside down wing, causing this negative lift.

The plots also reveal a Reynolds number dependency for some of the girders. This effect is seen when the static coefficient of the same girder are different for different wind speeds. Considering the rotation amplitude of  $\pm 2^\circ$ , this behaviour is particularly present in the lift coefficients of 6.4, 6.7 and 7.0 m. As described in subsection 2.8.1, this effect leads to some uncertainties regarding the scaling the results from a section model to a full scale girder.

## 9.2 Aerodynamic Derivatives

The wind tunnel tests described in the previous section resulted in a number of data points for each of the 18 ADs, for each of the six girders. These AD data points were obtained for values of the reduced wind velocities  $V_{red}$  on the interval  $[0.27, 3.64]$ . Functions for the ADs are further fitted to these points, with the use of third degree polynomials. Beyond the reduced velocity range of the experimental AD data points, these functions are constrained to a constant value. This section will show these AD-functions.

The AD data points and fitted functions are shown in the figures 9.3-9.8. Here, the ADs are shown as functions of reduced frequency,  $K$ , as this enhances the visualization of the fitted curves wrt. to the experimental ADs. The blue plus-signs indicate the experimental ADs, while the red lines indicate the fitted functions. In addition, the obtained ADs are presented as functions of the reduced velocity  $V_{red}$  in Appendix E. In these plots the Theodorsen's ADs derived from flat plate theory [41] are also plotted as a reference.

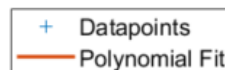
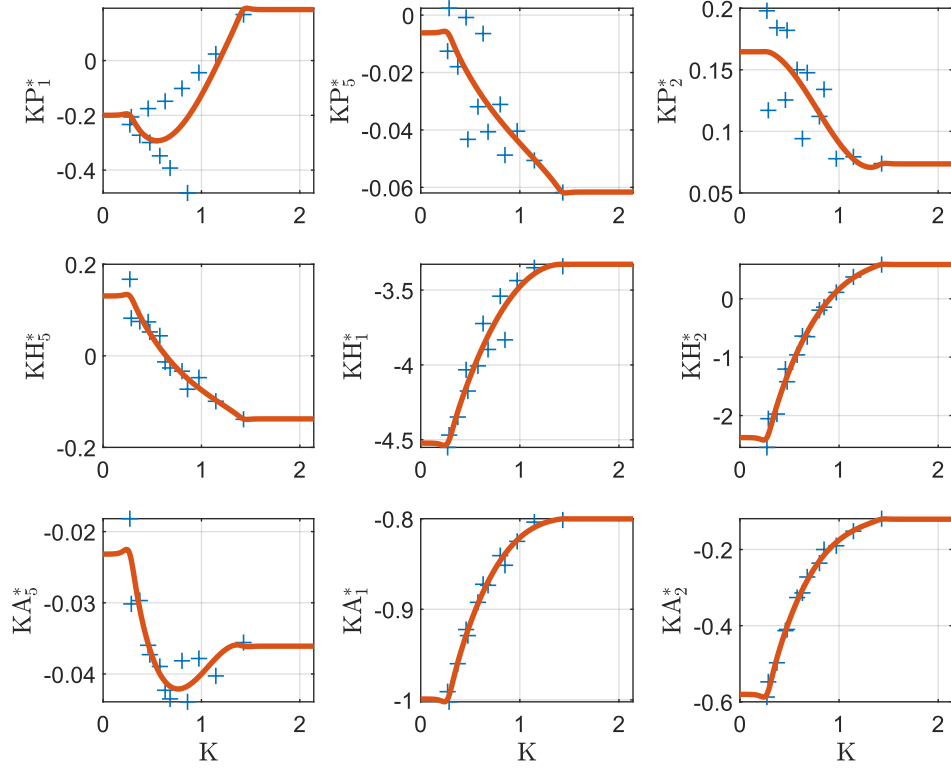


Figure 9.2: The legend used for the AD-fits

ADs related to  $\hat{K}_{ae}$  for 5.5m



ADs related to  $\hat{C}_{ae}$  for 5.5m

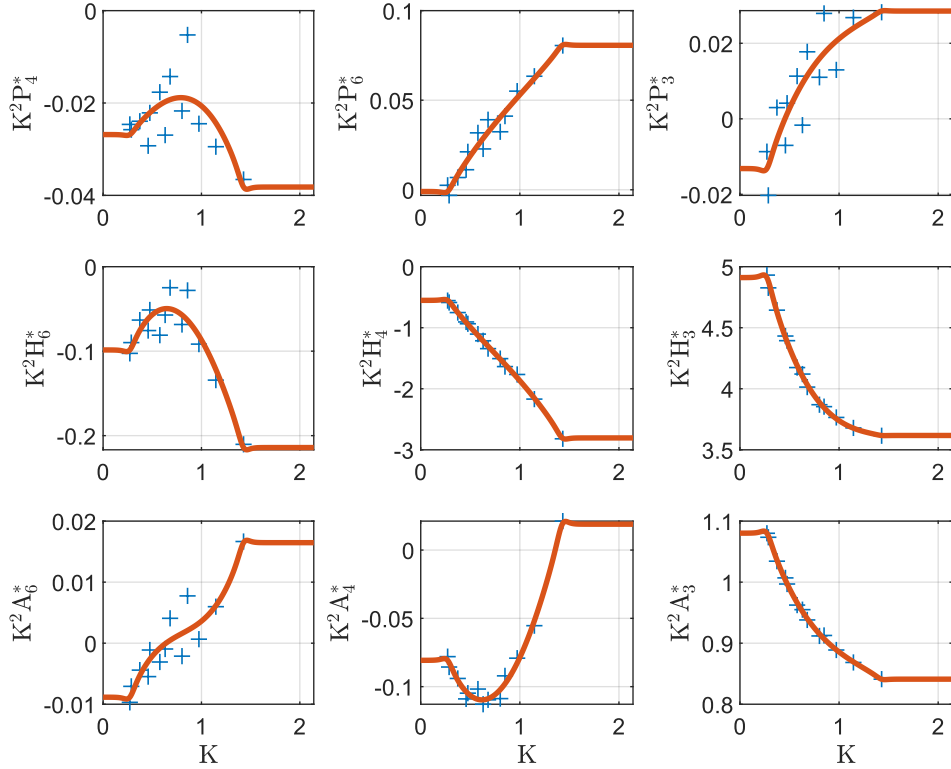
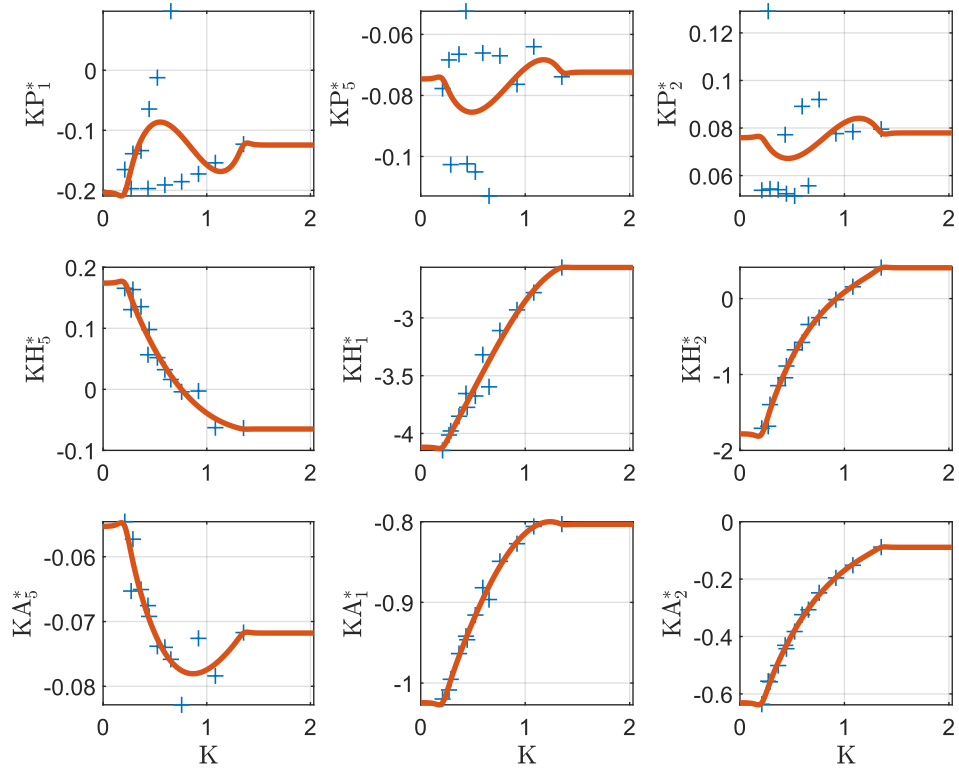


Figure 9.3: ADs for the 5.5 m girder



ADs related to  $\hat{K}_{ae}$  for 5.8m



ADs related to  $\hat{C}_{ae}$  for 5.8m

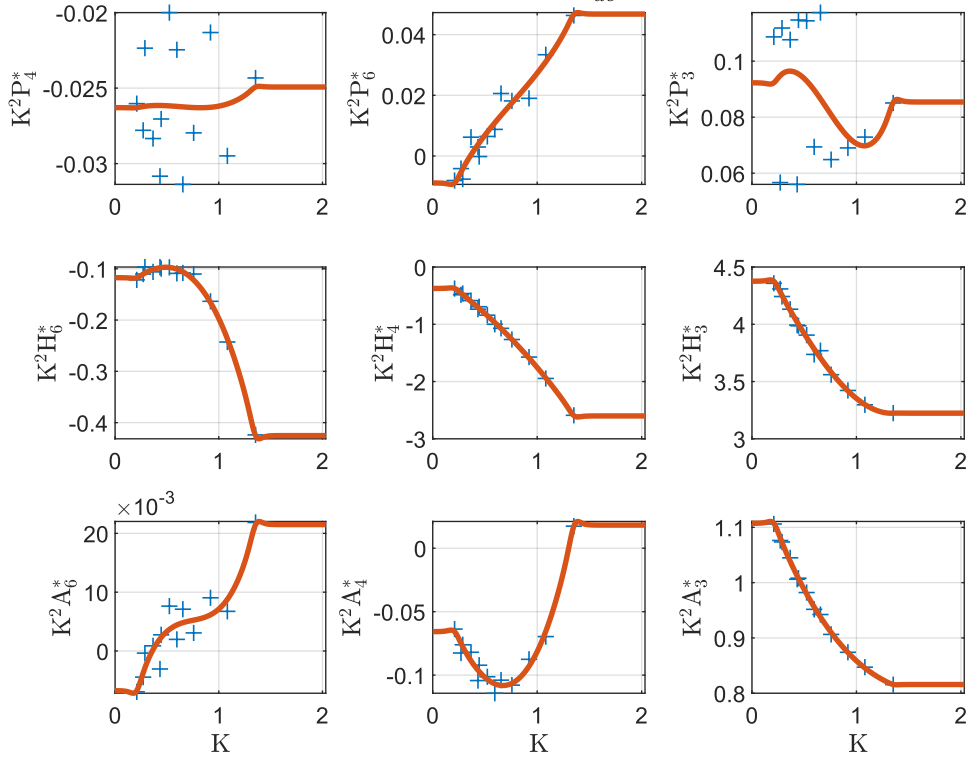
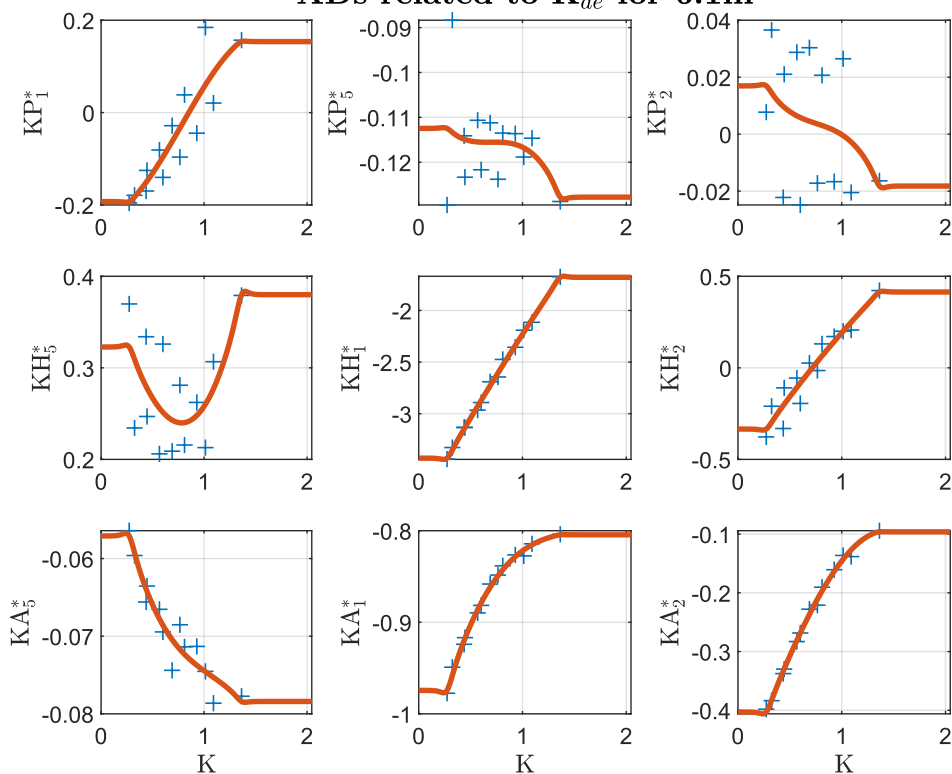


Figure 9.4: ADs for the 5.8 m girder

ADs related to  $\hat{K}_{ae}$  for 6.1m



ADs related to  $\hat{C}_{ae}$  for 6.1m

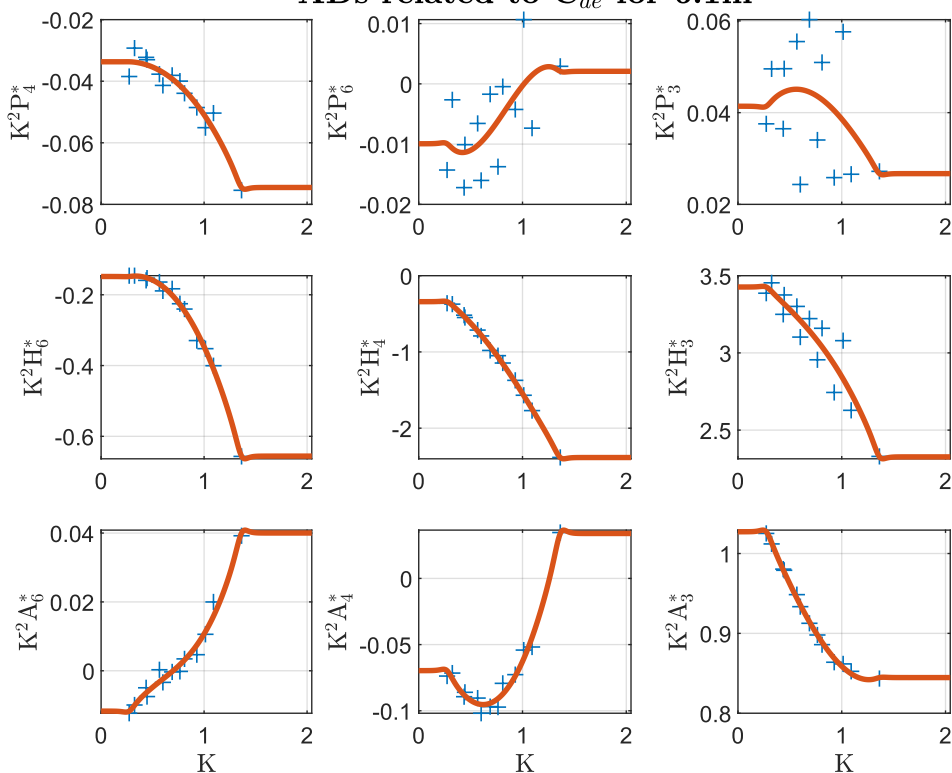
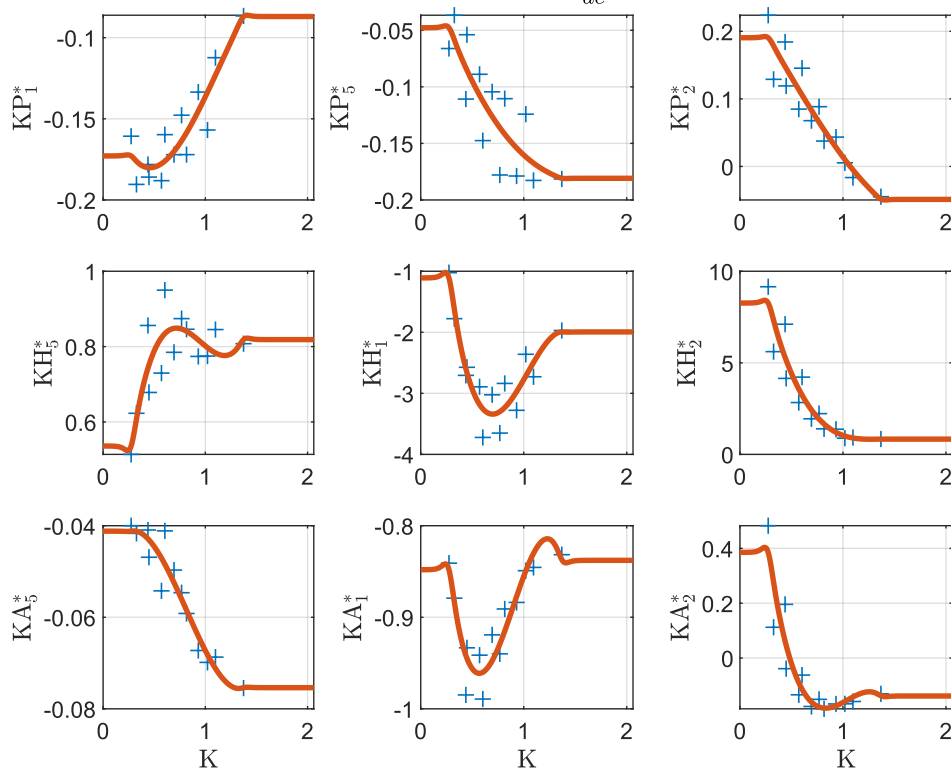


Figure 9.5: ADs for the 6.1 m girder

ADs related to  $\hat{K}_{ae}$  for 6.4m



ADs related to  $\hat{C}_{ae}$  for 6.4m

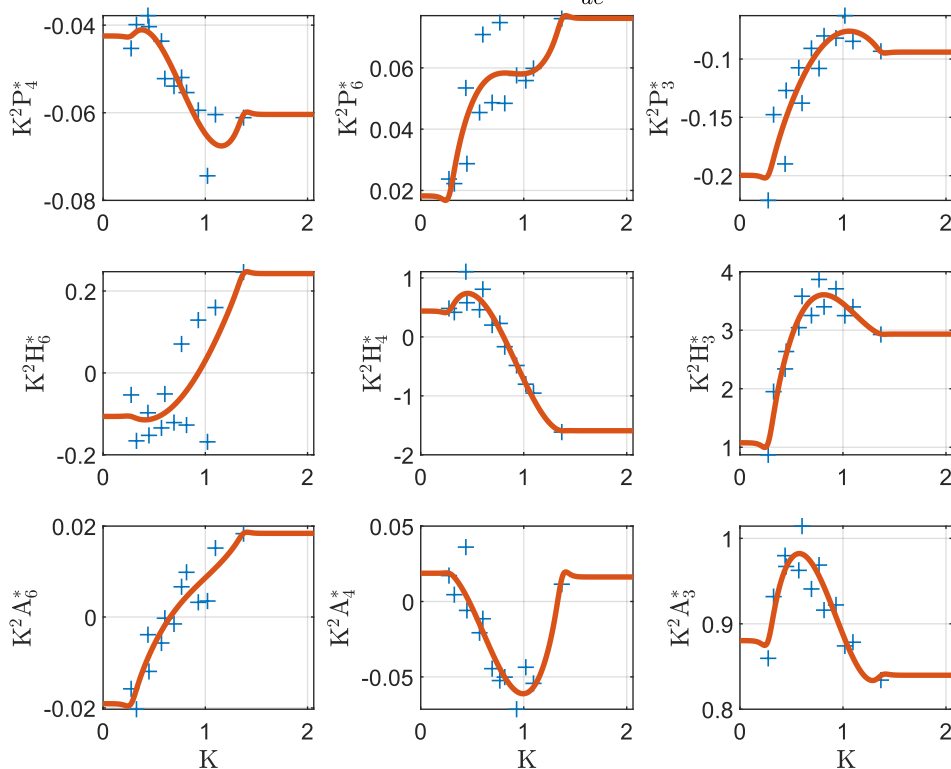
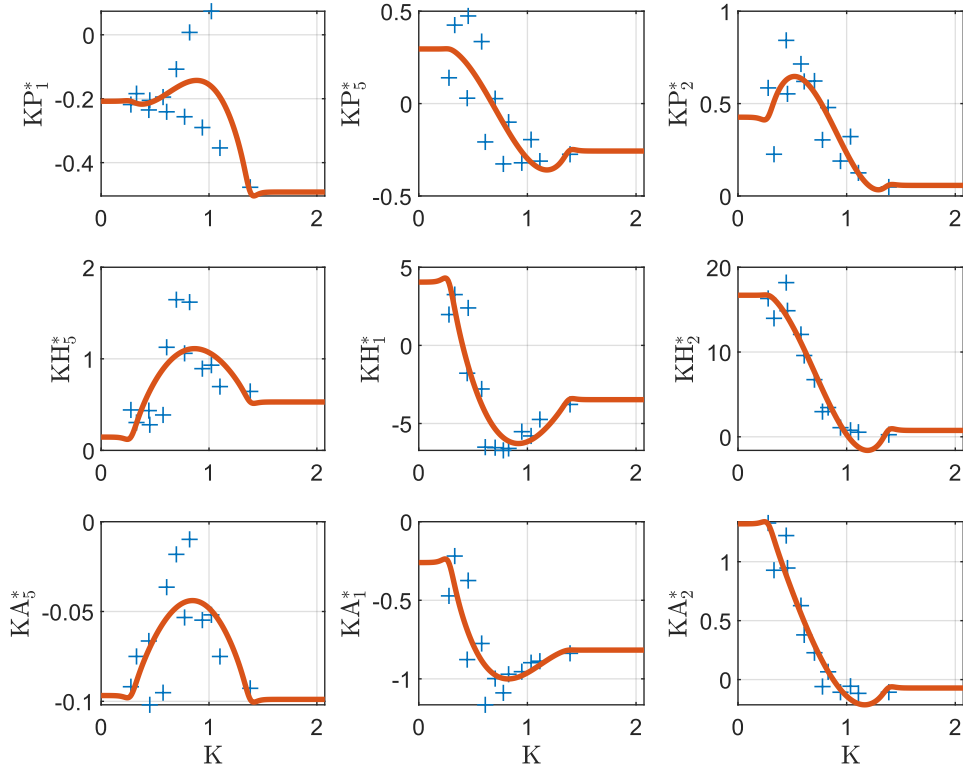


Figure 9.6: ADs for the 6.4 m girder

ADs related to  $\hat{K}_{ae}$  for 6.7m



ADs related to  $\hat{C}_{ae}$  for 6.7m

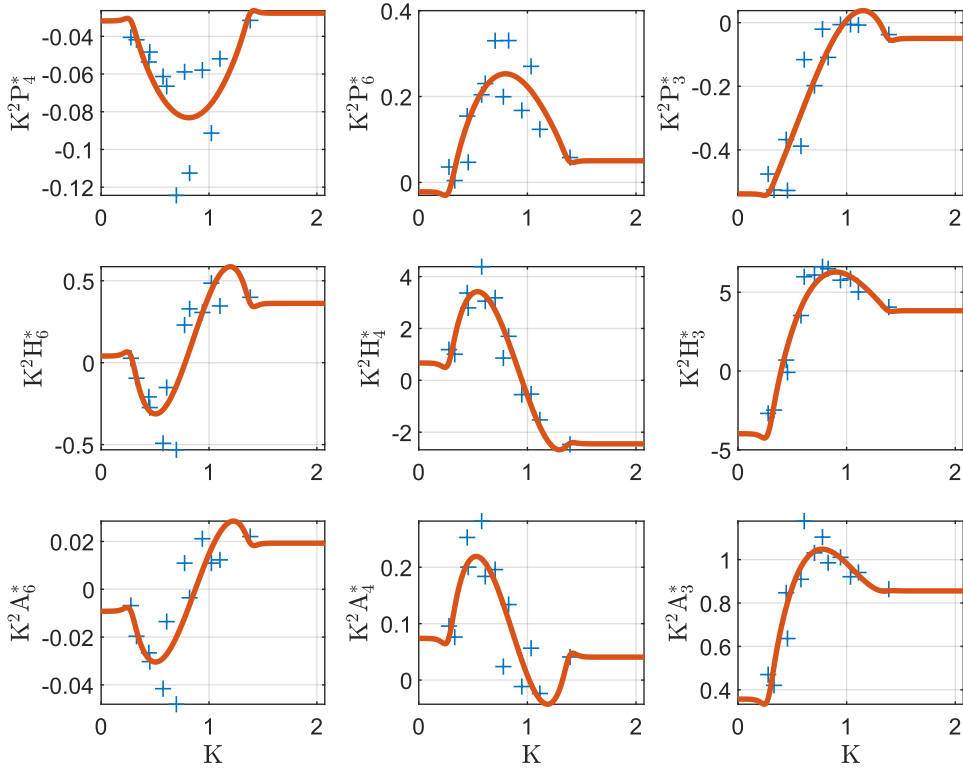


Figure 9.7: ADs for the 6.7 m girder

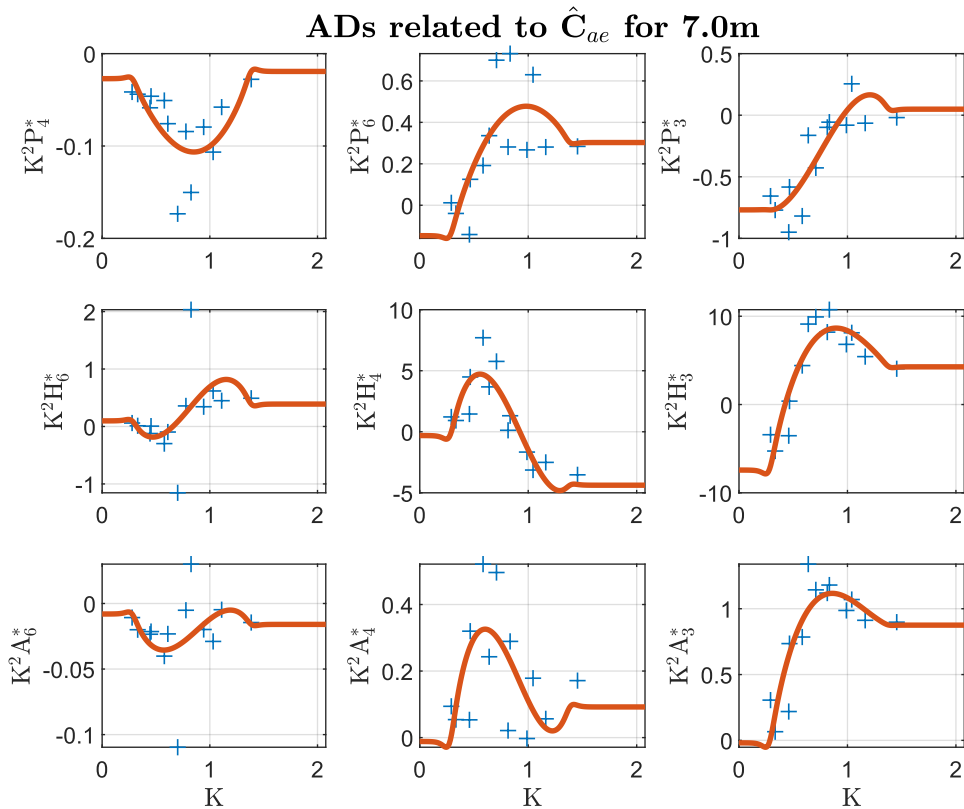
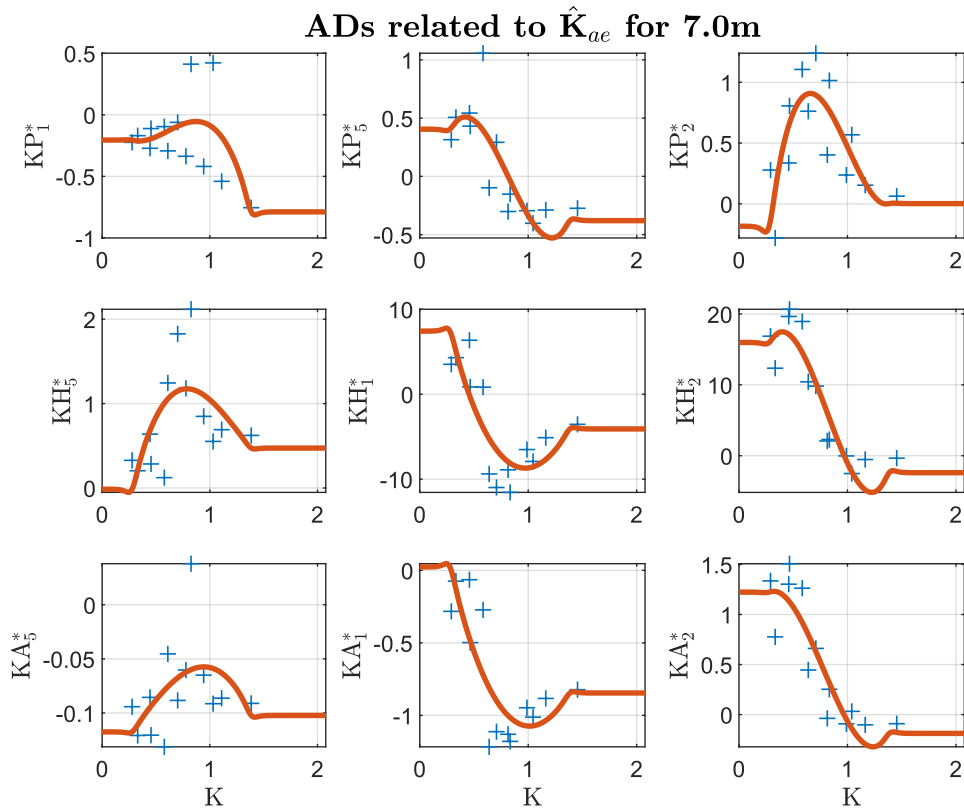


Figure 9.8: ADs for the 7.0 m girder

It should be noted that the fitting AD-functions to the experimental ADs may be performed in several ways, which will have an influence on the final stability limit results. A brief sensitivity analysis with regards to the fitted AD-functions is performed at the end of the next section.

The plots show that the resulting AD-functions and their quality vary somewhat between the girders. The critical ADs have an increasingly nonlinear behaviour for the higher girders. It is also seen that the higher girders have in general more scatter in the AD data points than the lower girders. This is for particularly the two girders 6.7 and 7.0 m. There is also generally some noticeable scatter in the ADs related to the self-excited drag force. The average magnitude of these ADs seems to increase as the girder height increases, which substantiates including them in the stability analysis to reveal if they have any influence on the stability limit. Also the ADs related to the vertical and torsional self-excited forces,  $H_1^*-H_4^*$  and  $A_1^*-A_4^*$ , have a presence of scatter, which may introduce uncertainties in the stability analysis of these girders.

Some of the scatters in the plots have a regular offset pattern, which has its natural explanation in the fact that the tests are conducted with two different wind speeds. This indicates that some ADs are dependent of the Reynolds number, which is a source of uncertainty. Scatter in the ADs related to the self-excited drag force may be due to the fact that the inertia forces in the section model dominate the generally low magnitude self-excited drag force. However, these ADs are of less importance wrt. the aerodynamic stability. The scatter seen for the ADs related to vertical and torsional self-excited forces can be due to higher order self-excited forces, as the ADs only capture the linear contribution [7] [45].

In summary, the polynomial AD-function fitting for four girders of height between 5.5 m to 6.4 m has low uncertainty for the ADs related to vertical and torsional self-excited forces. The two girders 6.7 and 7.0 m have a little more uncertainty however, as there is more scatter and there are indications of non-linearity and higher order self-excited forces.

In order to more clearly compare the obtained AD-functions of the six girders to each other, they are plotted together in figure 9.10 with the color representation as shown in figure 9.9.



Figure 9.9: The legend used for the AD-plots

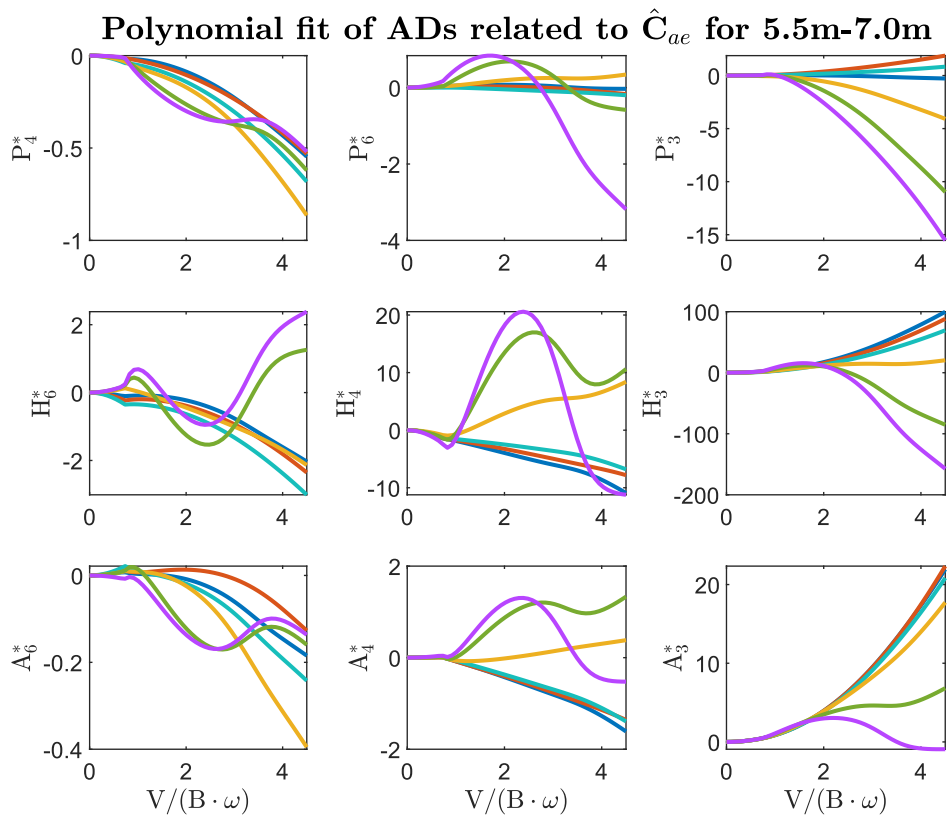
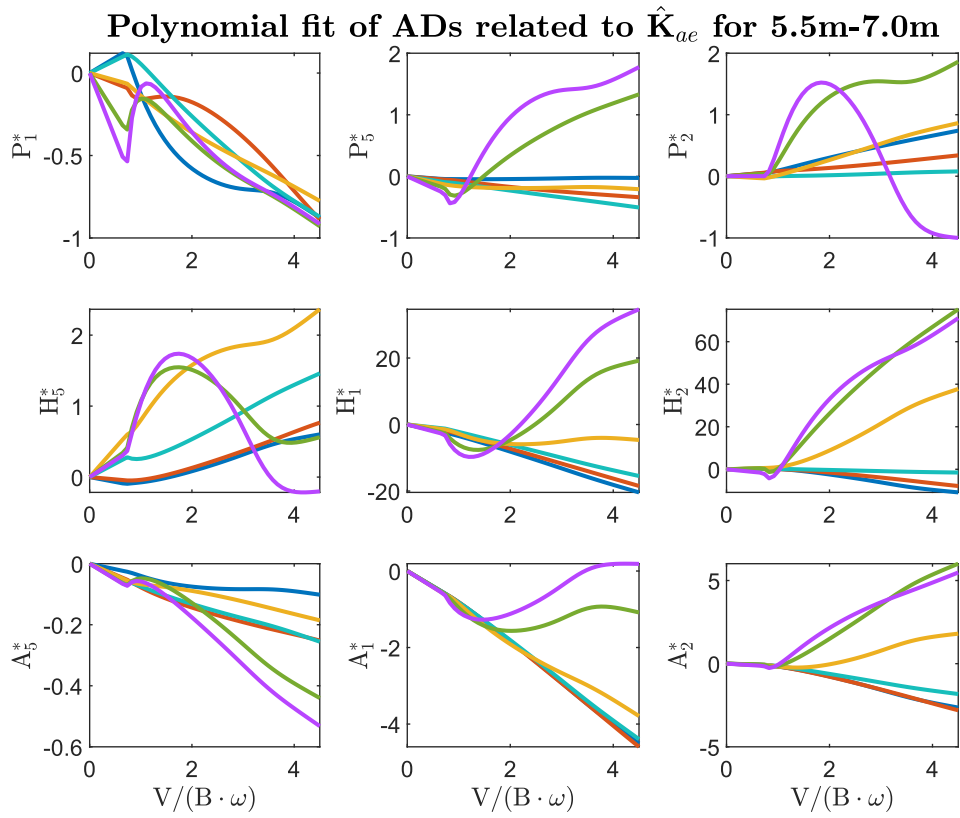


Figure 9.10: Comparison of polynomial fit

It is observed from the comparison plots that the AD-functions of the lower girders 5.5, 5.8, 6.1 m have a really similar development. This is an interesting result, as the girders do have notable differences in their geometric shape. The two highest girders 6.7 and 7.0 m also have a similar behaviour, clearly separated from the three lowest girders. The behaviour of the girder of height 6.4 m is somewhere in between the lower and higher girders. Further, some interesting observations are made when considering the behaviour of the critical ADs.

It is seen that  $H_1^*$  remains negative for 5.5-6.1 m while it is just barely negative? for 6.4 m. For the two girders 6.7 and 7.0 m, it is clearly positive. Negative values for  $H_1^*$  has a stabilizing effect for flutter, while positive values can increase the risk of galloping, as described in subsection 2.5.2. The AD  $H_3^*$  it is observed to have high absolute values for girders 5.5-6.1 m and 6.7 and 7.0 m, for  $V_{red} > 2$ . This is known to have a destabilizing effect towards flutter.

Further,  $A_1^*$  shows a negative linear development for girders 5.5 m-6.4 m, while it remains closer to zero for 6.7 m and 7.0 m. Low absolute values of  $A_1^*$  has a stabilizing effect with regards to flutter. Considering  $A_2^*$ , it is seen that it remains negative for girders 5.5 m-6.1 m, which adds damping for torsional flutter. However, it is barely positive for 6.4 m, and for 6.7 and 7.0 m it is clearly positive. This can make the higher girders subjected the instability phenomena of dynamic instability in torsion, described in subsection 2.5.3. Further,  $A_3^*$  is strongly positive for 5.5 m-6.4 m, while it is just barely positive for 6.7 m and 7.0 m. Low absolute values of  $A_3^*$  has a driving effect for flutter.

It is a not unusual to set all non-critical ADs, i.e. the ADs besides  $H_1^* - H_4^*$  and  $A_1^* - A_4^*$ , to zero in aerodynamic stability calculations. However, studies have shown that the non-critical ADs still can play an important part in the estimation of the critical wind speed [7]. All 18 ADs are included and applied in the further stability calculations in this thesis.

### 9.3 Predicted Stability Limits

Calculations of the critical wind speeds were executed using Matlab-programs provided by our supervisor Professor Ole Øiseth. This program implements the AD-functions described in the previous section, and the modal properties described in chapter 7. In addition, calculations were conducted using Theodorsen's ADs to provide a comparison. The iterative calculation procedure implemented by the Matlab-program is described in chapter 2.10.

Initially, the calculations were performed by including the first 40 modes obtained from the FE-models. Further, the combinations of modes included in the analysis were narrowed down, and the resulting changes in critical wind speed estimates revealed which modes that participated in the final instability modes. Both combinations of symmetric and asymmetric modes were tested. Results of the calculations based on these different mode combinations are presented in individual tables 9.1-9.6 for each of the six girders. The final determined critical wind speed estimates are marked in blue. Regarding the notation used, "1-3VS" means the 3 first vertical symmetric modes, and "1VS" means the first vertical symmetric mode.



Table 9.1: Stability calculations 5.5 m

Mode combination	Abaqus mode no.	Critical wind speed $V_{cr}$ [m/s]	
		Fitted ADs	Theodorsen's ADs
1:40	1:40	86.84	98.79
1HS, 1HA, 1-3VA, 1-4VS, 1TS, 1TA	1:4,6,7,11, 23,27:29	83.95	100.82
Symmetric mode combinations			
1-4VS, 1TS	3,7,11,27,29	84.02	100.90
1-3VS, 1TS	3,7,11,27	84.02	100.90
1-2VS, 1TS	3,7,27	85.51	101.3672
1-2VS, 1TS	7,27	97.77	112.29
1VS, 1TS	3,27	116.56	> 150
Asymmetric mode combinations			
1HA, 1-3VA, 1TA	2,4,6,23,28	107.46	125.43
1-3VA, 1TA	2,6,23,28	107.38	125.43
1-2VA, 1TA	2,6,28	107.38	125.43
1VA, 1TA	2,28	107.38	125.43

Table 9.2: Flutter combinations for 5.8 m

Mode combination	Abaqus mode no.	Critical wind speed $V_{cr}$ [m/s]	
		Fitted ADs	Theodorsen's ADs
1:40	1:40	88.55	98.48
1HS, 1HA, 1-3VA, 1-4VS, 1TS, 1TA	1:4,6,7,11, 23,27:29	86.68	100.63
Symmetric mode combinations			
1-4VS, 1TS	3,6,11,27,29	86.76	100.63
1-3VS, 1TS	3,6,11,27	86.84	100.63
1-2VS, 1TS	3,6,27	88.55	100.98
2VS, 1TS	6,27	100.82	111.86
1VS, 1TS	3,27	121.31	> 150
Asymmetric mode combinations			
1HA, 1-3VA, 1TA	2,4,7,23,28	113.09	125.12
1-3VA, 1TA	2,7,23,28	113.09	125.12
1-2VA, 1TA	2,7,28	113.16	125.12
1VA, 1TA	2,28	113.16	125.12

Table 9.3: Flutter combinations for 6.1 m

Mode combination	Abaqus mode no.	Critical wind speed $V_{cr}$ [m/s]	
		Fitted ADs	Theodorsen's ADs
1:40	1:40	88.79	98.24
1HS, 1HA, 1-3VA, 1-4VS, 1TS, 1TA	1:4,6,7,11,24, 27,28,30	87.15	100.47
Symmetric mode combinations			
1-4VS, 1TS	3,6,11,27,30	87.03	100.41
1-3VS, 1TS	3,6,11,27	87.03	100.41
1-2VS, 1TS	3,6,27	88.71	100.66
1VS, 1TS	6,27	100.56	111.62
1VS, 1TS	3,27	119.86	> 150
Asymmetric mode combinations			
1HA, 1-3VA, 1TA	2,4,7,24,28	112.54	124.80
1-3VA, 1TA	2,7,24,28	112.62	124.80
1-2VA, 1TA	2,7,28	112.62	124.80
1VA, 1TA	2,28	112.62	124.80

Table 9.4: Flutter combinations for 6.4 m

Mode combination	Abaqus mode no.	Critical wind speed $V_{cr}$ [m/s]	
		Fitted ADs	Theodorsen's ADs
1:40	1:40	88.40	98.18
1HS, 1HA, 1-3VA, 1-4VS, 1TS, 1TA	1:4,6,7,11,24, 27,28,30	86.05	100.61
Symmetric mode combinations			
1-4VS, 1TS	3,6,11,27,30	85.98	100.57
1-3VS, 1TS	3,6,11,27	85.90	100.57
1-2VS, 1TS	3,6,27	86.84	100.76
1VS, 1TS	6,27	96.60	111.78
1VS, 1TS	3,27	115.34	> 150
Asymmetric mode combinations			
1HA, 1-3VA, 1TA	2,4,7,24,28	105.43	124.86
1-3VA, 1TA	2,7,24,28	105.35	124.86
1-2VA, 1TA	2,7,28	105.35	124.86
1VA, 1TA	2,28	105.35	124.86

Table 9.5: Flutter combinations for 6.7 m

Mode combination	Abaqus mode no.	Critical wind speed $V_{cr}$ [m/s]	
		Fitted ADs	Theodorsen's ADs
1:40	1:40	47.15	98.07
1HS, 1HA, 1-3VA, 1-4VS, 1TS, 1TA	1:4,6,7,11,24, 27,28,30	47.15	100.76
Symmetric mode combinations			
1-4VS, 1TS	3,6,11,27,30	59.35	100.72
1-3VS, 1TS	3,6,11,27	59.35	100.72
1-2VS, 1TS	3,6,27	59.65	100.88
1VS, 1TS	6,27	81.40	111.93
1VS, 1TS	3,27	62.76	> 150
1VS	3	64.85	> 150
Asymmetric mode combinations			
1HA, 1-3VA, 1TA	2,4,7,24,28	47.15	124.75
1-3VA, 1TA	2,7,24,28	47.15	124.75
1-2VA, 1TA	2,7,28	47.15	124.75
1VA, 1TA	2,28	47.15	124.75
1VA	2	48.60	> 150

Table 9.6: Flutter combinations for 7.0 m

Mode combination	Abaqus mode no.	Critical wind speed $V_{cr}$ [m/s]	
		Fitted ADs	Theodorsen's ADs
1:40	1:40	39.84	97.87
1HS, 1HA, 1-3VA, 1-4VS, 1TS, 1TA	1:4,6,7,11,24, 27,28,30	39.85	101.04
Symmetric mode combinations			
1-4VS, 1TS	3,6,11,27,30	53.07	101.00
1-3VS, 1TS	3,6,11,27	53.07	101.00
1-2VS, 1TS	3,6,27	53.07	101.15
1VS, 1TS	6,27	73.93	112.25
1VS, 1TS	3,27	53.07	> 150
1VS	3	53.07	> 150
Asymmetric mode combinations			
1HA, 1-3VA, 1TA	2,4,7,24,28	39.85	124.34
1-3VA, 1TA	2,7,24,28	39.84	124.34
1-2VA, 1TA	2,7,28	39.84	124.34
1VA, 1TA	2,28	39.84	124.34
1VA	2	40.63	> 150

It should be noted that one should be careful when performing calculations considering the combination of all 40 modes, as some of these modes have a high excitation in other structural elements as cables and hangers. As the connection between cables and hangers are modelled as fixed ties, these modes are not likely to represent the true modal behaviour of the bridge. Allowing for rotations in the connections would be more correct.

The resulting estimates show that the four lower girders 5.5, 5.8, 6.1 and 6.4 m all have sufficient critical wind speed, with values of 84.0, 86.8, 87.0 and 85.9 m/s, respectively. This is above the design wind criteria of 76 m/s, with a margin varying between 8 and 11 m/s. The highest critical wind speed is in other words found for the 6.1 m girder, by a hair. The two girders 6.7 and 7.0 m have significantly lower critical wind speed estimates, with values of 48.6 and 40.6 m/s, respectively. They do not pass the design wind criteria.

It is seen that the calculations with Theodorsen's ADs show similar results for the six girders. This was expected, as these ADs vary little, and the modal properties of the six girders have been shown to be relatively equal.

Further, the reduced critical wind speeds from all calculations with polynomial AD-functions are within the interval of obtained data for the experimental ADs: [0.72, 3.64]. This is important for the validity of the estimates. The reduced critical wind speeds and critical frequencies for the final critical velocities are presented in their entirety in table 9.7, below:

Table 9.7: Critical frequency and reduced velocity for the presented critical velocities

Girders:	5.5 m	5.8 m	6.1 m	6.4 m	6.7 m	7.0 m
$V_{red_{CR}}$	1.0739	1.1126	1.1119	1.0809	2.6246	2.2530
$\omega_{CR}$ [rad/s]	2.2160	2.1890	2.1829	2.2009	0.5081	0.4929

It is seen that the critical frequency is significantly lower for the two highest girders than for the four lower girders.

The estimated critical wind speeds are further summarized for the six girders, and compared to the design wind speed criteria, in figure 9.11. The line drawn between the points of the critical wind speed estimates of the six girders is simply a visualization of the development, and is not to be interpreted as a function for the critical wind speed.

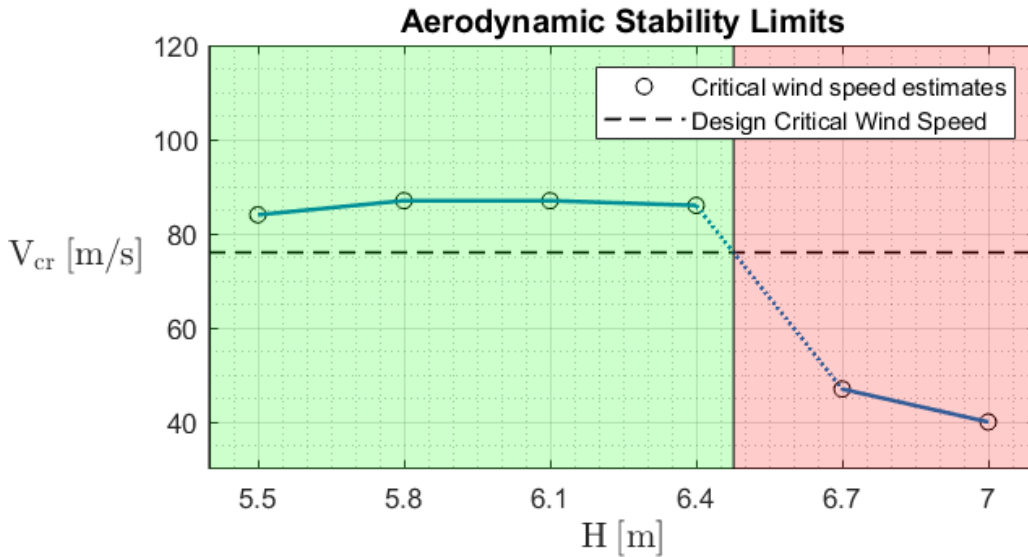


Figure 9.11: Critical wind speed estimates

The estimated critical wind speeds for the 4 lowest girders, 5.5-6.4 m, varies around 3 m/s which is about 3.6%. This variation is notably small, when considering the shape-wise differences of the girders. Girder 6.4 m is 16.4% higher than the lowest girder 5.5 m, and their angles  $\alpha$  below deck are  $19.2^\circ$  and  $31.4^\circ$ , respectively.

The drastic reduction in critical wind speed of girder 6.4 m to girder 6.7 m is also very interesting. The girders are shape-wise similar with a difference in height of 4.9% and their angles below deck are  $19.2^\circ$  and  $17.8^\circ$ , respectively. The large difference in performance of the four lower and the two highest girders is directly connected to the clear distinction between their AD-functions, described in the previous section.

The respective resulting instability modes of the six girders become apparent when considering the mode shapes that contribute to the instability. The resulting instability mode shapes are further visualized with Argand diagrams in figure 9.12. The instability mode represents the girder behaviour at the point of instability.

### Instability Modes

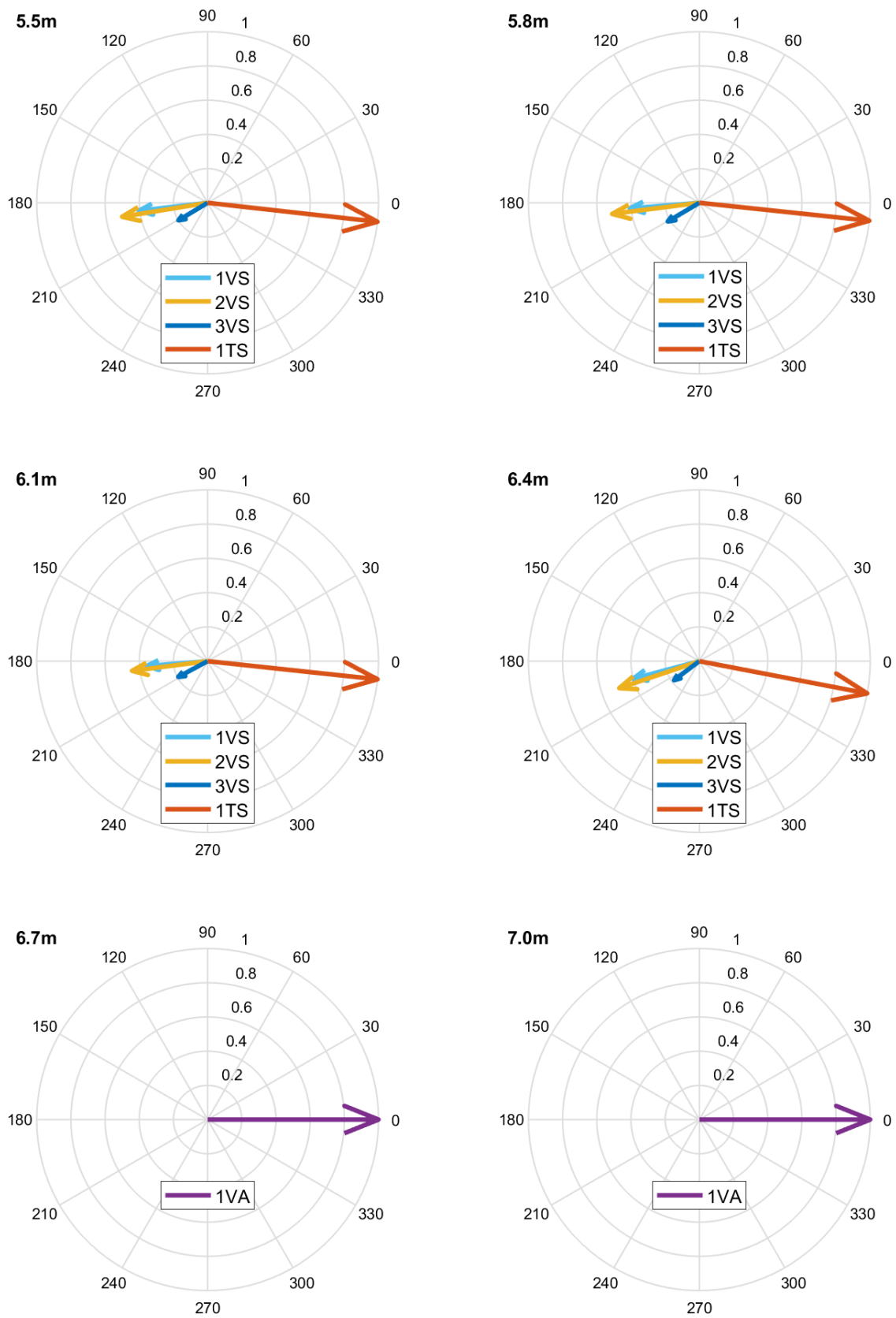


Figure 9.12: Argand diagrams of the instability modes for all six girders

From the Argand diagrams it is seen that the instability modes of the four lowest girders are very similar, all showing a strong influence of the first symmetric torsional mode and the two first symmetric vertical modes. This is the instability phenomenon of flutter. It is also observed that the second vertical symmetric mode has higher participation in the instability mode than the first vertical mode, which is a common trait. The similarity between the instability modes of these girders is in correspondence with the observations their similar AD-functions.

The instability modes of the two highest girders, 6.7 and 7.0 m consist of only one mode, namely the first asymmetric vertical mode, which is the vertical mode with the lowest natural frequency. This corresponds to the instability phenomena known as galloping. As mentioned in the previous section, the resulting ADs of these girders did indicate that galloping could occur. Galloping is known to be a problem related to a full separation of wind flow, i.e. where the flow is not reattached to the surface of the girder after being divided from it.

The distinction between the aerodynamic instability behaviour of the four lowest girders and the two highest is further visualized with a bar diagram in figure 9.13. This diagram displays the mode participation in each of the girder's instability modes. Each girder is indicated with a different color in this plot.

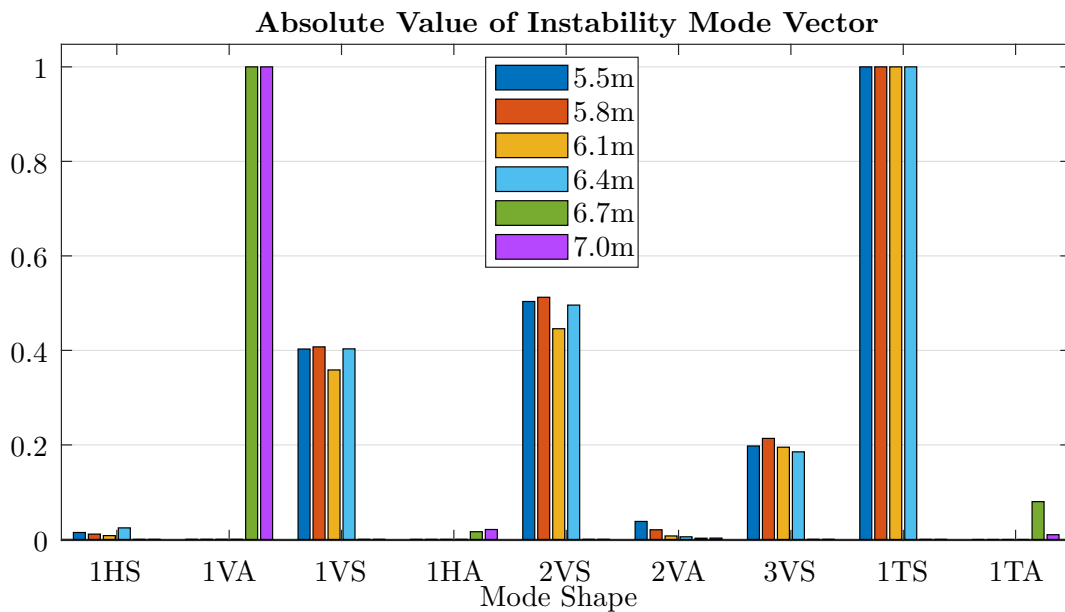


Figure 9.13: Comparison of the instability modes

The two groups of girders with different instability modes is clearly seen here. It is also worth noting that no instability mode has participation of horizontal modes. This is in accordance to presented theory in section 2.5.

More information about the instability behaviours of the six girders is revealed by considering plots of the in-wind frequency and damping of the respective modes that contribute to their instability, as functions of the wind speed. These plots from girder are shown for all girders in figure 9.14.

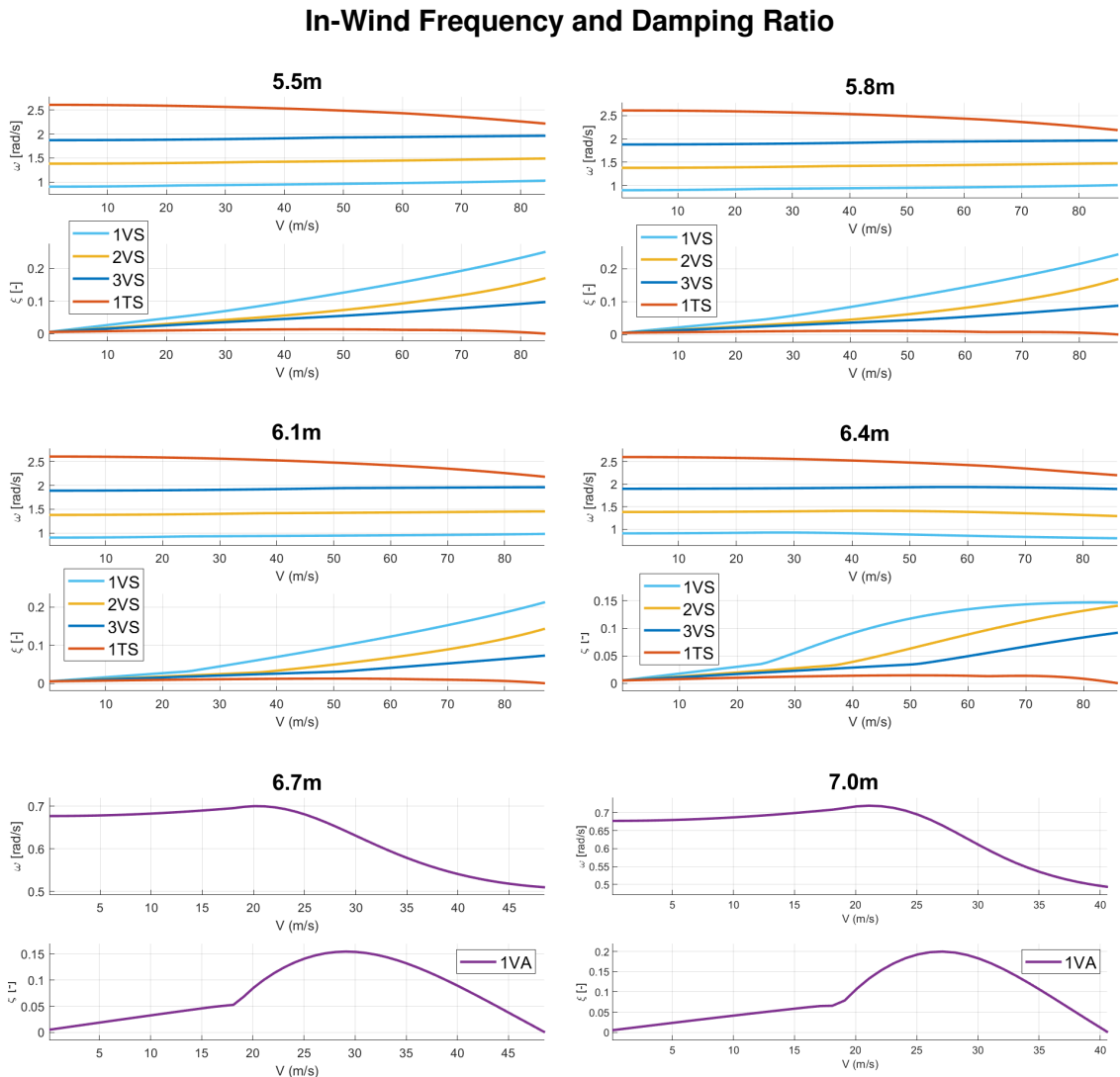


Figure 9.14: In-wind frequency and damping for the instability modes

It is seen that the in-wind frequency and in-wind damping plots are similar for girders for the four lowest and the two highest girders, respectively. In common for all six girders is the loss of stiffness in the driving instability mode with increasing mean-wind velocity. For the four lowest girders, this is the first symmetric torsional mode. This is observed as this is the mode where the damping reaches zero. The linear development of the in-wind frequency seen for lower wind speeds is due to the AD-functions being constant for  $V_{red}$ -values outside of the interval with obtained data points. For girders 5.5-6.1 m, the three symmetric vertical modes have a slight increase of stiffness with increased mean wind velocity. However, for girder 6.4 m the stiffness of the vertical modes decreases. This may indicate the start of the transition of instability behaviour from the lower girders to the highest girders.

As mentioned, uncertainties occur when using wind tunnel testing to estimate the behaviour of a fully sized structure. Additionally, the use of polynomial functions to fit



ADs also introduces uncertainties. In order to investigate the sensitivity of the obtained results, a brief analysis was conducted. The critical wind speeds were re-calculated with ADs scaled to 110%. The majority of the ADs have a destabilizing effect for higher absolute values, but as seen in table 2.1, some ADs have a damping effect with certain higher amplitudes. The results from this analysis is given in table 9.8.







Table 9.8: Brief sensitivity analysis

Girders:	5.5 m	5.8 m	6.1 m	6.4 m	6.7 m	7.0 m
$V_{cr}$ [m/s], with ADs scaled to 110%	79.4	80.8	81.6	82.1	46.0	38.9

These estimates give a brief idea of the sensitivity of the previously presented results. The estimates show that the four girders 5.5, 5.8, 6.1 and 6.4 m still pass the design criteria of 76 m/s.

The final critical wind speed estimates, which were highlighted in tables 9.1-9.6, are summarized and presented with the respective girder shapes in figure in table 9.9.

Table 9.9: Critical wind speeds estimates for the six selected girders

H [m]	Girder Shape	$V_{cr}$ [m/s]
5.5		84.0
5.8		86.8
6.1		87.0
6.4		85.9
6.7		48.6
7.0		40.6

## 9.4 Discussion of Results

As mentioned throughout this chapter, a number of uncertainties are involved in the obtained critical wind speed estimates. The major uncertainties are in relation to the scaling of the wind tunnel test results from the section model to the full scale bridge, and the fitting of the AD-functions from the AD data points. The acquired wind tunnel test data themselves is regarded to be of high quality. Also, the modal properties from the element models are considered to have a low degree of uncertainty.

Regarding the data fitting performed for the AD-functions, a sensitivity analysis was conducted where they were scaled up to 110 %. The resulting critical wind speed estimates were still within the design wind criteria of 76 m/s, which is reassuring. The uncertainty related to the scaling of wind tunnel test results is larger for the girders showing Reynolds number dependency. This was particularly seen for the three girders of height 6.4, 6.7 and 7.0 m, in the static coefficient plots and the resulting data scatter of the AD data points. Therefore, their critical wind speed estimates are considered to have slightly more uncertainty than the estimates of the three lower girders. Regardless, girder 6.7 and 7.0 m do not have sufficient stability, but it is worth noting that the estimate for girder 6.4 m therefore has more uncertainty than girders 5.5-6.1 m. However, all in all, the critical wind speed estimations are considered to be reliable.

There is a noticeable difference between the critical wind speed estimates of this thesis and those from the analysis conducted by Dr. techn. Olav Olsen. The latter estimate was based on the ADs of the girder of Julsundet, shown in figure 4.4, and was equal to the design criteria of 76 m/s, while the estimates of the four lower girders in this thesis are in the range 84-87 m/s. This difference is surprising, knowing that the girder of height 5.5 m is very similar to the the girder design proposed in Olav Olsen's report, and the girder of Julsundet has a more streamlined shape than the girders of this thesis. The modal properties should also be quite similar. Two differences are the change of span from 1235 m in Olav Olsen's model to 1220 m in this thesis, and the change of St. Venant torsional stiffness constant from 31 to 28.5 m<sup>4</sup>. The difference in results should therefore be due to the ADs. However, it is hard to compare girder shapes to each other visually. The answer may be found by executing stability calculations with the ADs.

Since the results showed that the critical wind speeds obtained are within the design criteria by a relatively large margin, it may indicate that the constraint value for the torsional stiffness is unnecessarily high. Hence, a girder using less material may be feasible. The aluminium girder for Langenuen could therefore probably be further optimized.

# Chapter 10

## Conclusion

By selecting a parametric girder shape and constraining the torsional stiffness to be constant, the resulting modal properties also remained relatively unchanged. Therefore, the effect of the aerodynamics of the girders are roughly isolated in the aerodynamic stability calculations. In addition, the material usage of the selected girders is relatively similar, which is recognized as an important factor for the cost, and hence the relevancy of the girders.

The results show that the four girders of height 5.5, 5.8, 6.1 and 5.4 m all have sufficient stability, compared to the design wind speed criteria of 76 m/s. Their critical wind speeds were estimated to be 84.0, 86.8, 87.0 and 85.9 m/s, respectively. The two girders of height 6.7 and 7.0 m did not have a sufficient stability limits however, with critical wind speeds of 48.6 and 40.6 m/s. The instability phenomena occurring for the four lowest girders is flutter, while it is galloping for the two highest girders. The transition from flutter to galloping likely occurs because of a full separation of flow for the two highest girders.

The acquired wind tunnel test data is considered to be of high quality. However, indication of Reynold number dependency is observed for the three highest girders, 6.4, 6.7 and 7.0 m, which introduces some uncertainty in their critical wind speed estimates. All in all, the obtained critical wind speed results are considered to be reliable.

During the wind tunnel tests, vortex shedding induced vibrations were observed to be more prevalent for the 5.5 m and 5.8 m girders than for the 6.1 m and 6.4 m girders. Further, seeing that the estimate of girder 6.4 m is related to more uncertainty than 6.1 m, the girder of height 6.1 m may be the overall preferable alternative.

## 10.1 Further work

During the authors work with this thesis, there has been identified a number of subjects that would be interesting to conduct further work on. Some of these would add to, and some would build on, the findings in this thesis.

- Conduct critical wind speed calculations on the girders of this thesis with the ADs from Julsundet. This will provide further information about the effect of the ADs acquired in this thesis vs. the ADs of Julsundet.
- Investigate the stability of girders with lower stiffness. Since four girders pass the stability criteria with a large margin, the torsional stiffness constraint, and hence material usage of the girders, may be unnecessarily high. The stability of girders with lower stiffness can be investigated with calculations based on the ADs acquired in this thesis. The new girders could be selected with the procedure as presented in chapter 5, but with a lower constraint for the torsional stiffness.
- Perform wind tunnel tests with wind flow from the opposite direction. The fence configuration is not symmetric, which could result in different performance with regards to the wind direction. Wind studies on the Langenuen fjord crossing initiated by NPRA show that the wind is significant in both directions [5].
- Investigate vortex shedding induced response in greater detail. The wind tunnel tests revealed different sensitivity to vortex shedding between the six girders. Girders of interest can be investigated further with dedicated wind tunnel tests, that also examine the effect of guide vanes.
- Investigate the uncertainty of the critical wind speed estimates. By performing Monte Carlo simulations with safety margins for the attained modal properties and the attained functions for aerodynamic derivatives, one can determine the reliability of the critical wind speed estimates. Such investigations has been performed on the Hardanger Bridge[25].
- Conduct static and dynamic response analyses for girders of interest, in order to obtain how the girders behave under serviceability wind velocity.
- Perform additional wind tunnel tests on the girders 6.4 and 6.7m. As these are subjected to two different instability phenomena, it would be interesting to further investigate the flow pattern around these section models.
- Research the stability of different girder shapes than those presented in this thesis. The method of selecting girder shapes described in chapter 5 could be used, but with a different parametrization, in order to investigate the effect of another interesting geometrical variation. New section models would have to be made, and new wind tunnel tests performed. One could for instance implement a parametrization which considers different heights of the side edge points of the girder, like the shapes of Osman Gazi and Hålogaland (see chapter 3.2), or where the width of the girder is primarily varied, rather than the height.
- Investigate the aerodynamic effect of using a stabilizer plate on the top of the girder. Studies conducted on the Runyang and Xihoumen suspension bridges in China indicate that a stabilizer plate located at the middle of the bridge cross section could lead to an increase in the critical wind speed[18]. This could be interesting to examine by performing wind tunnel tests with a selected girder shape.

# Bibliography

## Books

- [8] K. Bell. *An engineering approach to Finite Element Analysis of linear structural mechanics problems*. Fagbokforlaget, 2014.
- [9] K. Bell. *Konstruksjonsmekanikk - Del 2: Fasthetslære*. 1. utgave. Fagbokforlaget, 2015.
- [14] C. Dyrbye and S. O. Hansen. *Wind Loads on Structures*. John Wiley & Sons, 1997.
- [17] F. Gazzola. *Mathematical Models for Suspension Bridges. Nonlinear Structural Instability*. Springer, 2015.
- [19] N. J. Gimsing and C. T. Georgakis. *Cable Supported Bridges - Concept and Design*. Third. Springer, 2012.
- [23] P. K. Larsen. *Dimensjonering av stålkonstruksjoner*. 2. Fagbokforlaget, 2015.
- [32] A. Selberg. *Oscillation and aerodynamic stability of suspension bridges*. Civil Engineering and Building Construction Series. No. 13. Acta Polytechnica Scandinavia, 1961.
- [40] E. Strømmen. *Theory of Bridge Aerodynamics*. Second edition. Springer, 2010.

## Papers

- [1] Horg Aas. “Wind Tunnel Testing of Bridge Decks”. In: (2016).
- [7] O. Øiseth B. Siedziako and A. Rønnquist. “An enhanced forced vibration rig for wind tunnel testing of bridge deck section models in arbitrary motion”. In: (2017).
- [11] F. Brancaleoni. “Concepts and new perspectives for long span bridges”. In: (2016).
- [13] Magnus Aa Dalen. “Aerodynamic Stability of Long-span Suspension Bridges”. In: (2016).
- [16] C. J. Apelt G. S. West. “The effects of tunnel blockage and aspect ratio”. In: 361-377 114 (1982).
- [18] Y.J. Ge and H.F. Xiang. “Aerodynamic stabilization for box-girder suspension bridges with super-long span”. In: *Elsevier Ltd* (2009).
- [20] Gjelden. “Parametric modelling of Langenuen suspension bridge”. In: (2019).
- [25] A. Rønnquist O. Øiseth and Arvid Naess. “System reliability of suspension bridges considering static divergence and flutter”. In: (2015).
- [26] R. Sigbjørnsson O. Øiseth. “An alternative analytical approach to prediction of flutter stability limits of cable supported bridges”. In: (2011).
- [33] Necati Catbas Selcuk Bas Nurdan M. Apaydin. “Considerations for Finite Element Modeling of the Bosphorus Suspension Bridge”. In: (2016).

- [34] B. Siedziako and O. Øiseth. “On the importance of cross-sectional details in the wind tunnel testing of bridge deck section models”. In: (2017).
- [41] T. Theodorsen. “General theory of aerodynamic instability and the mechanism of flutter”. In: (1935).
- [43] S. Trein. “Coupled flutter stability from the unsteady pressure characteristics”. In: 114-122 (2011).
- [45] F.Y. Xu et al. “Higher-order Self-Excited Drag Forces on Bridge Decks”. In: 142 (2016).

## Reports

- [2] Norwegian Public Roads Administration. *Long span bridges in Norway, including future crossing of the Oslo Fjord*. Sept. 2014.
- [5] Norwegian Roads Public Administration. *MetOcean specification Langenuen report*. 2020.
- [6] Norconsult AS. *E39 Stord - Tysnes: Bru over Langenuen og Søreidsvika, Skisseprosjekt*. Mar. 2015.
- [21] Hydro. *Aluminium, environment and society*. 2012.
- [27] Dr. techn. Olav Olsen. *Suspension bridge over Langenuen - Aluminum girder alternative*. Sept. 2019.

## Manuals

- [10] K. Bell, O. V. Bleie, and L. Wollebæk. *CrossX - User's Manual*. Version 1.1. A Windows-based program for computation of parameters for, and stress distribution on, arbitrary beam cross sections. Department of structural engineering, NTNU. 2003.
- [35] Simulia. *Abaqus Scripting Reference Guide*. Version 6.14. 2014.
- [36] Simulia. *Abaqus Theory Guide*. Version 6.14. 2014.

## Websites

- [3] Norwegian Roads Public Administration. *Aluminum Bridge over Langenuen*. 2020. URL: <https://www.vegvesen.no/vegprosjekter/ferjefriE39/nyhetsarkiv/aluminiumbru-over-langenuen-kan-bli-en-realitet>.
- [4] Norwegian Roads Public Administration. *E39 Stord-Os*. 2020. URL: <https://www.vegvesen.no/Europaveg/e39stordos>.
- [24] NRK. *Fryktar aluminiumsanlegget blir stengt og aldri opna igjen*. 2020. URL: <https://www.nrk.no/vestland/hydro-gjer-det-dei-kan-for-a-halde-hjula-i-gang-1.14961523>.
- [30] Reuters. *Coronavirus-wrecked demand pushes aluminium to 4-year low*. 2020. URL: <https://www.reuters.com/article/global-metals/metals-coronavirus-wrecked-demand-pushes-aluminium-to-4-year-low-idUSL4N2BW24Y>.
- [37] Simulia/MIT. Version 6.17. 2017. URL: <https://abaqus-docs.mit.edu/2017/English/SIMACAETHERefMap/simathe-c-meshedsections.htm>.

- [38] Simulia/MIT. *\*BEAM ADDED INERTIA*. Version 6.17. URL: <https://abaqus-docs.mit.edu/2017/English/SIMACAEKEYRefMap/simakey-r-beamaddedinertia.htm>.
- [44] Wikipedia. *List of Longest Suspension Bridge Spans*. 2020. URL: [https://en.wikipedia.org/wiki/List\\_of\\_longest\\_suspension\\_bridge\\_spans](https://en.wikipedia.org/wiki/List_of_longest_suspension_bridge_spans).

## Images

- [12] Judy Breck. *Tacoma Narrows Bridge Collapse*. <https://flickr.com>. Feb. 2008.
- [15] Rick Franks. *Akashi Kaikyo Bridge*. <https://flickr.com>. Mar. 2017.
- [22] kronja. *hardangerbrua*. <https://flickr.com>. July 2014.
- [28] NY Photographer. *Brooklyn Bridge*. <https://flickr.com>. June 2016.
- [29] Lars Pirtzel. *Storebælt*. <https://flickr.com>. Sept. 2016.
- [31] brother rubber. *Menai Bridge*. <https://flickr.com>. Aug. 2012.
- [39] Ryan Stavely. *Tacoma Narrows (2)*. <https://flickr.com>. Apr. 2010.
- [42] TinaL100. *Williamsburg Bridge*. <https://flickr.com>. Jan. 2012.



# Appendices

# Appendix A

## List of Electronic Attachments

### Dynamo:

- *ParametricGirderShape.dyn* - Generating the parametric girder (Input: H and  $\theta$ ).
- *ConstantTorsionalStiffness.dyn* Parametric girder with constant torsional stiffness (Input: H).
- *Bredts2Formula.dyn* - Parametric girder shape with constant torsional stiffness, with a correct implementation of Bredts 2. formula.
- *GeometricProperties.dyn* - Parametric girder with constant torsional stiffness, and calculation of the geometrical properties presented in table 5.1.
- *CrossX\_ExactGirderSketch.dyn* - The exact girder geometry for the CrossX calculations. Generates a .TXT-file that can be uploaded to CrossX. (Input: H)
- *CrossX\_BulkheadGeometry.dyn* - Output: the coordinates of the seven corner points of the bulkeheads in the girders. (Input: H)

### Matlab:

- *TorsionalStiffnessGrid.m* - Torsion constant surface plot, extracting function for constant torsional stiffness and selecting girder shapes.
- *TorsionalStiffnessConstant.m* - Torsional stiffness constant function for the parametric girder (Input: H,  $\theta$  and  $t_{ef}$ ).

### Python:

- *ElementModel\_5\_5m, ..., ElementModel\_7\_0m* - Python scripts generating the Abaqus global element models.

## Appendix B

# Girder Shape Drawings

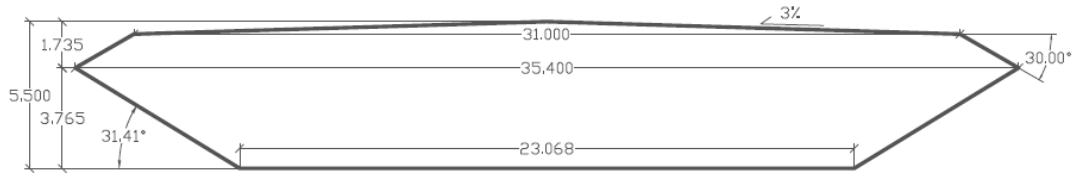


Figure B.1: Girder shape of height 5.5 m

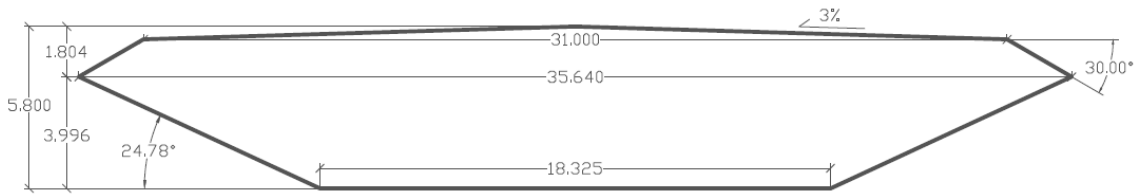


Figure B.2: Girder shape of height 5.8 m

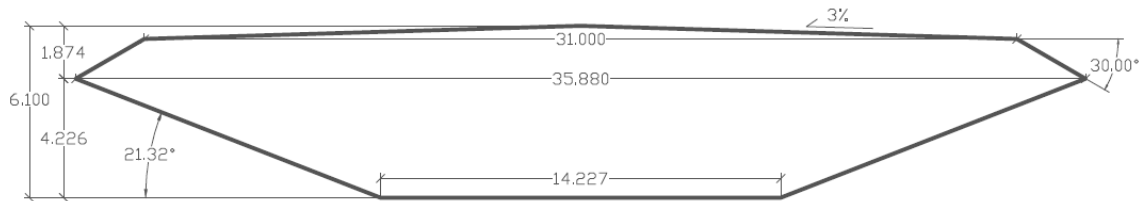


Figure B.3: Girder shape of height 6.1 m

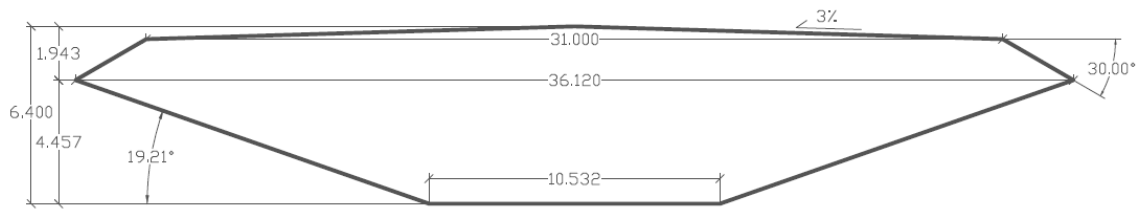


Figure B.4: Girder shape of height 6.4 m

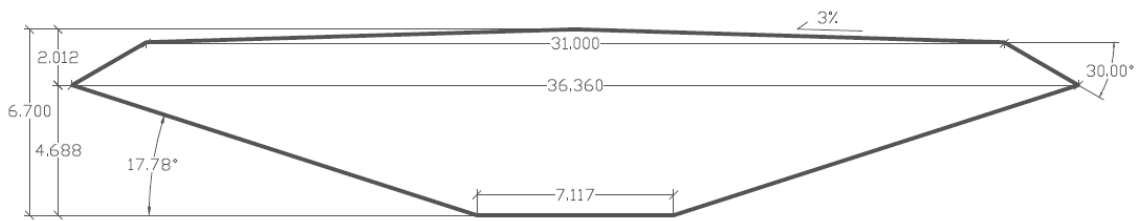


Figure B.5: Girder shape of height 6.7 m

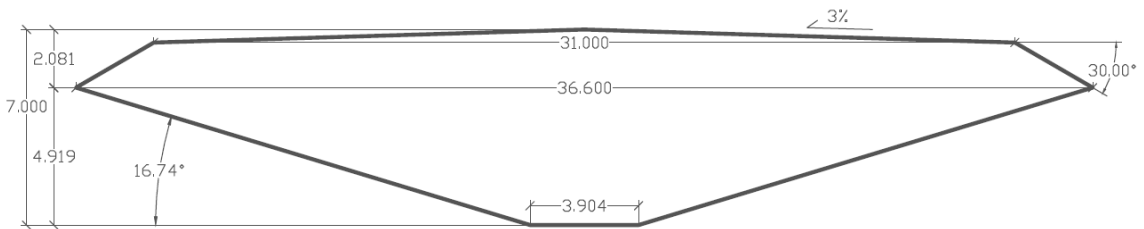


Figure B.6: Girder shape of height 7.0 m

## Appendix C

# Girder Inertia Properties

Table C.1: Girder inertia properties that vary between the six girders

Varying property	Girder height H [m]					
	5.5	5.8	6.1	6.4	6.7	7.0
Linear mass [kg/m]						
Girder	6718	6727	6751	6779	6808	6844
Eccentricity [m]						
Asphalt $e_z$	2.024	2.026	2.034	2.043	2.051	2.058
Hanger head $e_z$	1.792	1.794	1.802	1.811	1.819	1.826
Rotational inertia [kgm <sup>2</sup> /m]						
Girder $I_{11}$	$3.231 \cdot 10^4$	$3.347 \cdot 10^4$	$3.460 \cdot 10^4$	$3.550 \cdot 10^4$	$3.618 \cdot 10^4$	$3.656 \cdot 10^4$
Girder $I_{22}$	$6.641 \cdot 10^5$	$6.650 \cdot 10^5$	$6.710 \cdot 10^5$	$6.789 \cdot 10^5$	$6.876 \cdot 10^5$	$6.983 \cdot 10^5$
Bulkhead $I_{11}$	$1.786 \cdot 10^3$	$1.955 \cdot 10^3$	$2.105 \cdot 10^3$	$2.237 \cdot 10^3$	$2.334 \cdot 10^3$	$2.376 \cdot 10^3$
Bulkhead $I_{22}$	$6.780 \cdot 10^4$	$6.409 \cdot 10^4$	$6.176 \cdot 10^4$	$6.065 \cdot 10^4$	$6.038 \cdot 10^4$	$6.073 \cdot 10^4$
Total girder inertia [kgm <sup>2</sup> /m]						
Horizontal	$9.639 \cdot 10^5$	$9.611 \cdot 10^5$	$9.647 \cdot 10^5$	$9.715 \cdot 10^5$	$9.799 \cdot 10^5$	$9.910 \cdot 10^5$
Vertical	$5.450 \cdot 10^4$	$5.588 \cdot 10^4$	$5.731 \cdot 10^4$	$5.852 \cdot 10^4$	$5.946 \cdot 10^4$	$6.003 \cdot 10^4$
Torsional	$1.018 \cdot 10^6$	$1.017 \cdot 10^6$	$1.022 \cdot 10^6$	$1.030 \cdot 10^6$	$1.039 \cdot 10^6$	$1.051 \cdot 10^6$

## Appendix D

# Modal Properties

Table D.1: Modal properties 5.5 m

Mode	Abaqus no.	Generalized mass $\tilde{M}_i$ [kg]	Frequency [Hz]	Displacement Plot		
				Horizontal	Vertical	Torsion
1HS	1	$1.103 \cdot 10^7$	0.057			
1VA	2	$1.195 \cdot 10^7$	0.107			
1VS	3	$6.262 \cdot 10^6$	0.143			
1HA	4	$1.024 \cdot 10^7$	0.156			
2VA	6	$1.063 \cdot 10^7$	0.219			
2VS	7	$1.012 \cdot 10^7$	0.220			
3VS	11	$9.845 \cdot 10^6$	0.298			
2HS	13	$5.414 \cdot 10^6$	0.310			
3VA	23	$1.155 \cdot 10^7$	0.377			
3HS	26	$5.303 \cdot 10^6$	0.395			
1TS	27	$5.198 \cdot 10^6$	0.415			
1TA	28	$6.692 \cdot 10^6$	0.456			
4VS	29	$1.112 \cdot 10^7$	0.475			
4VA	37	$1.143 \cdot 10^7$	0.583			
2HA	38	$9.529 \cdot 10^6$	0.612			

Table D.2: Modal properties 5.8 m

Mode	Abaqus no.	Generalized mass $\tilde{M}_i$ [kg]	Frequency [Hz]	Displacement Plot		
				Horizontal	Vertical	Torsion
1HS	1	$1.103 \cdot 10^7$	0.057			
1VA	2	$1.196 \cdot 10^7$	0.107			
1VS	3	$6.260 \cdot 10^6$	0.144			
1HA	4	$1.025 \cdot 10^7$	0.156			
2VS	6	$1.022 \cdot 10^6$	0.220			
2VA	7	$1.108 \cdot 10^7$	0.220			
3VS	11	$9.888 \cdot 10^6$	0.299			
2HS	13	$5.416 \cdot 10^6$	0.310			
3VA	23	$1.156 \cdot 10^7$	0.381			
3HS	26	$5.298 \cdot 10^6$	0.395			
1TS	27	$5.194 \cdot 10^6$	0.415			
1TA	28	$6.691 \cdot 10^6$	0.457			
4VS	29	$1.114 \cdot 10^7$	0.479			
4VA	37	$1.144 \cdot 10^7$	0.589			
2HA	38	$9.533 \cdot 10^6$	0.612			



Table D.3: Modal properties 6.1 m

Mode	Abaqus no.	Generalized mass $\tilde{M}_i$ [kg]	Frequency [Hz]	Displacement Plot		
				Horizontal	Vertical	Torsion
1HS	1	$1.103 \cdot 10^7$	0.057			
1VA	2	$1.198 \cdot 10^7$	0.108			
1VS	3	$6.263 \cdot 10^6$	0.144			
1HA	4	$1.028 \cdot 10^7$	0.157			
2VS	6	$1.030 \cdot 10^7$	0.220			
2VA	7	$1.142 \cdot 10^7$	0.221			
3VS	11	$9.935 \cdot 10^6$	0.301			
2HS	13	$5.373 \cdot 10^6$	0.311			
3VA	24	$1.143 \cdot 10^7$	0.383			
3HS	26	$5.342 \cdot 10^6$	0.396			
1TS	27	$5.219 \cdot 10^6$	0.415			
1TA	28	$6.703 \cdot 10^6$	0.457			
4VS	30	$1.119 \cdot 10^7$	0.483			
4VA	37	$1.147 \cdot 10^7$	0.594			
2HA	38	$9.505 \cdot 10^6$	0.613			

Table D.4: Modal properties 6.4 m

Mode	Abaqus no.	Generalized mass $\tilde{M}_i$ [kg]	Frequency [Hz]	Displacement Plot		
				Horizontal	Vertical	Torsion
1HS	1	$1.103 \cdot 10^7$	0.057			
1VA	2	$1.200 \cdot 10^7$	0.108			
1VS	3	$6.266 \cdot 10^6$	0.144			
1HA	4	$1.033 \cdot 10^7$	0.157			
2VS	6	$1.038 \cdot 10^7$	0.220			
2VA	7	$1.151 \cdot 10^7$	0.222			
3VS	11	$9.979 \cdot 10^6$	0.303			
2HS	13	$5.312 \cdot 10^6$	0.312			
3VA	24	$1.161 \cdot 10^7$	0.385			
3HS	26	$5.412 \cdot 10^6$	0.396			
1TS	27	$5.261 \cdot 10^6$	0.415			
1TA	28	$6.720 \cdot 10^6$	0.457			
4VS	30	$1.123 \cdot 10^7$	0.486			
4VA	37	$1.149 \cdot 10^7$	0.599			
2HA	38	$9.467 \cdot 10^6$	0.616			

Table D.5: Modal properties 6.7 m

Mode	Abaqus no.	Generalized mass $\tilde{M}_i$ [kg]	Frequency [Hz]	Displacement Plot		
				Horizontal	Vertical	Torsion
1HS	1	$1.103 \cdot 10^7$	0.057			
1VA	2	$1.202 \cdot 10^7$	0.108			
1VS	3	$6.271 \cdot 10^6$	0.144			
1HA	4	$1.037 \cdot 10^7$	0.157			
2VS	6	$1.044 \cdot 10^7$	0.220			
2VA	7	$1.158 \cdot 10^7$	0.223			
3VS	11	$1.002 \cdot 10^7$	0.303			
2HS	13	$5.245 \cdot 10^6$	0.313			
3VA	24	$1.162 \cdot 10^7$	0.387			
3HS	26	$5.501 \cdot 10^6$	0.397			
1TS	27	$5.316 \cdot 10^6$	0.414			
1TA	28	$6.739 \cdot 10^6$	0.456			
4VS	30	$1.134 \cdot 10^7$	0.489			
4VA	37	$1.151 \cdot 10^7$	0.602			
2HA	38	$9.432 \cdot 10^6$	0.618			

Table D.6: Modal properties 7.0 m

Mode	Abaqus no.	Generalized mass $\tilde{M}_i$ [kg]	Frequency [Hz]	Displacement Plot		
				Horizontal	Vertical	Torsion
1HS	1	$1.103 \cdot 10^7$	0.057			
1VA	2	$1.204 \cdot 10^7$	0.108			
1VS	3	$6.280 \cdot 10^6$	0.145			
1HA	4	$1.043 \cdot 10^7$	0.158			
2VS	6	$1.053 \cdot 10^7$	0.220			
2VA	7	$1.162 \cdot 10^7$	0.223			
3VS	11	$1.005 \cdot 10^7$	0.304			
2HS	13	$5.164 \cdot 10^6$	0.314			
3VA	24	$1.164 \cdot 10^7$	0.388			
3HS	26	$5.632 \cdot 10^6$	0.398			
1TS	27	$5.403 \cdot 10^6$	0.413			
1TA	28	$6.759 \cdot 10^6$	0.454			
4VS	30	$1.158 \cdot 10^7$	0.490			
4VA	37	$1.153 \cdot 10^7$	0.603			
2HA	38	$9.399 \cdot 10^6$	0.621			

## Appendix E

# Aerodynamic Derivatives

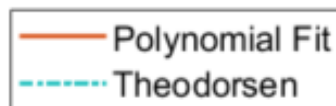


Figure E.1: The legend used for the AD-plots

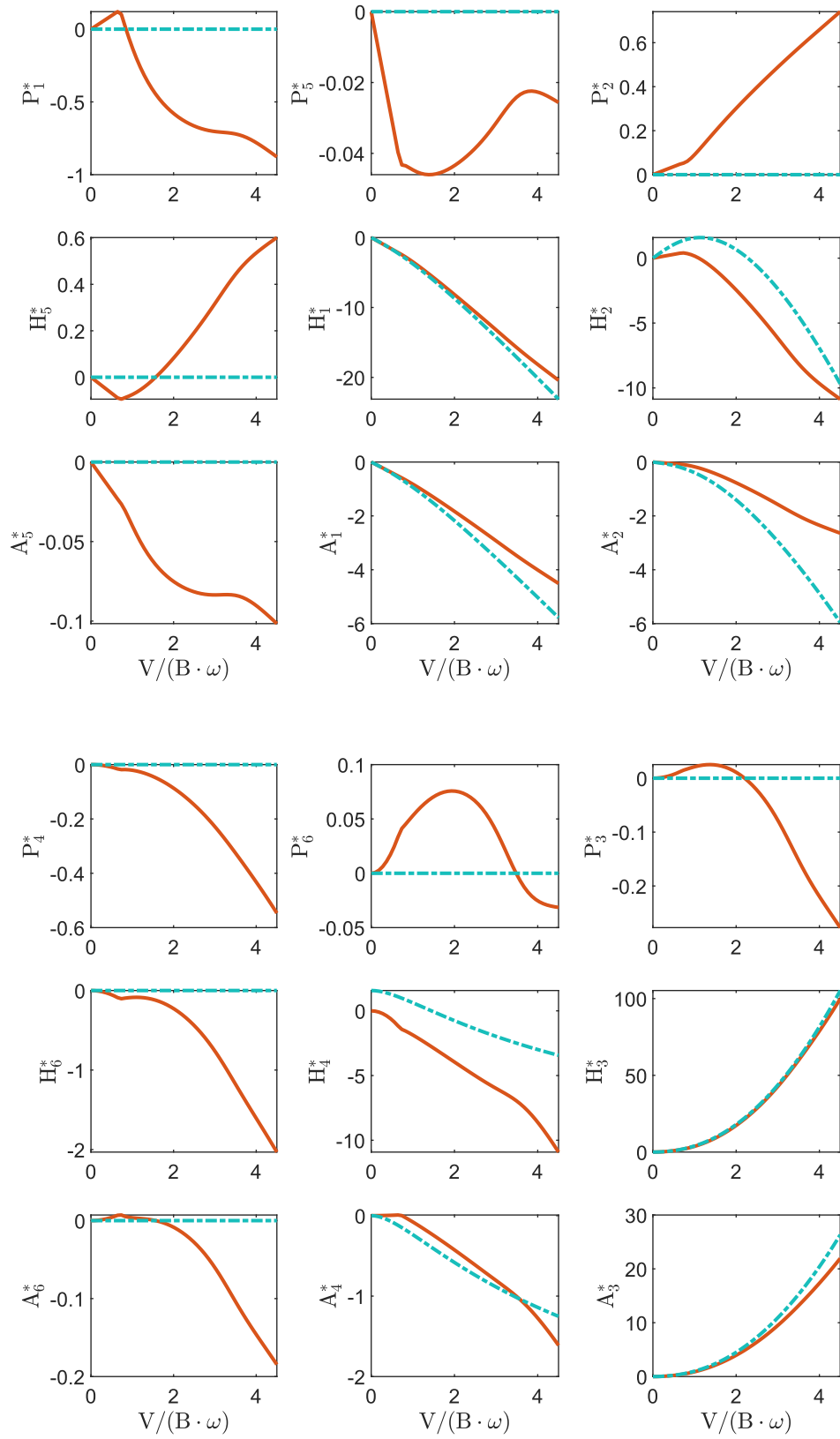


Figure E.2: ADs for 5.5 m

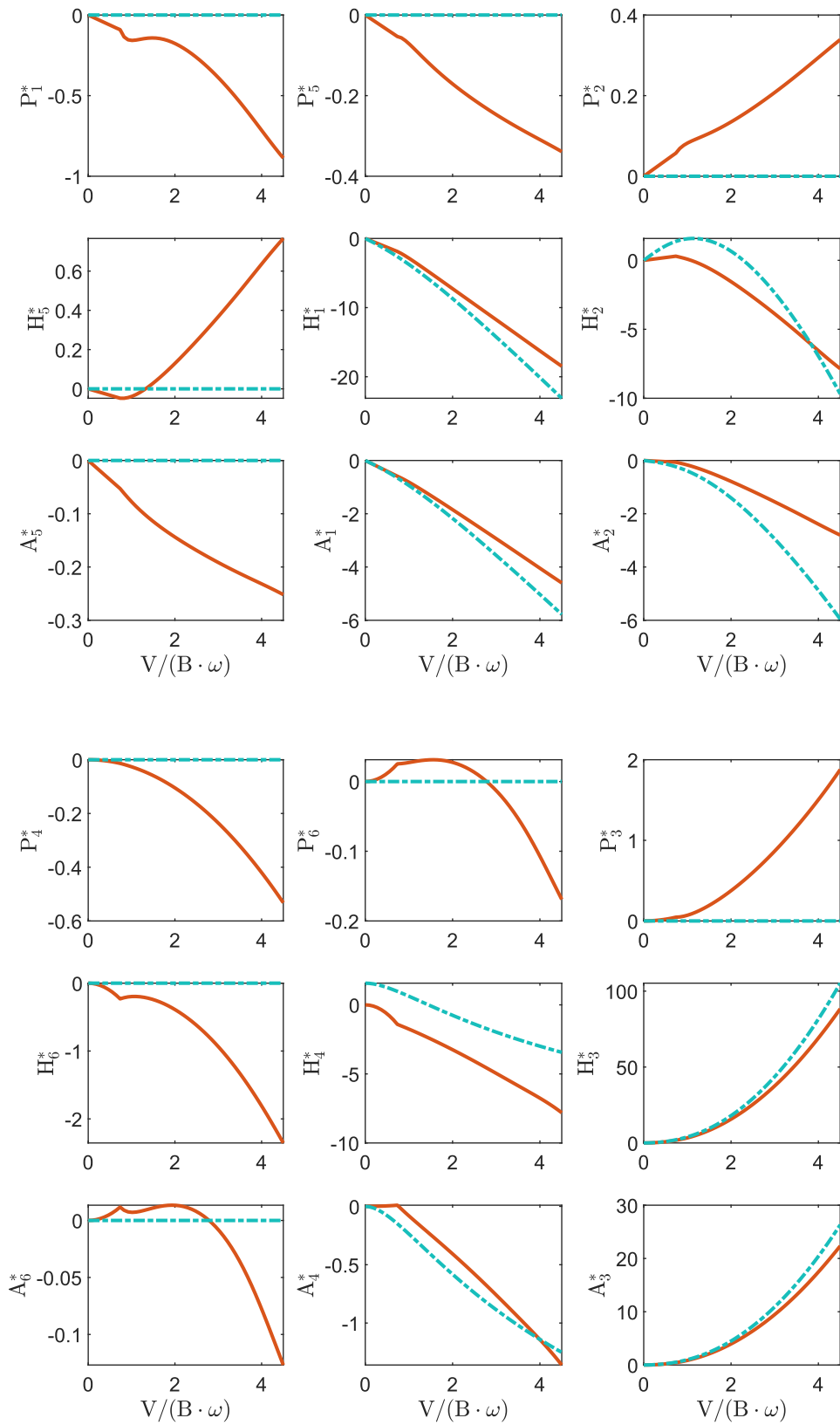


Figure E.3: ADs for 5.8 m

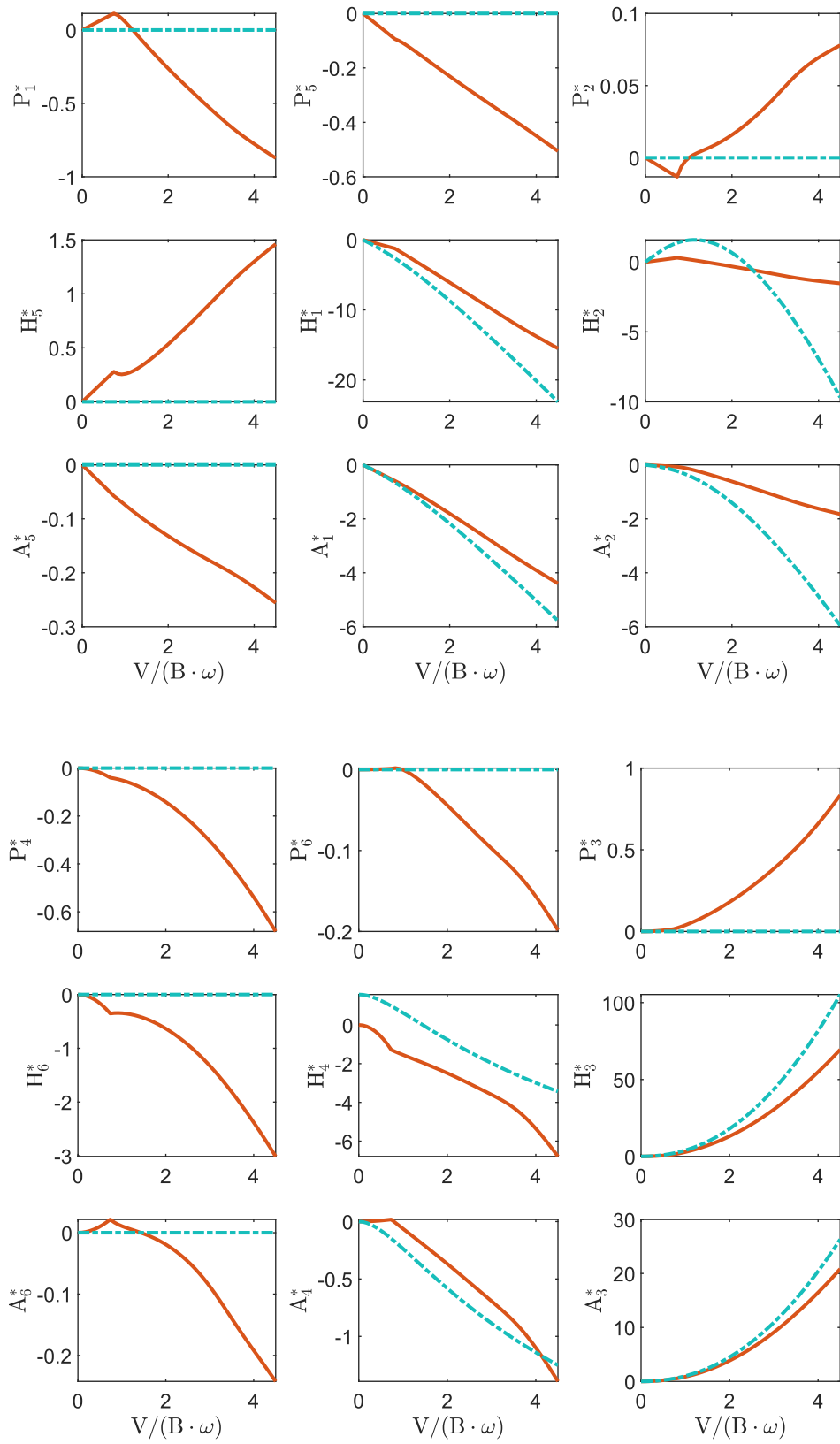


Figure E.4: ADs for 6.1 m

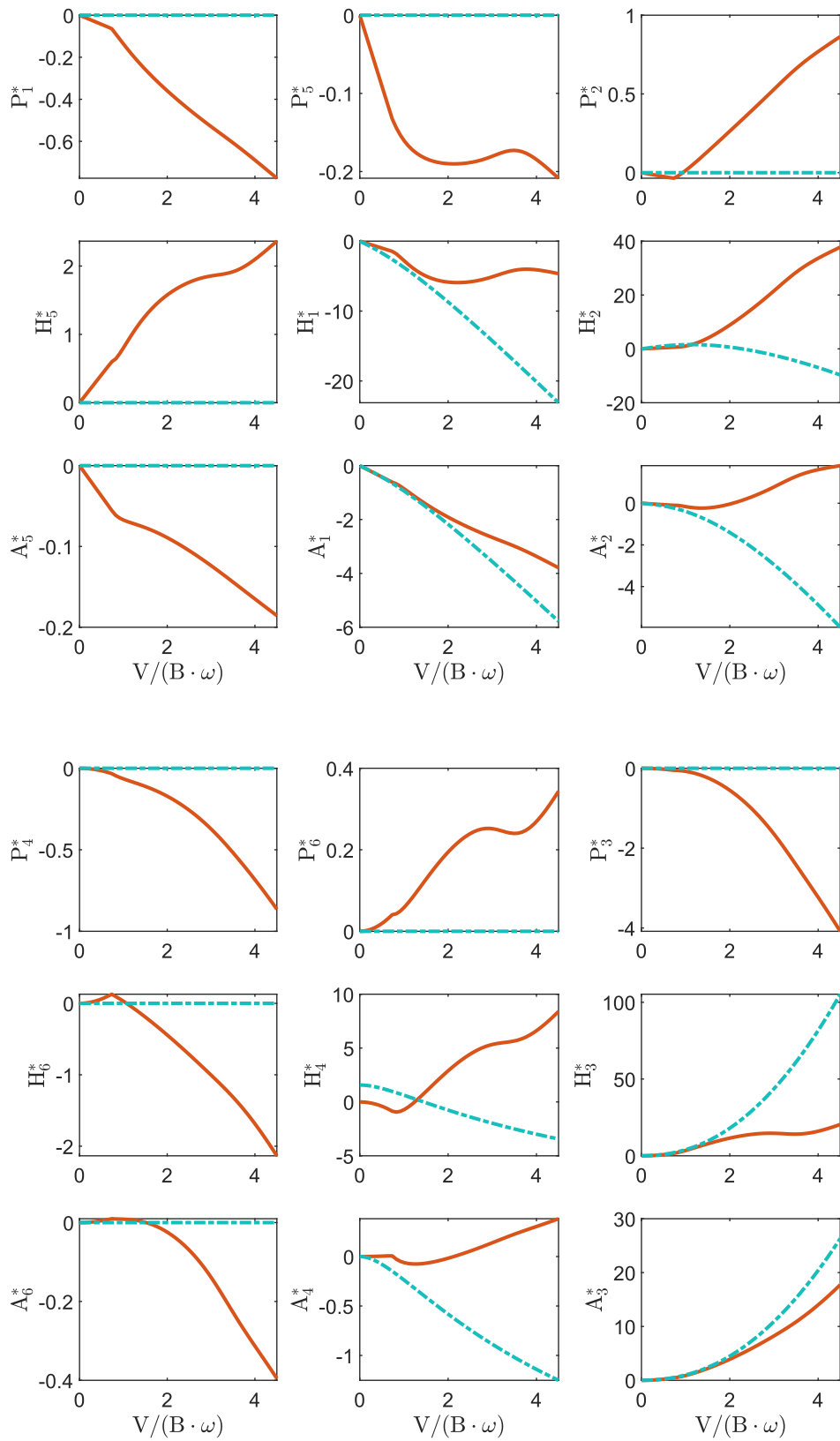


Figure E.5: ADs for 6.4 m

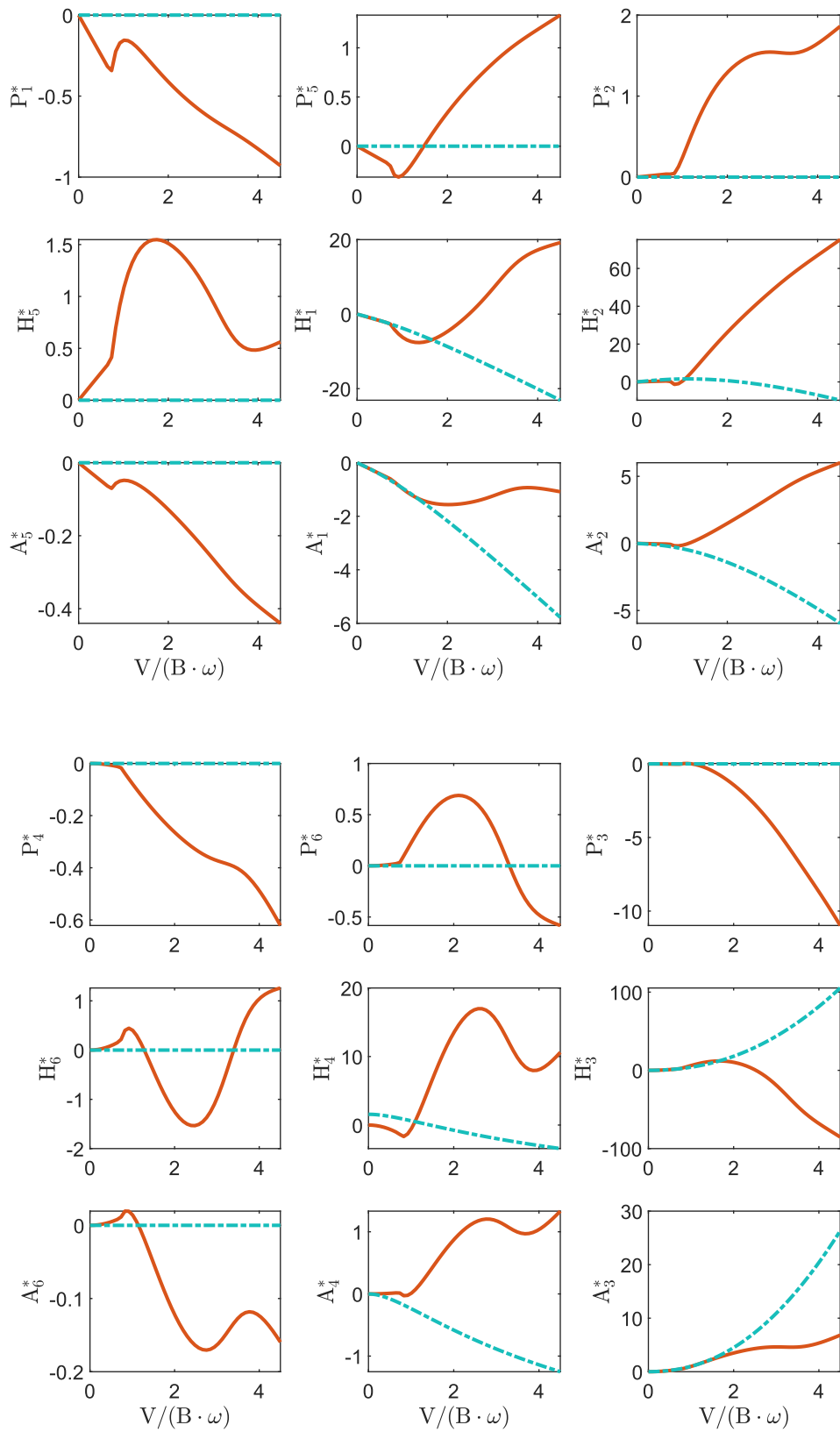


Figure E.6: ADs for 6.7 m



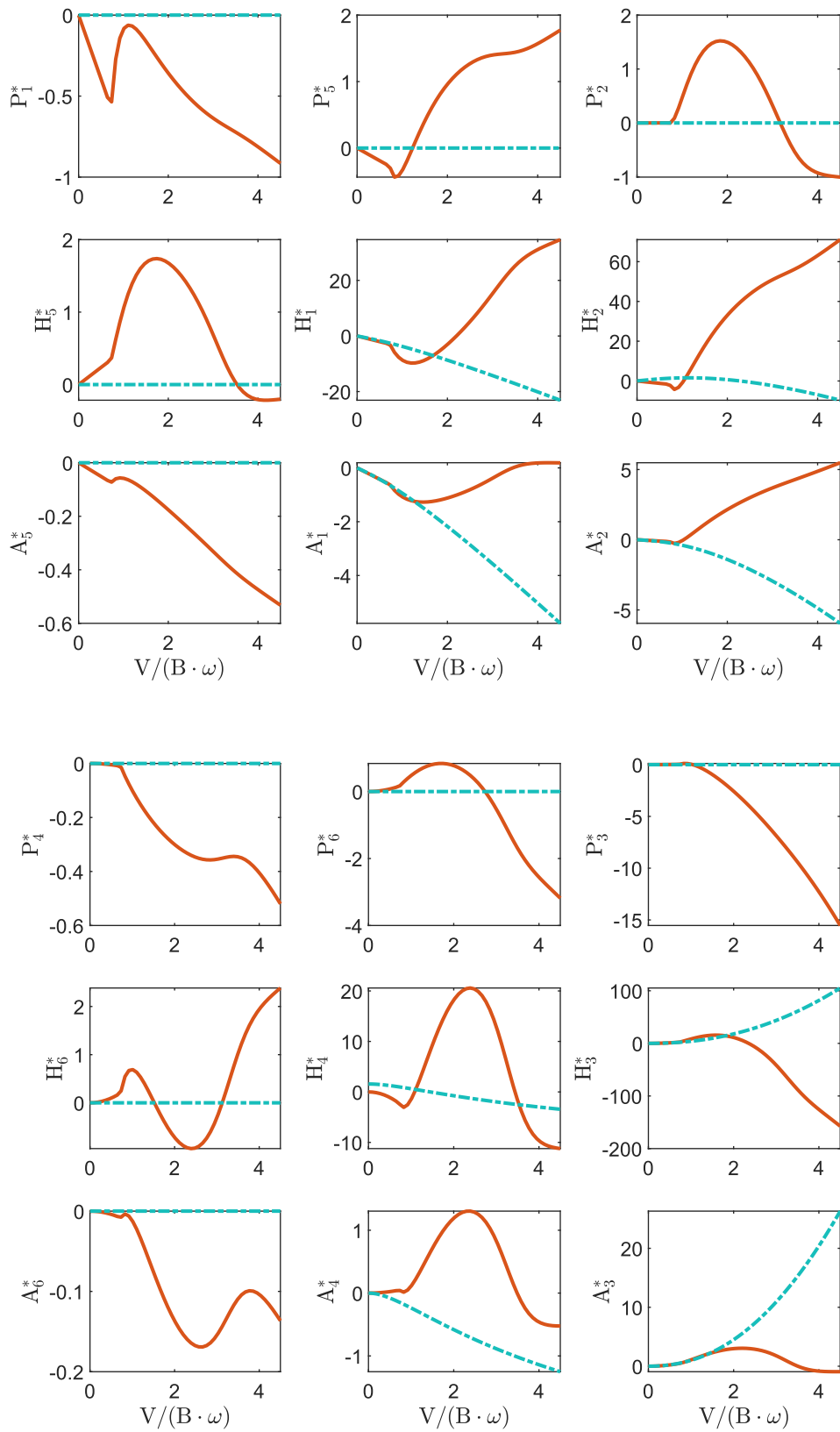


Figure E.7: ADs for 7.0 m

